

A 5902 II

Dz. 6

POLISH ACADEMY OF SCIENCES – WROCLAW BRANCH

WROCLAW UNIVERSITY OF TECHNOLOGY

ISSN 1644-9665
INDEX 375667

Biblioteka Główna i OINT
Politechniki Wrocławskiej



100100354458



ARCHIVES OF CIVIL AND MECHANICAL ENGINEERING

**Quarterly
Vol. VI, No. 2**

WROCLAW 2006

ADVISORY COMMITTEE

Chairman – JAN KMITA¹

JAN BILISZCZUK (Poland)
CZESŁAW CEMPEL (Poland)
JERZY GRONOSTAJSKI (Poland)
ANTONI GRONOWICZ (Poland)
M.S.J. HASHMI (Ireland)
HENRYK HAWRYLAK (Poland)
RYSZARD IZBICKI (Poland)
WAŁAW KASPRZAK (Poland)
MICHAEL KETTING (Germany)
MICHAŁ KLEIBER (Poland)
VADIM L. KOLMOGOROV (Russia)

ADOLF MACIEJNY (Poland)
ZDZISŁAW MARCINIAK (Poland)
KAZIMIERZ RYKALUK (Poland)
ANDRZEJ RYŻYŃSKI (Poland)
ZDZISŁAW SAMSONOWICZ (Poland)
WOJCIECH SZCZEPIŃSKI (Poland)
PAWEŁ ŚNIADY (Poland)
RYSZARD TADEUSIEWICZ (Poland)
TARRAS WANHEIM (Denmark)
WŁADYSŁAW WŁOSIŃSKI (Poland)
JERZY ZIÓŁKO (Poland)
JÓZEF ZASADZIŃSKI (Poland)

EDITORIAL BOARD

Editor-in-chief – JERZY GRONOSTAJSKI²

ROBERT ARRIEUX (France)
AUGUSTO BARATA DA ROCHA (Portugal)
GHEORGHE BRABIE (Romania)
LESŁAW BRUNARSKI (Poland)
EDWARD CHLEBUS (Poland)
L. DEMKOWICZ (USA)
KAZIMIERZ FLAGA (Poland)
YOSHINOBI FUJITANI (Japan)
FRANCISZEK GROSMAŃ (Poland)
MIECZYSLAW KAMIŃSKI (Poland)
Scientific secretary – SYLWESTER KOBIELAK

ANDRZEJ KOCANĀDA (Poland)
WAŁAW KOLLEK (Poland)
PIOTR KONDERLA (Poland)
ZBIGNIEW KOWAL (Poland)
TED KRAUTHAMMER (USA)
ERNEST KUBICA (Poland)
CEZARY MADRYAS (Poland)
TADEUSZ MIKULCZYŃSKI (Poland)
HARTMUT PASTERNAK (Germany)
MACIEJ PIETRZYK (Poland)
EUGENIUSZ RUSIŃSKI (Poland)
HANNA SUCHNICKA (Poland)

¹ The Faculty of Civil Engineering, Wrocław University of Technology
Wybrzeże Wyspiańskiego 27, 50-370 Wrocław, Poland
Tel. +48 71 320 41 35, Fax. +48 71 320 41 05, E-mail: jan.kmita@pwr.wroc.pl

² The Faculty of Mechanical Engineering, Wrocław University of Technology
ul. Łukasiewicza 5, 50-371 Wrocław, Poland
Tel. +48 71 320 21 73, Fax. +48 71 320 34 22, E-mail: jerzy.gronostajski@itma.pwr.wroc.pl

POLISH ACADEMY OF SCIENCES – WROCLAW BRANCH
WROCLAW UNIVERSITY OF TECHNOLOGY

DAR



ARCHIVES OF CIVIL AND MECHANICAL ENGINEERING

Quarterly
Vol. VI, No. 2

WROCLAW 2006

EDITOR IN CHIEF

JERZY GRONOSTAJSKI

EDITORIAL LAYOUT AND PROOF-READING

EWA SOBESTO, SEBASTIAN ŁAWRUSEWICZ

SECRETARY

TERESA RYGLOWSKA

Publisher: Committee of Civil and Mechanical Engineering
of Polish Academy of Sciences – Wrocław Branch,
Faculty of Civil Engineering and Faculty of Mechanical Engineering
of Wrocław University of Technology

© Copyright by Oficyna Wydawnicza Politechniki Wrocławskiej, Wrocław 2006

OFICYNA WYDAWNICZA POLITECHNIKI WROCŁAWSKIEJ
Wybrzeże Wyspiańskiego 27, 50-370 Wrocław

ISSN 1644-9665

Drukarnia Oficyny Wydawniczej Politechniki Wrocławskiej. Zam. nr 734/2006.

Contents

A. SMYKLA, Developing FEM models for difficult to describe 3D structures by using STL files – the case study of the human femur modelling	5
A. GRONOWICZ, M. PRUCNAL-WIESZTORT, Singular configurations of planar parallel manipulators	21
M. URBANIAK, Effect of the conditioning of CBN wheels on the technological results of HS 6-5-2 steel grinding	31
T. BŁASZCZYŃSKI, J. ŚCIGAŁO, Assessment of ultimate bearing capacity of RC sections affected by mineral oil	41
Z. MAŃKO, D. BĘBEN, Full-scale field tests of soil-steel bridge structure in two stages of its construction	57
J. MARKUL, B. SŁOWIŃSKI, Efficiency improvement in internal grinding	77
G. BRABIE, F. ENE, Application of the neural network method in optimization of the drawing process of hemispherical parts made from metal sheets	87
Information about PhDs	93

Spis treści

A. SMYKLA, Budowa modeli MES trudno opisywalnych struktur przestrzennych z wykorzystaniem plików STL na przykładzie głowy kości udowej człowieka	5
A. GRONOWICZ, M. PRUCNAL-WIESZTORT, Położenia osobliwe płaskich manipulatorów równoległych	21
M. URBANIAK, Wpływ kondycjonowania ściernic z azotku boru na efekty technologiczne szlifowania stali HS 6-5-2	31
T. BŁASZCZYŃSKI, J. ŚCIGAŁO, Ocena granicznej nośności przekroju żelbetowego poddanego oddziaływaniu olejów mineralnych	41
Z. MAŃKO, D. BĘBEN, Badania stalowo-gruntowej konstrukcji mostu w dwóch etapach jego budowy	57
J. MARKUL, B. SŁOWIŃSKI, Zwiększenie efektywności procesu szlifowania otworów ...	77
G. BRABIE, F. ENE, Zastosowanie metody siatek neuronowych do optymalizacji procesu tłoczenia półkulistych wyrobów z blach	87
Informacja o pracach doktorskich	93

Developing FEM models for difficult to describe 3D structures by using STL files – the case study of the human femur modelling

A. SMYKLA

Rzeszów University of Technology, ul. Wincentego Pola 2, 35-959 Rzeszów

The paper presents a computational approach to the process of creation of complex three-dimensional composite structures making use of STL files. The process of numerical treatment of measuring points' coordinates is shown. The construction of the model of human thigh bone head is demonstrated. Finally, the geometrical model of the object, which can be used by PATRAN system, is obtained.

Keywords: *FEM, thigh bone, STL, PCL*

1. Introduction

Without the slightest doubt computational modelling of the real world is a very sophisticated process. The creation of the model for FEM analysis can be attributed to such a category of problems. In order to manage its complexity, the modelling process usually involves the following stages:

- geometrical description,
- meshing of finite elements,
- description of material properties
- loading of boundary conditions (static and kinetic).

The paper presents an innovative approach to femur computational modelling. We will show how to automate the greater part of the PCL (the PATRAN Command Language) scripts generation process. The model generated by PCL script is the basis for further biomechanical analysis.

The femur belongs to a group of long bones whose tissue occurs in two forms: cortical and trabecular. The bone under consideration is inhomogeneous, anisotropic and behaves like a viscoelastic body [1], [2]. Figure 1 presents basic mechanical properties of the bone.

The first step of the modelling process is to determine geometrical coordinates of the bone. It can be done in many ways, e.g., by computer-assisted tomography (CT), magnetic resonance imaging (MRI), positron emission tomography (PET)). It is assumed that geometrical coordinates have been already known (due to coordinate measurement machine) and stored in a file (STL – stereolithography format is an ASCII or binary file used in manufacturing. It is a list of the triangular surfaces that de-

scribe a computer-generated solid model. This is the standard input for the most rapid prototyping machines). These data are the starting point for further modelling stages (Figure 2). Some of the stages have their own standard solutions (supported by off-the-shelf software packages). However, there are also stages that require customization and non-standard approach. For these parts of the process, author's own method and its software implementation have been developed.

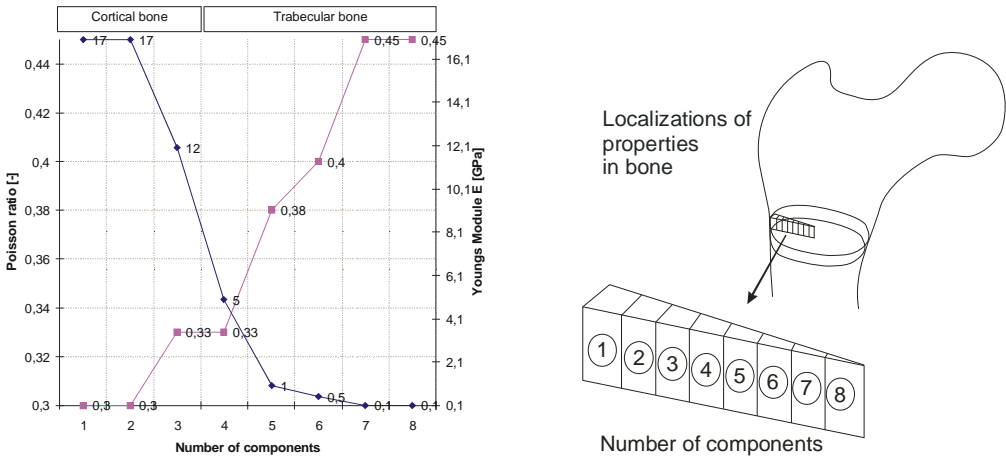


Fig. 1. Basic mechanical properties of a bone [5]

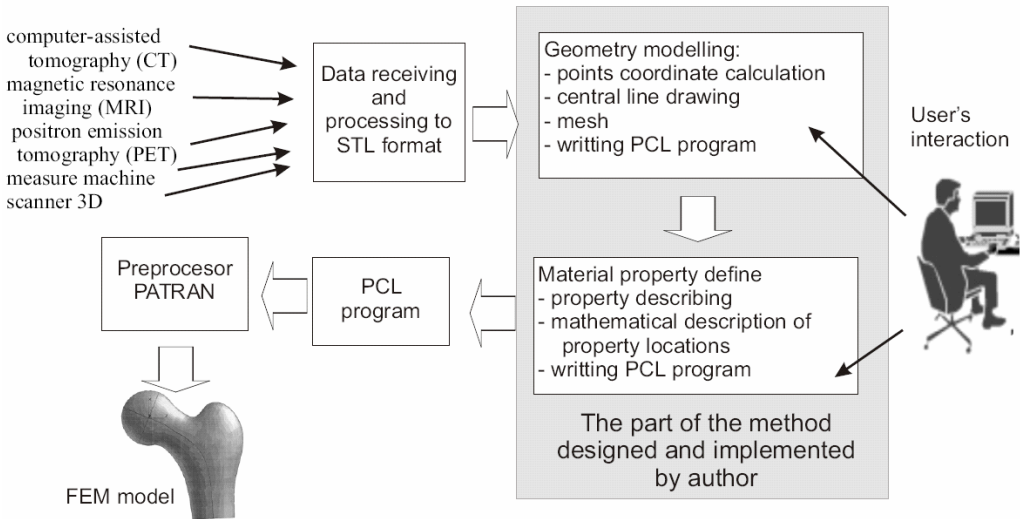


Fig. 2. Modelling process for FEM calculations

An STL format file may also be obtained automatically from the cloud of points, using an appropriate software (for instance, Raindrop Geometric). Based upon an edge defined in this way, we will define the location of the central line. This action depends upon data characteristics. In the majority of cases, this operation may be automatized. Should this process fail, it will become necessary to define the location of the central line in an interactive work phase. It will be necessary to include a definition of the location of the central line's end points $C_0 = [x_0, y_0, z_0]$, $C_N = [x_N, y_N, z_N]$ (Figure 4) in the automatic process data base. Making an assumption that the edges describing triangles are distributed evenly along the circumference, the remaining points may be delimited using the following algorithm:

1. Define a plane S_1 such that S_1 contains $C_{S1} = (C_0 + C_N)/2$ and that S_1 is a normal plane for the vector $\mathbf{V} = [v_x, v_y, v_z] = [x_N - x_0, y_N - y_0, z_N - z_0]$. The equation of the plane has the following form: $v_x(x - c_{sx}) + v_y(y - c_{sy}) + v_z(z - c_{sz}) = 0$.

2. Find out which of the TR_i edge forming triangles are intersected by the S_1 plane. A necessary and sufficient condition here is that one of the triangle sides is intersected by the plane. This can be checked by performing the following operation: $t = ((TC1 - C_{S1}) \cdot \mathbf{V}) / ((TC1 - TC2) \cdot \mathbf{V})$, where $TC1, TC2, TC3$ are the vertices of the triangle TR_i , and C_{S1} is the point on the plane S_1 (Figure 3). If t is contained within the interval $(0 \dots 1)$, then intersection should take place at point $K_i = TC1 + t * (TC2 - TC1)$. All points K_i (for all triangles TR_i) should be memorized.

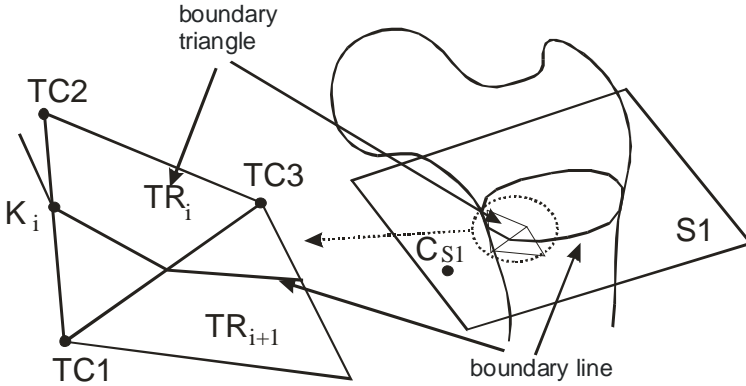


Fig. 3. Calculation of points K_i

3. A definition of the point C_1 is done through: $C_1 = 1/m \sum_{i=1}^m K_i$, where m is a number of points calculated within step 2.

4. Build sections C_0C_1 and C_1C_N , and repeat steps 1 through 3 (Figure 4). In practical terms, it is enough to use the above iterative algorithm to obtain 5–9 central points C_i .

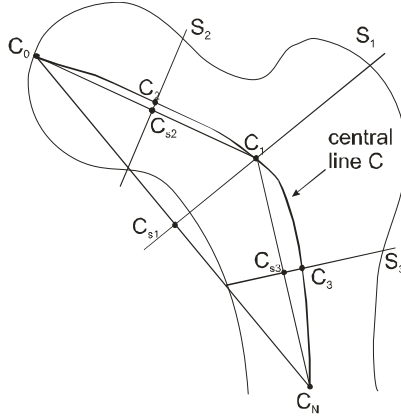


Fig. 4. An iterative manner of defining points of the central line C

The whole curve may be interpolated using the Ranner Subsplines. For $n+1$ points $C_i = (x_i, y_i)$ with $n > 3$ and $C_{i+1} \neq C_i$ for all $i = 0, \dots, n-1$, we want to find a smooth curve that connects the points in their given order. The curve is to be composed of piecewise cubic vectorial polynomials:

$$S_i(t) = a_i + t b_i + t^2 c_i + t^3 d_i, \quad t \in [0, T_i], \quad i = 0, \dots, n-1.$$

Here $a_i, b_i, c_i, d_i \in R^2$. The segment of the curve joining C_i and C_{i+1} is consequently given by a polynomial of the third degree at most. The coefficients $a_i, b_i, c_i, d_i \in R^2$ must be calculated for $i = 0, \dots, n-1$ as well as the lengths T_i of the parameter intervals. For this purpose, we must know the points $S_i(0) = P_i$, $S_i(T_i) = P_{i+1}$ and the unit tangent vectors $S'_i(0) = t_i$, $S'_i(T_i) = t_{i+1}$. If we demand in addition that $\|S'(T_i/2)\| = 1$, then T_i can be easily computed [4]:

$$\int_0^{T_i} \|S'_i(t)\| dt \approx \frac{T_i}{6} (\|S'_i(0)\| + 4\|S'_i(T_i/2)\| + \|S'_i(T_i)\|) = T_i,$$

where the symbol $\|s\| = \|[x, y]\| = \sqrt{x^2 + y^2}$.

For this reason, t is an approximation of the arc length parametrization. If the tangents to the curve at P_i are not known, the unit tangent vectors t_i must first be determined. We want to be able to reproduce straight line segment and corners. For the chordal vectors $s_i = C_{i+1} - C_i \neq 0$ normalized to $s_i^0 = s_i / \|s_i\|$, the formula of Ranner describes the non-normalized tangent vector as

$$\mathbf{t}_i = (1-\alpha_i) \mathbf{s}_{i-1} + \alpha_i \mathbf{s}_i = \mathbf{s}_{i-1} + \alpha_i (\mathbf{s}_i - \mathbf{s}_{i-1})$$

with

$$\alpha_i = \frac{A(\mathbf{s}_{i-2}^0, \mathbf{s}_{i-1}^0)}{A(\mathbf{s}_{i-2}^0, \mathbf{s}_{i-1}^0) + A(\mathbf{s}_i^0, \mathbf{s}_{i+1}^0)}.$$

Here $A(\mathbf{s}, \mathbf{t})$ measures the area of parallelogram spanned by the vector \mathbf{s} and $\mathbf{t} \in \mathbb{R}^2$. This area can be most easily computed:

$$A(\mathbf{s}, \mathbf{t}) = \sqrt{1 - (\mathbf{s}^T \mathbf{t})^2} = |\det(\mathbf{s}, \mathbf{t})|.$$

The tangent vector \mathbf{t}_i (Figure 5) at the point C_i is defined by linear combination of $\mathbf{s}_{i-2}^0, \dots, \mathbf{s}_{i+1}^0$ where the shape of the form was written and tested experimentally by Ranner and Pochop [6] to obtain well fitting smooth curve.

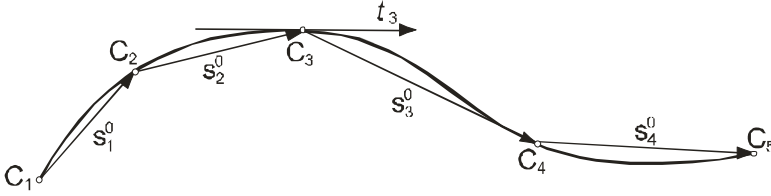


Fig. 5. Definition of the vector \mathbf{t}

Those formulas are meaningful for all C_i , which possess two adjacent points to the “left” and to the “right”. If the denominator in α_i does not vanish, we have

$$\mathbf{t}_i = \mathbf{s}_{i-1} \text{ if } C_{i-2}, C_{i-1}, C_i \text{ are collinear,}$$

$$\mathbf{t}_i = \mathbf{s}_i \text{ if } C_i, C_{i+1}, C_{i+2} \text{ are collinear.}$$

If the denominator is zero and $A(\mathbf{s}_{i-1}^0, \mathbf{s}_i^0) > 0$, we have a vertex. In order to represent vertices by a Ranner subspline, we shall assign each C_i the left and right unit tangent vectors \mathbf{t}_i^L and \mathbf{t}_i^R , respectively. If we want to have a vertex at C_i we shall set $\mathbf{t}_i^L = \mathbf{s}_{i-1}^0$ and $\mathbf{t}_i^R = \mathbf{s}_i^0$. Otherwise we set $\mathbf{t}_i^R = \mathbf{t}_i^L = \mathbf{t}_i$.

The above schema can be written as the following algorithm

$$C_i(\mathbf{t}) = \mathbf{a}_i + t\mathbf{b}_i + t_2\mathbf{c}_i + t_3\mathbf{d}_i$$

in six steps:

1. For $i = 0, \dots, n-1$ find the chordal vectors:

$$s_i = K_{i+1} - K_i.$$

2. Determine additional chordal vectors:

$$s_{-2} = 3s_0 - 2s_1,$$

$$s_{-1} = 2s_0 - s_1,$$

$$s_n = 2s_{n-1} - 2s_{n-2},$$

$$s_{n+1} = 3s_{n-1} - 2s_{n-2}.$$

3. Normalize the chordal vectors s_i for $i = -2, -1, \dots, n+1$:

$$\text{if } \|s_i\| > 0, \text{ set } s_i^0 = s_i / \|s_i\|,$$

$$\text{if } \|s_i\| = 0, \text{ set } s_i^0 = 0.$$

4. Determine the left and right unit tangent vectors for $i = 0, \dots, n$.

$$\text{Set } NE = \sqrt{1 - (s_{i-2}^0 s_{i-1}^0)^2} + \sqrt{1 - (s_i^0 s_{i+1}^0)^2}.$$

If $NE > 0$:

$$\alpha_i = \sqrt{1 - (s_{i-2}^0 s_{i-1}^0)^2} / NE,$$

$$t_i^L = s_{i-1} + \alpha_i (s_i - s_{i-1}),$$

$$t_i^L = t_i^L / \|t_i^L\|,$$

$$t_i^R = t_i^L.$$

If $NE = 0$:

$$t_i^L = s_{i-1}^0,$$

$$t_i^R = s_i^0.$$

5. For each $i = 0, \dots, n-1$ compute the length T_i^* of the parameter interval:

$$A = 16 - \|t_i^R + t_{i+1}^L\|^2,$$

$$B = 6s_i^T \cdot (t_i^R + t_{i+1}^L),$$

$$C = 36\|s_i\|^2,$$

$$T_i^* = (-B + \sqrt{B^2 + AC}) / A.$$

6. Compute the coefficients for the Ranner subspline for $i = 0, \dots, n-1$:

$$a_i = C_i,$$

$$b_i = t_i^R,$$

$$c_i = \frac{3}{(T_i^*)^2} s_i - \frac{1}{T_i^*} (2t_i^R + t_{i+1}^L),$$

$$d_i = \frac{3}{(T_i^*)^2} (t_i^R + t_{i+1}^L) - \frac{2}{(T_i^*)^3} s_i.$$

The next step is to determine the location of the lines \mathbf{V}_{ab} forming 3D FEM mesh. The matrix equations of the line \mathbf{V}_{ab} have been defined in the following steps:

- placing vector \mathbf{V} [1 0 0] based on point [0 0 0],
- rotating vector \mathbf{V} about the angle α and then the angle β ,
- translating vector \mathbf{V} to point $[x_e, y_e, z_e]$.

The steps are shown in Figure 6.

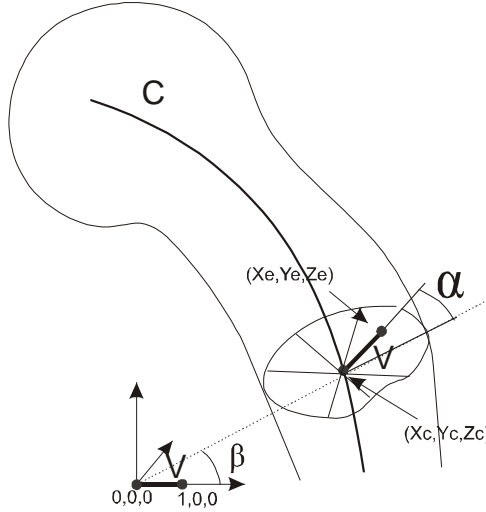


Fig. 6. The vector $\mathbf{V}_{\alpha\beta}$ transformation

The matrix equations are as follows:

$$\begin{bmatrix} X_e \\ Y_e \\ Z_e \\ 1 \end{bmatrix} = \begin{bmatrix} 1 \\ 0 \\ 0 \\ 1 \end{bmatrix} \begin{bmatrix} 1 & 0 & 0 & X_c \\ 0 & 1 & 0 & Y_c \\ 0 & 0 & 1 & Z_c \\ 0 & 0 & 0 & 1 \end{bmatrix} \begin{bmatrix} \cos \alpha & -\sin \alpha & 0 & 0 \\ \sin \alpha & \cos \alpha & 0 & 0 \\ 0 & 0 & 1 & 0 \\ 0 & 0 & 0 & 1 \end{bmatrix} \begin{bmatrix} \cos \beta & 0 & \sin \beta & 0 \\ 0 & 1 & 0 & 0 \\ -\sin \beta & 0 & \cos \beta & 0 \\ 0 & 0 & 0 & 1 \end{bmatrix} \quad (1)$$

The next step is to calculate the common points of the bone's border and the line $\mathbf{V}_{\alpha\beta}$. In order to identify the unknown coordinates, the data are read from the STL file in a sequential manner (Figure 7).

For example, the coordinates of points $[x_b, y_b, z_b]$ are determined by building a plane by using the points $Brz_k(x_1, y_1, z_1)$, $Brz_l(x_2, y_2, z_2)$ and $Brz_m(x_3, y_3, z_3)$, where the equation of plane is:

$$A \cdot x + B \cdot y + C \cdot z + D = 0. \quad (2)$$

The coefficients A, B, C, D are calculated using the equation of the plane containing 3 points Brz_k, Brz_l, Brz_m :

$$\begin{vmatrix} x & y & z & 1 \\ x_1 & y_1 & z_1 & 1 \\ x_2 & y_2 & z_2 & 1 \\ x_3 & y_3 & z_3 & 1 \end{vmatrix} = 0. \quad (3)$$

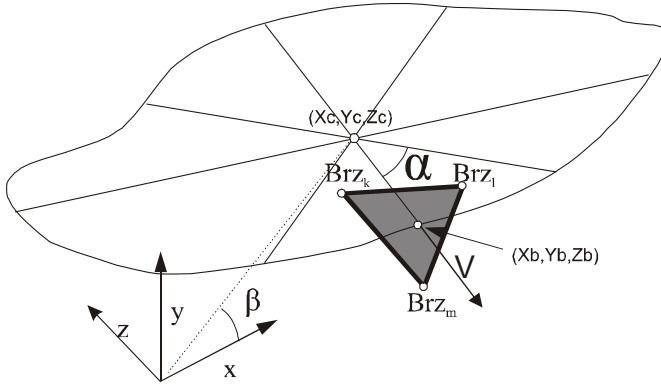


Fig. 7. Graphical representation of border points estimations

In the next step, the unknown coordinates are calculated based on the results of the previous stage:

$$\begin{bmatrix} Brz_x \\ Brz_y \\ Brz_z \end{bmatrix} = \begin{bmatrix} A & B & C \\ ye-yc & xe-yc & 0 \\ ze-zc & 0 & xe-xc \end{bmatrix}^{-1} \begin{bmatrix} -D \\ xc(ye-yc) - yc(xe-xc) \\ xc(ze-zc) - ze(xe-xc) \end{bmatrix}. \quad (4)$$

2. Removing errors on the border

In many cases, the data obtained based on CT or RNI have nonsmooth character, and the coordinates of the border points that have been determined during the scanning process are not precise. The numerical models of medical images have been remembered in voxal form which causes steplike surface effect. This means that subsequent cross-sections may be inaccurately placed. Such a misplacement may lead to nonsmooth numerical models and finally to stress concentration resulting from geometrical steplike irregularities. Figure 8 presents three cases illustrating the relationship between the quality of border description data and the size of finite elements.

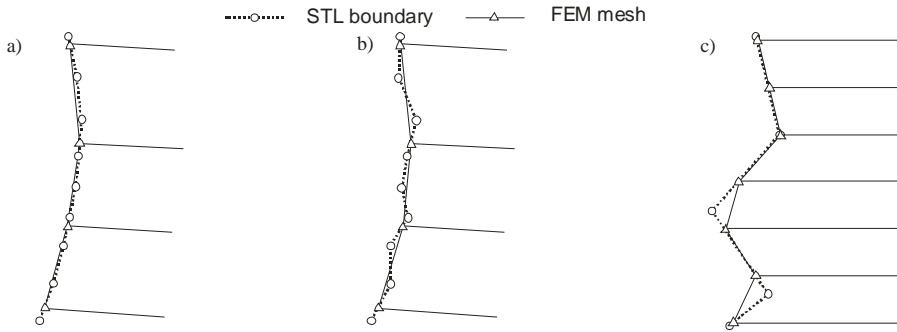


Fig. 8. Relationship between the “quality” of border description data (stored in STL files) and the size of FE: a) the appropriate STL mesh, b) STL is imprecisely measured, FE mesh is thin, thus the effect of modelling is acceptable, c) STL is imprecisely measured, FE mesh is thin, thus the effect of modelling is inappropriate

Of course, if data are accurate, then the resulting numerical models will be fitted. A similar situation may arise when the nodes of border definition are placed thicker than FE mesh. In such a case, the “smoothing” of FE mesh is “natural”. If it is necessary to build the FE mesh thicker than inaccurate STL data, then the final numerical model may contain elements that are not exactly fitted on the border. In this case, the process of creation of felicitous models is possible after changing the coordinates of border points with continuous derivative precision.

This way is presented below. In order to verify the approach proposed, the data describing the femur geometry (which were input into a computer) were obtained from the Vita Mot co-ordinate measuring machine, so the border was described with high accuracy. Next, the results of simulating scanning errors (e.g., CT) were added to the data set. This stage was done by randomly moving coordinates of the border points in the cross-sections YZ . The bottom part (original and random error) of the modelled femur was presented in Figure 9.

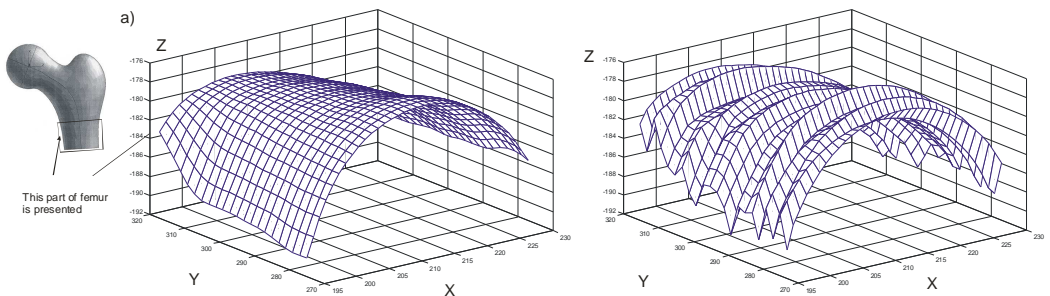


Fig. 9. The bottom part of femur: a) original data, b) data with randomly moving coordinates in $\langle -3, 3 \rangle$ interval and direction YZ

In order to avoid the stiffness variability, the model from Figure 9b was numerically smoothed. This task was carried out in two steps. In the first step, we had to approximate the shape of the border in the direction ZX by means of cubic splines concept. Next, the results of step one are processed again in the direction XZ (it is not necessary in all cases). The calculation of smoothing spline was done with the `csaps` built-in Matlab function. Next paragraph describes how it operates.

The cubic smoothing spline s to the given data x, y is constructed for the specified smoothing parameter p $[0..1]$ and the optionally specified weight w . The smoothing spline minimizes:

$$p \sum_i w(i)(y(i) - s(x(i)))^2 + (1 - p) \int \lambda(t)(D^2 s)(t)^2 dt,$$

where w is matrix on size (x) the default value for the weight vector w in the error measure, and 1 the default for the piecewise constant weight function in the roughness measure. For $p = 0$, s is the least-squares straight line fitting to the data, while, at the other extreme, i.e., for $p = 1$, s is the variational, or ‘natural’ cubic spline interpolator. As p moves from 0 to 1, the smoothing spline changes from one extreme to the other.

This operation in MATLAB system can be done by using the following command: `wyn=csaps(x,y,p)`. The `x` and `y` are the input vectors of point coefficients and `p` is the weight. The vector of results (`wyn`) has a new value of points of smoothing spline. The example of applying the function presented in a chosen cross-section is shown in Figure 10.

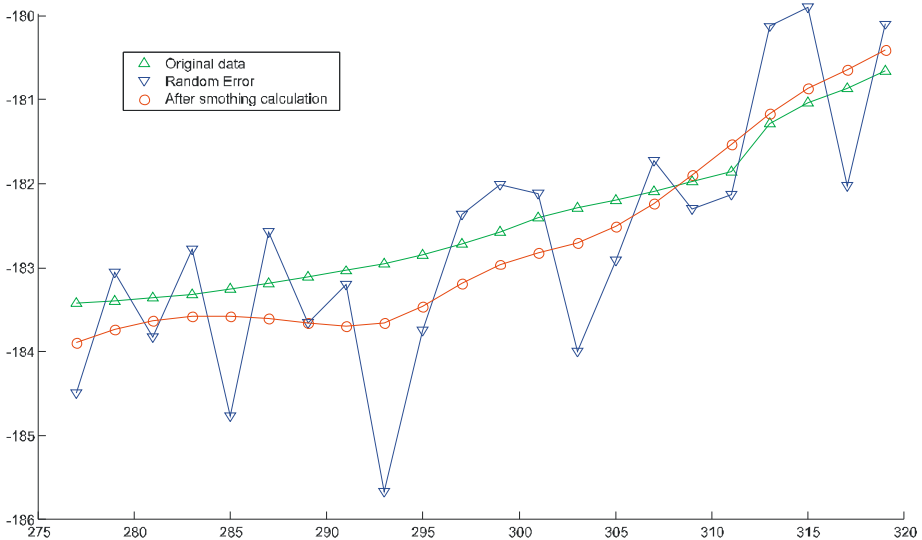


Fig. 10. The example of applying the `csaps` function in a chosen cross-section

After applying the csaps function for each cross-section we obtain the area which is almost smoothed (Figure 11).

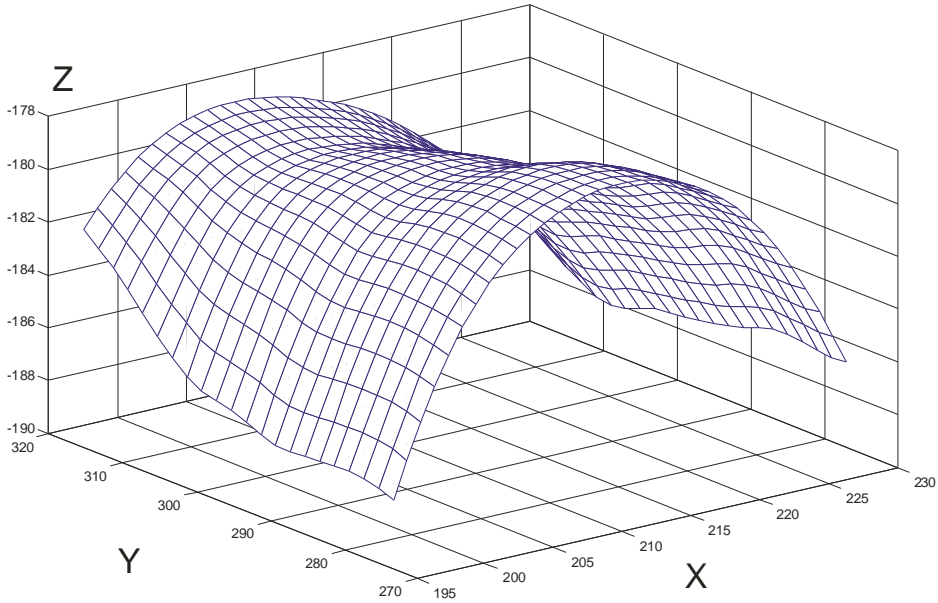


Fig. 11. Smoothed area after applying the csaps function in all cross-sections

We can show the error of this approximation method as the difference between the real values of the border coordinates determined experimentally and the values of randomly generated errors (Figure 12 a)), and the difference between the real values of the border coordinates determined experimentally and the values of border coordinates after smoothing process (Figure 12 b)).

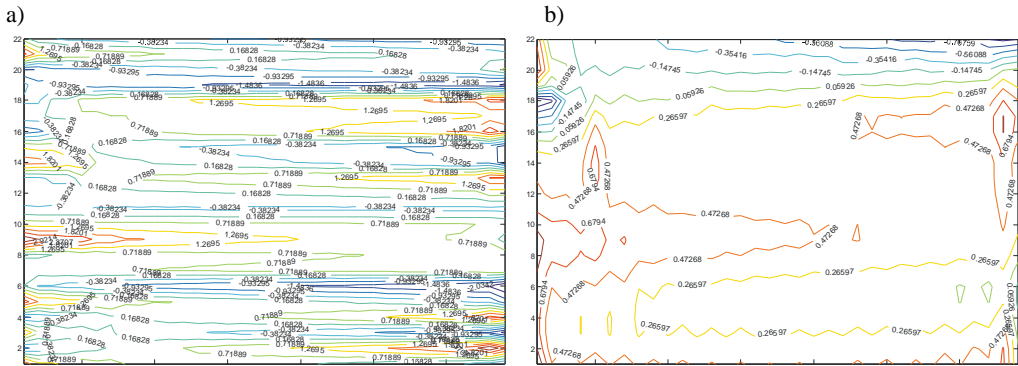


Fig. 12. Error of border placement: a) before approximation, b) after smoothing

Of course, in real CT models the borders are less wiggled, so the effect of using the method proposed will be better.

3. The process of model building in NASTRAN system

In order to create a solid geometry element, the PATRAN system has been used. The procedure involves the following stages:

- Top points definition.
- Curve (for adequate top points) definition.
- Extension of the surface between points.
- Extension of the solid by using of surfaces.

PATRAN preprocessor enables control of the system by internal language (PCL) [7]. The sequence of the system commands below shows how to create a solid geometry using node points coordinates.

Node points coordinates

```
[0, 0, 0]
[1, 0, 0]
[1, 0, 1]
[0, 0, 0.5]
[0, 1, 0]
[0, 1, 0.5]
[1, 1, 1]
[1, 1, 0]
```

Commands

```
STRING asm_create_grid_xyz_created_ids[VIRTUAL]
asm_const_grid_xyz( "1", "[0 0 0]", "Coord 0",
asm_create_grid_xyz_created_ids )
asm_const_grid_xyz( "2", "[1 0 0]", "Coord 0",
asm_create_grid_xyz_created_ids )
asm_const_grid_xyz( "3", "[1 0 1]", "Coord 0",
asm_create_grid_xyz_created_ids )
asm_const_grid_xyz( "4", "[1 1 0]", "Coord 0",
asm_create_grid_xyz_created_ids )
asm_const_grid_xyz( "5", "[0 1 0]", "Coord 0",
asm_create_grid_xyz_created_ids )
asm_const_grid_xyz( "6", "[1 1 1]", "Coord 0",
asm_create_grid_xyz_created_ids )
asm_const_grid_xyz( "7", "[0 0 0.5]", "Coord 0",
asm_create_grid_xyz_created_ids )
asm_const_grid_xyz( "8", "[0 1 0.5]", "Coord 0",
asm_create_grid_xyz_created_ids )
STRING asm_line_2point_created_ids[VIRTUAL]
asm_const_line_2point( "1", "Point 7 ", "Point 3 ", 0, "", 50.,
1, asm_line_2point_created_ids )
```

```

asm_const_line_2point( "2", "Point 1 ", "Point 2 ", 0, "", 50.,
1, asm_line_2point_created_ids )
asm_const_line_2point( "3", "Point 8 ", "Point 6 ", 0, "", 50.,
1, asm_line_2point_created_ids )
asm_const_line_2point( "4", "Point 5 ", "Point 4 ", 0, "", 50.,
1, asm_line_2point_created_ids )
STRING sgm_surface_2curve_created_ids[VIRTUAL]
sgm_const_surface_2curve( "1", "Curve 3 ", "Curve 1 ",
sgm_surface_2curve_created_ids )
sgm_const_surface_2curve( "2", "Curve 4 ", "Curve 2 ",
sgm_surface_2curve_created_ids )
STRING sgm_solid_2surface_created_ids[VIRTUAL]
sgm_const_solid_2surface_v1( "1", TRUE, "Surface 2 ", "Surface
1 ", sgm_solid_2surface_created_ids )

```

Figure 13 outlines the structure generated using the PATRAN PCL script.

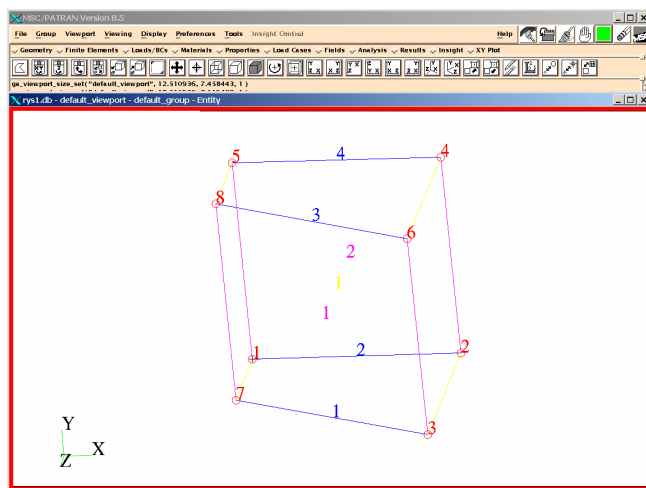


Fig. 13. PATRAN preprocessor and solid built by using the PCL program presented

The script has been automatically created by computer program written in a high-level language. During the process of PCL script creation the following conditions have to be met:

- Special attention has to be paid to the proper numbering of points, curves and solids.
- Each element has to have adequate material properties assigned. Such an assignment has been done due to the similarity of the bone internal structure to the cylinder structure (the properties of the cylinder's elements are mapped to the properties of the bone's elements in the concrete places) (Figure 14).

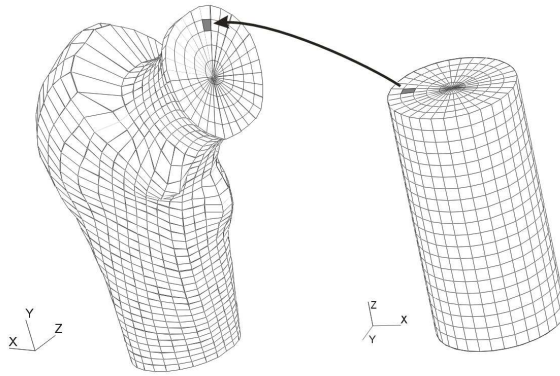


Fig. 14. Relationship between the properties of the cylinder's elements and bone's elements

The modelling of the femur has been carried out in the PATRAN system. This system provides the modeler with predefined language (PCL) that enables controlling the program and performing all basic operations.

The material properties of the elements have been identified through determining their positions in the cylindrical areas (Figure 15).

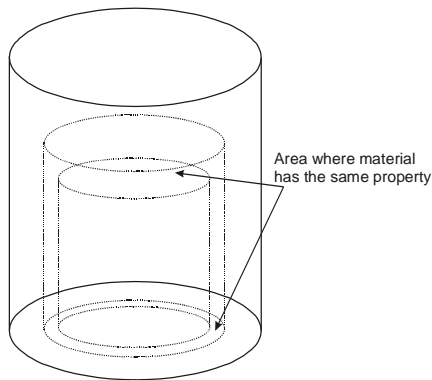


Fig. 15. Idea of the allocation of elements properties

We can define the properties of material and allocate them in a correct position in the way similar to that of creating geometry in PCL language.

It can be done by

```
material.create( "Analysis code ID",10, "Analysis type ID", 1, "mat_bone", 0, @
  "Date: 06-Nov-03 Time: 17:08:32", "Isotropic", 1, "Directionality", @
  1, "Linearity", 1,"Homogeneous", 0, "Elastic", 1, "Model Options & IDs", [" " @
  , "", "", "", ""], [0, 0, 0, 0, 0], "Active Flag", 1, "Create", 10, @
  "External Flag", FALSE,"Property IDs", ["Elastic Modulus", "Poisson Ratio"], @
```

```
[2, 5, 0], "Property Values", ["17000000", "0.3", "" ] )  
elementprops_create( "properties_of_element", 71, 1, 30, 1, 1, 15, [13, 21, @  
1079, 20], [5, 9, 3, 1], ["m:mat_bone", "", "", ""], " Solid 1" )
```

The final results of the modelling process are presented in Figure 16.

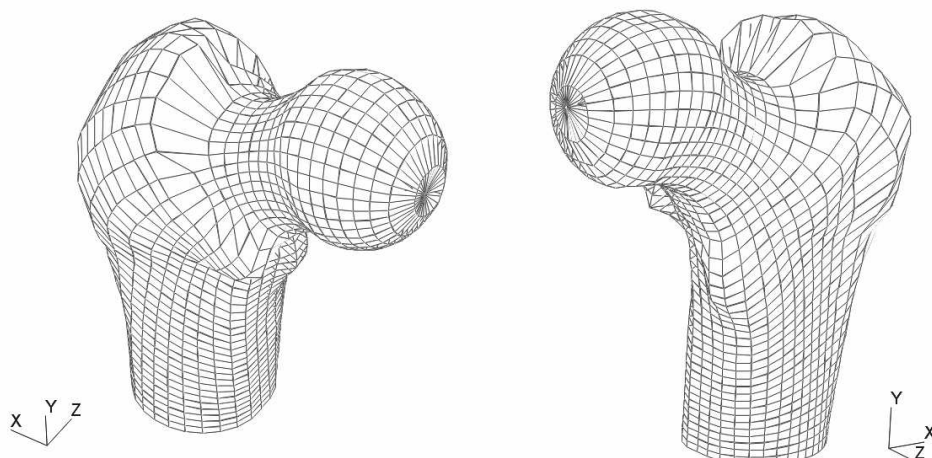


Figure 16. Results of modelling process.

4. Final remarks

1. When applying our method we can create a model with 8-node FEM elements. The elements of this kind are better than 4-node ones, which can be used for modelling each structure in an easy way.
2. The method presented may enable us to write programs for automatic FEM analysis of stress, strain or displacement in similar structures in the future.
3. The model presented is smooth, without any sudden changes of stiffness and unreal properties.
4. We can describe the bone properties in a mathematical form and modify it during calculations.

References

- [1] Będziński R.: *Biomechanika inżynierska*, Oficyna Wydawnicza Politechniki Wrocławskiej, Wrocław, 1997.
- [2] Cwanek J., Kopecki H., Kopkowicz M., Smykła A.: *Modelowe badania rozkładu sił wewnętrznych w elementach nośnych stawu biodrowego, wspomagane komputerowo*, Mechanika w medycynie, Zbiór prac seminarium naukowego, Rzeszów, 2000.

- [3] Foley D., Andries D., Feiner K., Hughes J., Philips R.: *Introduction to computer graphics*, Addison-Wesley, 1990.
- [4] Engeln-Mullges G., Uhlig F.: *ical Algorithms with C*, Springer, 1996.
- [5] Okrajni J., Jasik A., Kusz D.: *Wpływ niejednorodności właściwości materiałowych i sposobu obciążenia na wyężenie komponentów modelu kości udowej*, Acta of Bioengineering and Biomechanics, Volume 3, Supplement 2, 2001.
- [6] Ranner G., Pochop V.: *A new method for loacal smooth interpolation EUROGRAPHICS 81*, J.L. Encarnacao (ed.), pp. 137–147.
- [7] MSC/PATRAN, The PATRAN Command Language (PCL).
- [8] www.biodro.home.pl/nauka/cytaty/biomexim/biomechanika.html

Budowa modeli MES trudno opisywalnych struktur przestrzennych z wykorzystaniem plików STL na przykładzie głowy kości udowej człowieka

Opisano proces modelowania złożonych struktur przestrzennych. Informacja o geometrii tych struktur jest zapisywana w plikach STL i stanowi dane wejściowe opisywanej metody. Jako przykład przedstawiono proces modelowania głowy kości udowej człowieka wraz z matematycznym opisem jej właściwości. Modelowanie wykonano, korzystając z języka PCL i systemu PATRAN.

Singular configurations of planar parallel manipulators

A. GRONOWICZ, M. PRUCNAL-WIESZTORT

Wrocław University of Technology, Wybrzeże Wyspiańskiego 25, 50-370 Wrocław

The paper deals with determining singular configurations for a group of 3 DOF planar parallel manipulators whose links form revolute and prismatic pairs. Relations for Jacobian matrix determinants for selected mechanisms are derived. The form of the equations differs depending on the structure of the inner part of the manipulators belonging to the Assur groups of the 3rd class. An analysis of the relations shows that singular configurations occur when Assur points coincide. Due to the approach proposed, singular configurations can be determined using classical kinematic analysis methods, without it being necessary to specify a Jacobian determinant and to define its zeroing conditions. Also a method of determining singular configurations from auxiliary mechanisms' characteristic point trajectory is proposed. The research results make it easier to define the conditions in which singular configurations occur.

Keywords: *singularity, planar parallel manipulators*

1. Introduction

Due to their advantages, such as the ability to carry considerable loads at high speed and with great precision, planar parallel manipulators can have numerous applications. They are characterized by a relatively small workspace which is partly inaccessible due to the occurrence of singular configurations. Once the system enters a singular configuration, it cannot be pulled out of it and may be damaged as a result. Therefore the determination of singular configurations is vitally important for planning the motion of actual manipulators and for their analysis and design.

There are many works, e.g., [1], [2], [3], which deal with the singular configurations of planar parallel manipulators. This paper presents the results of research aimed at deriving generalizations which would cover as large a group of 3 DOF planar parallel systems as possible. The knowledge gained may contribute to a wider use of the mechanisms.

2. Jacobian matrix determinant as indicator of singular configurations

A singular configuration is a peculiar position of the driven link (the effector) in which the manipulator cannot be effectively controlled [4]. Analyses of the motion of parallel manipulators indicate singular configurations, irrespective of the modelling method.

In order to describe the mechanism in absolute coordinates for a system with n movable links, $k = 3n$ linearly independent equations need to be formulated [5]. For

a mechanism with mobility m the number of equations which follow from the equations of constraints (joint constraints Φ^W) is $k - m$. The other equations are derived from the formulation for the motion of the driving links (excitations Φ^C). Hence a multi-body mechanical system is described by the following system of equations:

$$\Phi(\mathbf{q}, t) = \begin{bmatrix} \Phi^W(\mathbf{q}) \\ \Phi^C(\mathbf{q}, t) \end{bmatrix} = 0. \quad (1)$$

After differentiating Equation (1), taking into account that matrix \mathbf{q} is time variable, the following equation of velocity is obtained:

$$\dot{\mathbf{q}} = -\Phi_q^{-1} \Phi_t. \quad (2)$$

The equation has a solution for:

$$\det(\Phi_q) \neq 0. \quad (3)$$

The above notation of derivatives conforms to the Lagrange symbols, where the subscript t denotes a derivative over time and Φ_q is a Jacobian of the constraints matrix Φ . The form of the matrix Φ_q depends on the kind of problem (forward or inverse kinematics problem). A singular configuration occurs when the Jacobian matrix determinant is equal to zero.

Generally, three types of singularity can be distinguished in the workspace of planar parallel manipulators [1], [6]:

- forward kinematics problem singularity $\det(\Phi_{q1}) = 0$,
- inverse kinematics problem singularity $\det(\Phi_{q2}) = 0$,
- mixed singularity $\det(\Phi_{q1}) = 0$ and $\det(\Phi_{q2}) = 0$.

3. Analysis of singularities of manipulators with symmetrical legs with driving links at base

Three degrees of freedom planar parallel manipulators with one driving link in each of the three legs are considered. 384 systems, including 56 designs with driving links at the base, form a complete set of possible design solutions. Figure 1 shows symmetrical systems with driving links at the base.

Each of the manipulators considered consists of three kinematic chains connecting end-effector 7 to base 0. In each chain, there are driving links 1, 2, 3 located at the base and intermediate links 4, 5, 6 connected to the driving links and end-effector 7. A singular configuration analysis was performed using the relations for the Jacobian matrix determinant for the forward kinematics problem.

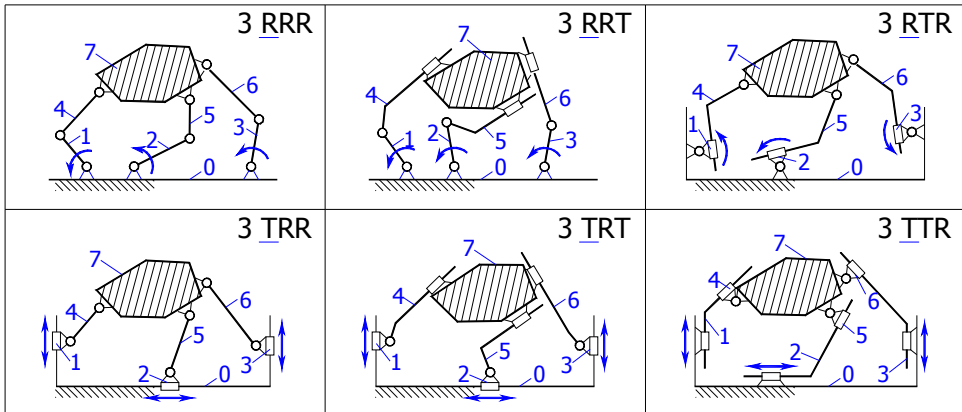


Fig. 1. Kinematic schemes of the mechanisms analysed

Appropriate equations of constraints were formulated for all the types of the systems shown in Figure 1. Then the vector of equations was differentiated whereby successive Jacobian matrices were obtained. Finally, relations for Jacobian determinants were derived. The relations are presented in the Table.

The manipulators presented in Table 1 are grouped according to the form of their determinants. One should note that the relations for determinants are identical in the systems whose inner parts, after the driving links and the base have been removed, are identical [7]. Table 1 also includes configurations which fulfil condition $\det(\Phi_q) = 0$. It becomes apparent that there is an analogy to Assur's classification of planar systems [8] – the inner systems are the 3rd class Assur groups. Hence the following general condition for the occurrence of manipulator singular configurations can be formulated:

a singular configuration for the considered systems occurs when the configuration of the inner group is characterized by the coincidence of Assur points [7].

A special case of a singular configuration (not shown in the table, but satisfying equation $\det(\Phi_q) = 0$) is the coincidence of the Assur points in infinity. This is manifested in the parallelism of appropriate straight lines.

4. Determination of singular configurations through kinematic analysis by graphical method

Conditions for the occurrence of singular configurations for the systems considered were defined by specifying the Jacobian determinant $\det(\Phi_q)$ and equating it to zero. But the observation that a singular configuration corresponds to the coincidence of the Assur points allows us to determine the singular configurations of all the systems and it is not necessary to specify the Jacobian determinant and to define conditions for equation $\det(\Phi_q) = 0$.

The conclusions drawn from the formulated condition of the occurrence of singular configurations allow us to determine singular configurations for manipulators with asymmetrical legs with driving links at the base and for manipulators with driving links located in the legs. By analogy to the configurations shown in Table 1 it is possible to determine the singular configurations of each manipulator belonging to the group under consideration. Figure 2 shows singular configurations for the $2RTR1RRR$ and $TRTRTRRRR$ systems with driving links at the base, determined from the positions of the Assur points.

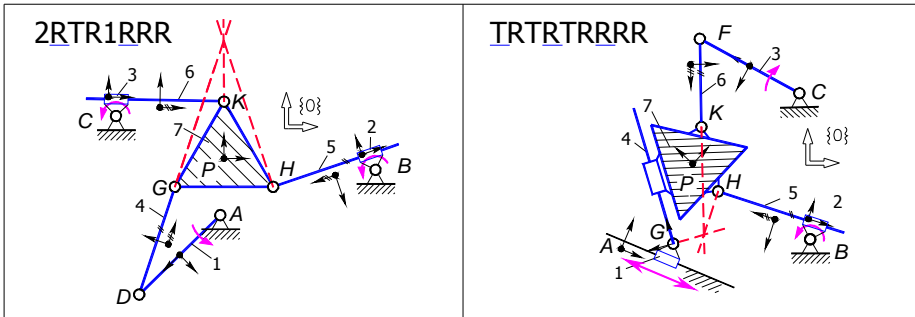


Fig. 2. Singular configuration of manipulators with asymmetrical legs

Hence singular configuration for a given manipulator can be determined if the conditions at which the coincidence of the Assur points occurs are known.

One of the possible ways of determining such conditions is a kinematic analysis performed using graphical methods. In the forward kinematics problem for each manipulator belonging to the group considered, the velocities of the three driving links are given, while the velocity of the end-effector point P is sought. In order to determine this velocity, first the velocity of the peculiar point M (an Assur point) belonging to the end-effector and then the velocities of the other end-effector points should be calculated.

In Table 1, we have:

l_i – the length of links $i = \{4, 5, 6\}$,

${}^7x_n, {}^7y_n$ – the coordinates of the point n in the system of effector 7, $n = \{G, H, K\}$,

$\theta_{j,k} = \theta_j - \theta_k$ – the difference in the angles of orientation of links $j, k = \{4, 5, 6, 7\}$,

The above observation perfectly fits the manipulator $3RTR$ described in [9]. In order to solve the manipulator's kinematics, one must determine the velocity of the point M (Figure 3b) and then calculate the velocities of the other points of end-effector. The velocity of the point M is determined by solving the following system of vector equations:

$$\begin{cases} \overline{\mathbf{v}_M} = \overline{\mathbf{v}_G} + \overline{\mathbf{v}_{MG}}, \\ \overline{\mathbf{v}_M} = \overline{\mathbf{v}_H} + \overline{\mathbf{v}_{MH}}, \end{cases} \quad (4)$$

Table. Jacobian determinants

<p>3 RRR</p>	<p>3 TRR</p>	
$\det(\Phi_q) = l_4 l_5 l_6 [\sin\Theta_{5,6} (-{}^7x_G \sin\Theta_{4,7} + {}^7y_G \cos\Theta_{4,7}) + \sin\Theta_{6,4} (-{}^7x_H \sin\Theta_{5,7} + {}^7y_H \cos\Theta_{5,7}) + \sin\Theta_{4,5} (-{}^7x_K \sin\Theta_{6,7} + {}^7y_K \cos\Theta_{6,7})]$		(5)
<p>3 RRT</p>	<p>3 TRT</p>	
$\det(\Phi_q) = \sin\Theta_{5,6} (x_4 \cos\Theta_4 + y_4 \sin\Theta_4) + \sin\Theta_{6,4} (x_5 \cos\Theta_5 + y_5 \sin\Theta_5) + \sin\Theta_{4,5} (x_6 \cos\Theta_6 + y_6 \sin\Theta_6)$		(6)
<p>3 RTR</p>	<p>3 TTR</p>	
$\det(\Phi_q) = \sin\Theta_{5,6} [{}^7x_G \cos\Theta_{4,7} + {}^7y_G \sin\Theta_{4,7}] + \sin\Theta_{6,4} [{}^7x_H \cos\Theta_{5,7} + {}^7y_H \sin\Theta_{5,7}] + \sin\Theta_{4,5} [{}^7x_K \cos\Theta_{6,7} + {}^7y_K \sin\Theta_{6,7}]$		(7)

where:

$$\begin{aligned} \overline{\mathbf{v}_G} &= \overline{\mathbf{v}_D} + \overline{\mathbf{v}_{GD}}, & \overline{\mathbf{v}_D} &= \overline{\mathbf{v}_A} + \overline{\mathbf{v}_{DA}}, & \overline{\mathbf{v}_{DA}} &= \overline{\mathbf{v}_{41}}, \\ \overline{\mathbf{v}_H} &= \overline{\mathbf{v}_E} + \overline{\mathbf{v}_{HE}}, & \overline{\mathbf{v}_E} &= \overline{\mathbf{v}_B} + \overline{\mathbf{v}_{EB}}, & \overline{\mathbf{v}_{EB}} &= \overline{\mathbf{v}_{52}}. \end{aligned} \quad (8)$$

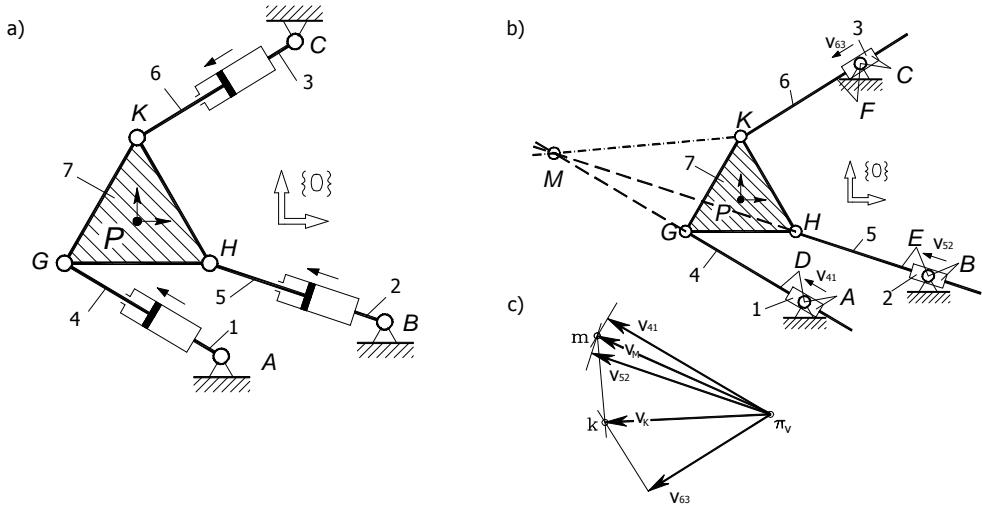


Fig. 3. Kinematic scheme of the manipulator 3RTR (a), equivalent mechanism (b), velocity diagram (c)

Hence after substituting Equations (4) and (8) we arrive at:

$$\begin{cases} \overline{\mathbf{v}_M} = \overline{\mathbf{v}_{41}} + \overline{\mathbf{v}_{GD}} + \overline{\mathbf{v}_{MG}}, \\ \overline{\mathbf{v}_M} = \overline{\mathbf{v}_{52}} + \overline{\mathbf{v}_{HE}} + \overline{\mathbf{v}_{MH}}. \end{cases} \quad (9)$$

In the system of Equations (9), vectors \mathbf{v}_{41} and \mathbf{v}_{52} and the direction of vector sums $\mathbf{v}_{GD} + \mathbf{v}_{MG}$ and $\mathbf{v}_{HE} + \mathbf{v}_{MH}$ are known, which allows the velocity of the point M (Figure 3c) to be determined. Then the velocity of the point K (Figure 3c) is obtained from this system of equations:

$$\begin{cases} \overline{\mathbf{v}_K} = \overline{\mathbf{v}_{63}} + \overline{\mathbf{v}_{KF}}, \\ \overline{\mathbf{v}_K} = \overline{\mathbf{v}_M} + \overline{\mathbf{v}_{KM}}. \end{cases} \quad (10)$$

Having solved the system of Equations (10), one can calculate the velocity of the point K and then the other end-effector velocities (including the velocity of the point P). When vectors \mathbf{v}_{KF} and \mathbf{v}_{KM} are parallel to each other, the velocity of none of the effector points can be determined. This happens in the case of the configurations shown

in Figure 4 [9]. A singular configuration occurs when the normals to the velocity directions \mathbf{v}_{GD} , \mathbf{v}_{HE} , \mathbf{v}_{KF} intersect at one point (Figure 4a) or are parallel (Figure 4b).

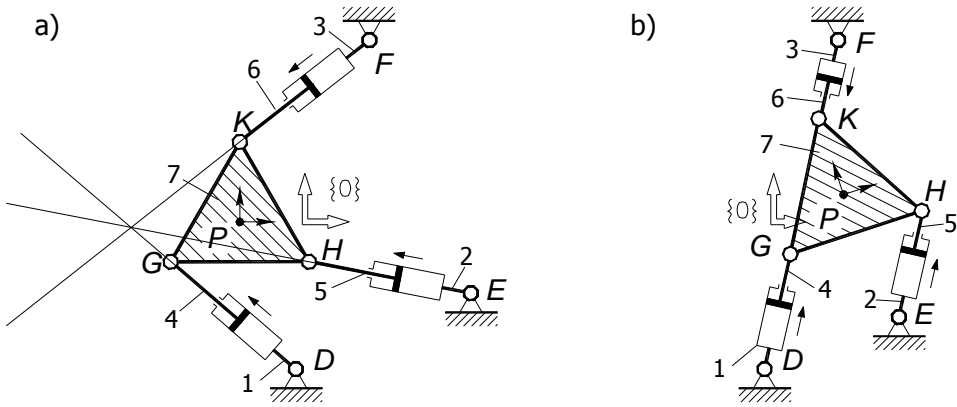


Fig. 4. Singular configurations of manipulator 3RTR

5. Singular configurations within workspace – auxiliary mechanisms

The determination of a singular form of configuration (on the basis of the determinant or Assur points) is the first step only. Then singular configurations against the background of the workspace must be determined. This is a complex problem since the determinant is nonlinearly dependent on the position parameters.

The singular configurations of manipulators with a known geometry are mostly determined through a numerical search of the entire workspace and by calculating the Jacobian determinant. But this is ineffective and laborious. The generalization about the conditions of the occurrence of singular configurations in the systems considered allows an effective and quick determination of the configurations. For this purpose auxiliary mechanisms based on the geometrical interpretation of the singular configurations should be introduced [10]. By determining all the possible positions of the auxiliary mechanisms it is possible to determine all the singular configurations of a manipulator – the trajectory of auxiliary mechanism point P marks out the manipulator's singular configurations.

Figure 5 shows auxiliary mechanisms for the manipulator 3TRR. The geometry of the base and that of links 1–7 corresponds to the manipulator's geometry, while links 8, 9, 10 are responsible for a peculiar configuration: the intersection of appropriate directions and parallelism for the cases shown in Figures 5a and 5b, respectively [10].

By analogy to the auxiliary mechanisms presented one can propose auxiliary mechanisms for the other manipulators.

The advantage of auxiliary mechanisms lies in the fact that singular configurations can be quickly and effectively determined against the background of the workspace.

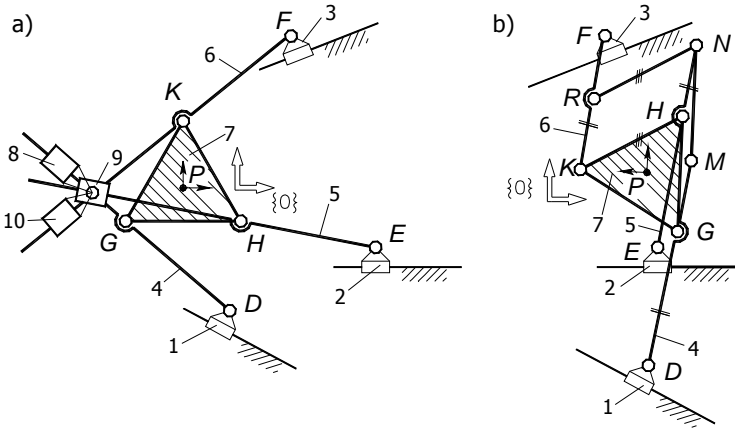


Fig. 5. Auxiliary mechanisms for determining singular configurations characterized by:
 a) intersection, b) parallelism of normals to relative velocities

A detailed analysis of the auxiliary mechanisms allows one to formulate further conclusions. The auxiliary mechanism shown in Figure 5a has two degrees of freedom. Consequently, the orientation of link 7 and one coordinate (x_P or y_P) of the point P can be defined arbitrarily. Even if the effector has a constant orientation, the mechanism is still capable of motion. The point P plots a trajectory which forms a continuous curve of singular positions for a given orientation of end-effector link 7. By successively changing the orientation of link 7 and each time determining the trajectory of the point P one obtains several curves which represent the singular configurations. In order to determine singular configurations, it is most convenient to present them in the system $XY\theta_7$ since the locations of singular configurations change with the orientation of the effector. Hence it follows that the singular configurations for the whole workspace form a continuous surface in the system $XY\theta_7$. This means that the manipulator's workspace delimited by the singularities of the inverse problem cannot be fully utilized without disassembly. Thus one can say that the available workspace of a given planar parallel manipulator is delimited by the singularities of both the forward and inverse kinematic problems.

The auxiliary mechanism shown in Figure 5b has one degree of freedom. As the orientation of the end-effector changes, the position of the point P changes in a specific way. Thus singular configurations characterized by parallelism of appropriate straight lines occur less often.

6. Conclusion

The results of research aimed at formulating generalizations covering possibly the largest group of 3 DOF planar parallel systems with driving links in each of the three legs have been presented.

Compact relations for the Jacobian matrix determinants for symmetrical systems with driving links at the base have been derived. The form of the equations depends on the structure of the system fragment which remains after the base and the driving links are removed. The system fragments form the so-called 3rd class Assur groups [6]. A detailed analysis of the expressions for the Jacobian determinants showed that singular configurations occur when the Assur points coincide.

The approach presented allows one to determine singular configurations by classical kinematic analysis methods without calculating the Jacobian matrix determinant and to define conditions in which equation $\det(\Phi_q) = 0$ is fulfilled. As a result, the conditions of the occurrence of singular configurations and the singular configurations themselves can be easily determined and interpreted.

The finding that the singular configurations of the forward kinematic problem occur only when the Assur points coincide served as the basis for defining auxiliary mechanisms which simplify the analysis of singular configurations.

The research results presented may contribute to a wider use of planar parallel manipulators. The demonstrated simple way of determining singular configurations and their nature will facilitate the design of such manipulators.

References

- [1] Gosselin C., Angeles J.: *Singularity analysis of closed-loop kinematic chains*, IEEE Trans. On Robotics and Automation, 1990, 6(3).
- [2] Gosselin C., Sefrioui J.: *Polynomial solutions for the direct kinematic problem of planar three-degree-of-freedom parallel manipulator*, International Conference on Advanced Robotics, Pisa, 1991.
- [3] Knapczyk J., Morecki A.: *Podstawy robotyki. Teoria i elementy manipulatorów i robotów*, WNT, 1999.
- [4] Daniali H.R.M., Zsombor-Murray P.J., Angeles J.: *Singularity analysis of a general class of planar parallel manipulators*. IEEE Int. Conf. On Robotics and Automation, Nagoya, May 25–27, 1995.
- [5] Shabana A.A.: *Computational Dynamics*, John Wiley & Sons, Inc., 1995.
- [6] Tsai L-W.: *Robot analysis. The mechanics of serial and parallel manipulators*, John Wiley & Sons, Inc., New York, 1999.
- [7] Gronowicz A., Prucnal-Wieszort M.: *Położenia osobliwe manipulatorów równoległych płaskich*, XIX Konferencja Naukowo-Dydaktyczna Teorii Maszyn i Mechanizmów, Kraków, 12–14 października, 2004.
- [8] Miller S.: *Układy kinematyczne. Podstawy projektowania*, WNT, 1988.
- [9] Wender Ph., Chablat D.: *Workspace and assembly modes in fully-parallel manipulators: a descriptive study*. *Advances in Robot Kinematics: Analysis and Control*, Kluwer Academic Publishers, 1998.
- [10] Prucnal-Wieszort M.: *Wyznaczanie położeń manipulatorów równoległych płaskich na tle strefy roboczej*, XIX Konferencja Naukowo-Dydaktyczna Teorii Maszyn i Mechanizmów, Kraków, 12–14 października, 2004.

Położenia osobliwe płaskich manipulatorów równoległych

W artykule podjęto problem wyznaczania położenia osobliwych grupy płaskich manipulatorów równoległych o trzech stopniach swobody, których człony tworzą pary obrotowe i postępowe. Przedstawiono wyrażenia opisujące wyznaczniki macierzy Jacobiego dla wybranych mechanizmów. Forma otrzymanych równań zależy od budowy strukturalnej wewnętrznej części manipulatorów tworzących tzw. grupy Assura III klasy. Analiza otrzymanych wyrażeń pokazała, że położenia osobliwe odpowiadają tym, w których punkty Assura pokrywają się. Zaprezentowane podejście umożliwia określenie konfiguracji osobliwych jedynie na podstawie klasycznych metod analizy kinematycznej, bez obliczania wartości wyznacznika macierzy Jacobiego i definiowania warunków zerowania się tego wyrażenia. Ponadto zaproponowano metodę określania położenia osobliwych na podstawie trajektorii punktu charakterystycznego mechanizmów pomocniczych. Przedstawione wyniki badań ułatwiają określanie warunków występowania położenia osobliwych.

Effect of the conditioning of CBN wheels on the technological results of HS 6-5-2 steel grinding

M. URBANIAK

Technical University of Łódź, Stefanowskiego 1-15, 90-537 Łódź

The paper deals with the comparison of grinding results achieved with vitrified and resin-bonded superhard wheels during the grinding of high-speed steel. Several dressing conditions were applied. Grinding results were determined on the basis of the measurements of grinding efficiency, grinding forces and surface roughness achieved during the process.

Keywords: *CBN grinding wheels, resinoid bond, vitrified bond, dressing*

1. Introduction

The forming of functional properties of cubic boron nitride (CBN) wheels is one of the most difficult tasks, when an operational use of superhard wheels is taken into account [1]. For that reason these wheels still are not used on a large scale. The reconditioning of CBN wheels needs to be carried out carefully for all types of bonds, also because of high prices of superhard wheels, especially vitrified wheels.

High hardness of CBN requires application of rotary diamond tools during conditioning process of vitrified wheels. In this way, it is possible to minimize wear of dressing tool. In-feed dressing is realized in a few passes with small depths of the cut, which results in smooth grinding wheel cutting surface (GWCS). Smooth surface should be "opened" in another operation in order to achieve an appropriate, stable stereometry. "Opening" can be done in an initial grinding process where maximum efficiency is not required. This problem was described in [2].

The application of rotary diamond dressers in conventional grinding machines is associated with additional expensive equipment. It would be useful to evaluate the possibilities of applying non-rotary diamond tools in these machines in the case of superhard wheels. And this problem is discussed below.

The second group of superhard wheels is represented by resin-bonded wheels, which might replace vitrified wheels due to their lower prices and easier reconditioning. The rigidity (Young's modulus) of resin-bonded wheels is about twenty times smaller than that of vitrified ones. The rigidity of the connection between grain and bond is also three times smaller compared with metal-bonded wheels.

In this case, superhard grains may deflect significantly.

This allows us to achieve better surface finish but on the other hand this causes difficulties in the precise reconditioning and stabilizing the wheel properties during grinding process.

Table 1. Dressing conditions

Research stand	Surface grinder SPG 30 × 80							
Wheel characteristics ($\varphi = 350$ mm)	1A1-1 LKB 125/100 K 47 C1 1A1-1 LKB 63/50 K 47 C1			1A1-1 LKB 63/50 B23				
	Dressing conditions			Conditioning parameters				
Dressing version	1	2	3	4	5	6	7	8
Type of dresser	Single-point diamond M1010						Dressing wheel 37C60M5V	
Speed of dressed wheel [m/s]	26.5						2	
Width of dresser [mm]	0.85 – 1.05			1.05 – 1.20			–	–
Number and type of dressing passes	Sharpening, 3	Sharpening, 2 Spark out, 5	Sharpening, 2 Touch dressing, 10	Sharpening, 5			Truing, 5 Sharpening, 3	
In-feed dressing [mm]	0.02	0.02 / 0	0.02 / 0.001	0.02				
Overlap ratio	2.5						6	
Speed [m/s] and direction of rotation of dressing wheel	–	–	–	–	–	–	11 backward	
Clearing tool	–	–	–	Armco iron			–	Steel brush
Number of passes and in- feed brushing	–	–	–	20 × 0.01 [mm] (through)	2 [μm/s] (plunge)	–	3 × 0.02 [mm] (through)	
Speed [m/s] and direction of rotation of clearing tool	–	–	–	–	–	5.8 backward		–

The dressing process allowing the whole grains to be pull out of the bond¹ is responsible for the above mentioned limitations. Only those grains, which slightly protrude from the bond layer, remain on the wheel cutting surface. Hence, in an initial phase of grinding, the significant influence of a bond–workpiece couple on grinding result can be observed.

This problem was analysed in several publications concerning dressing process with different diamond dressers. The author's publication [3] gives a detailed description of this process.

An interesting method of dressing (with a rotating brush) was described in CIRP [4]. According to this publication, a significant influence of functional properties of resin-bonded wheels on dressing was possible. Thus the method was applied in author's own research [5].

2. Methods and conditions of research

The aim of the research was to determine the influence of some selected dressing methods on grinding results with application of CBN wheels. Vitrified wheels were dressed with a single-point diamond dresser. According to previous research [6] favourable dressing conditions were accepted (the shape of the dressed layer a_d/p_d and the overlap ratio k_d). This enabled an investigation of the influence of grinding intensity (based on specific volumetric grinding output Z') on grinding result.

Resin-bonded wheels were conditioned by means of several methods (dressing and clearing – bond removal process). Dressing and clearing conditions are presented in Table 1.

As wide industrial application of the wheels mentioned should be considered, several grinding tests have been carried out on HS 6-5-2 tool steel with different parameters (Table 2).

Table 2. Grinding conditions

Grinding speed	[m/s]	26.5
Feed (workpiece)	[m/s]	0.12–0.33
In-feed grinding	[μm]	5–20
Specific volumetric grinding output	[$\text{mm}^3/(\text{mm}\cdot\text{s})$]	0.58–6.66
Number of grinding passes		30
Coolant		oil emulsion 5%
Workpiece		HS 6-5-2 (63–65 HRC)

Previous publications have shown that the influence of dressing conditions decreases as the grinding process continues. Significant changes could be observed at the

¹ Diamond grains achieved by CVD method (chemical reactions in plasma) are less resistant to chipping during dressing and grinding due to crystallographic defects and create new cutting edges.

beginning of the process. It was found that after 20 grinding passes, the state of GWCS stabilized. Thus grinding results were measured after 30 grinding passes.

3. Examination and analysis of research results

Research results were examined based on:

- visual inspection of ground surface focused on grinding burn,
- average value of the surface roughness parameter Ra_{av} ,
- the values of the grinding force components F_n and F_t .

The analysis of the results achieved was carried out in terms of a specific volumetric grinding output Z' described by the following equation:

$$Z' = a_e \cdot V_{ft} \quad [\text{mm}^3/(\text{mm}\cdot\text{s})]. \quad (1)$$

As an example, the research results in the case of resin-bonded wheel being dressed with silicon carbide wheel and cleared with steel brush are shown in Figures 1 and 2. The figures presented the range of the grinding output without burns (Figure 1) and the variation of the grinding force components (Figure 2).

Based on the results obtained the analysis of effectiveness of grinding of HS 6-5-2 tool steel was carried out in the area of the most effective grinding, without burns [5].

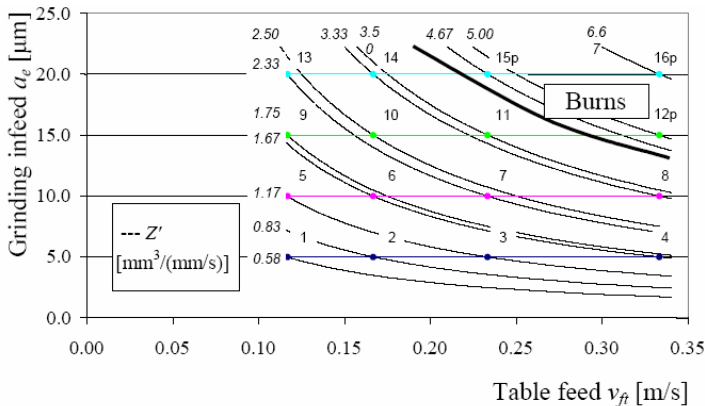


Fig. 1. Range of operation without grinding burns. Grinding wheel LKB 63/50 B23 after dressing (dressing wheel and clearing steel brush)

Grinding results achieved with different grain sizes, after dressing without spark out passes, are shown in Figure 3.

Grinding wheel with greater grain size ($125 \mu\text{m}$) was able to achieve the efficiency Z' (grinding output) of about $3.50 \text{ mm}^3/(\text{mm}\cdot\text{s})$. The surface roughness parameter Ra did not exceed $0.67 \mu\text{m}$. In the case of the grain size of $63 \mu\text{m}$, the grinding output $Z' = 2.33 \text{ mm}^3/(\text{mm}\cdot\text{s})$, while Ra did not exceed $0.47 \mu\text{m}$.

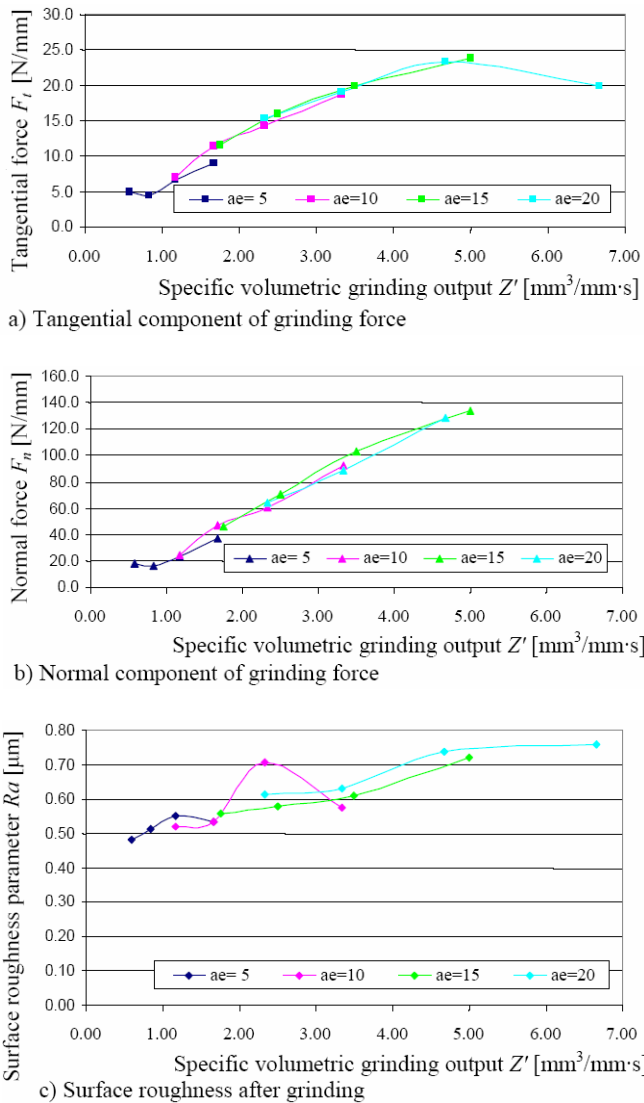


Fig. 2. Grinding results versus specific volumetric grinding output. Grinding wheel LKB 63/50 B23 after dressing (dressing wheel and clearing steel brush)

The components of grinding force were smaller in the case of a greater grain size (by about 20% smaller in the case of tangential force and by about 10% smaller in the case of normal component).

In the next step, the grinding results achieved with vitrified wheels were compared. In this part of research, three kinds of dressing with single-point diamond dresser were employed (Figure 4).

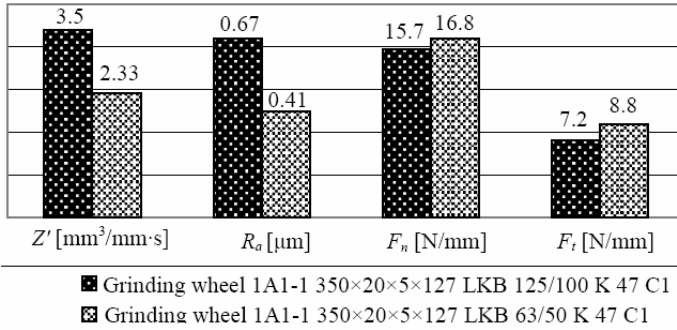


Fig. 3. Influence of grain size on grinding result

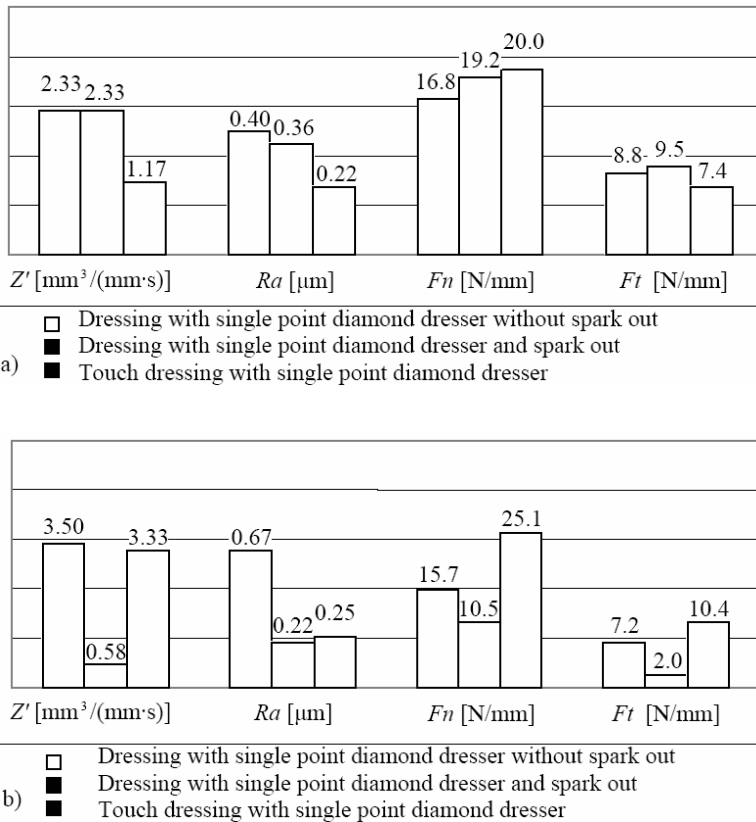


Fig. 4. Influence of dressing method on grinding output with application of CBN vitrified wheel with the grain size of 63 µm (a) and 125 µm (b)

Dressing without spark out passes enabled grinding with the highest output. In this case, the components of grinding force were the smallest and the surface roughness

parameter Ra reached the highest value. Spark out passes in the case of the grain size of $63\ \mu\text{m}$ (Figure 4a) did not change the grinding output. However grinding force increased by about 10%, and the surface roughness parameter decreased by about 10% at the same time. This was the result of a slight flattening of GWCS. Spark out passes in the case of $125\ \mu\text{m}$ grain size (Figure 4b) caused a significant flattening of cutting grains which led to a visible decrease in the grinding effectiveness. In this case, the lowest value of the surface roughness parameter Ra was reached.

Touch dressing gave good results in the case of the grain size of $125\ \mu\text{m}$. The grinding output was very close to the highest value, and the surface roughness parameter reached the smallest value ($Ra = 0.25\ \mu\text{m}$). However, the grinding force increased by about 30%.

The same variant of dressing did not bring about any beneficial changes in the case of grains of smaller size, i.e., $63\ \mu\text{m}$. The grinding output decreased by about 50% in comparison to the outputs in other dressing variants. Also a normal component of the grinding force was higher. Nevertheless the surface roughness was very small ($Ra = 0.22\ \mu\text{m}$).

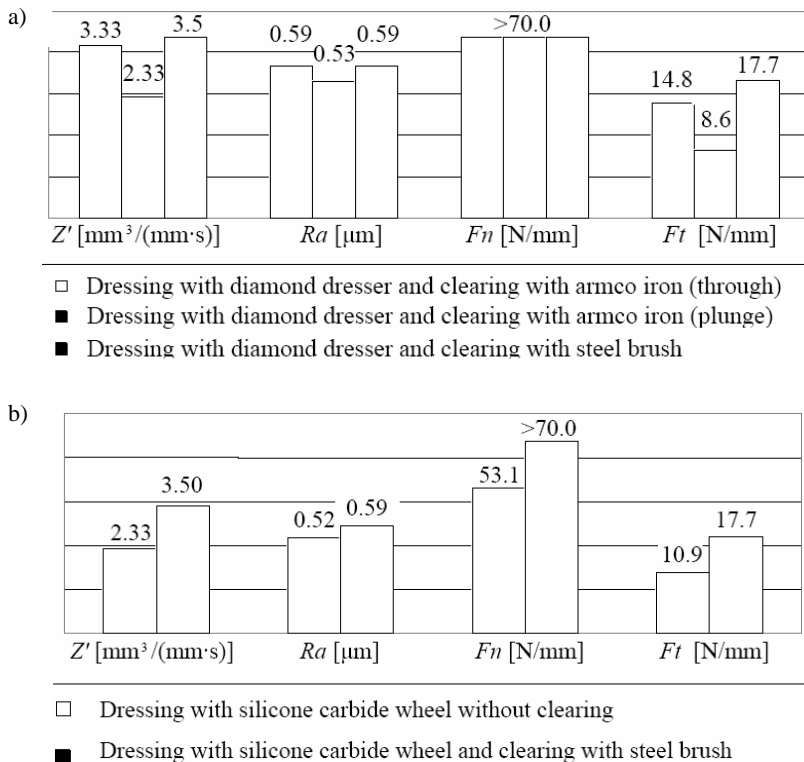


Fig. 5. Influence of conditioning method on grinding output in the case of CBN resin-bonded wheel. Dressing with diamond dresser (a), dressing with silicone carbide wheel (b)

The analysis of grinding results after dressing with spark out passes and after touch dressing shows that the problems of CBN grain chipping and the interaction between grains and dressing tool (when the dimension of dressing width is similar to the grain size) are important. The problems will be investigated in further research.

In the next step, the author analysed the grinding output achieved with the application of resin-bonded wheel, dressed in two ways and cleared in another three ways (Figure 5).

Dressing process carried out with diamond dresser without additional clearing operation did not bring about any successful results in the case of resin-bonded wheel. More detailed description of this problem can be found in [7]. Among the clearing methods applied the best results were achieved with steel brush and during grinding of Armco iron (Figure 5a). After this operation, a satisfactory surface finish ($Ra = 0.59 \mu\text{m}$) was achieved.

Tangential force component increased by about 20% in the case of using a steel brush. Normal components reached high values but did not cause grinding burns.

Dressing with silicone carbide wheel (Figure 5b) and steel brush clearing also resulted in high effectiveness of HS 6-5-2 tool steel grinding. Excluding a clearing caused a decrease in the grinding effectiveness by about 30%. Also two other parameters measured decreased: by 8% in the case of surface roughness and by 25% in the case of grinding force. Similar results were obtained after dressing with diamond and clearing with Armco iron.

4. Summary

Grinding outputs achieved with application of CBN resin-bonded wheel (the grain size of $63 \mu\text{m}$) are similar to those achieved with application of CBN vitrified wheel (the grain size of $125 \mu\text{m}$). However, in the case of vitrified wheel smaller values of the surface roughness parameter were achieved (if touch dressing was applied). Moreover, the grinding forces were significantly smaller.

Acknowledgement

The research was carried out with the help from the Company of EUROPOL, which sold CBN wheels at the low price.

References

- [1] Gołabczak A.: *Metody kształtowania właściwości użytkowych ściernic*, Wydawnictwo Politechniki Łódzkiej, Monografie, Łódź, 2004.
- [2] Urbaniak M.: *Czynna powierzchnia ściernicy w początkowym okresie szlifowania, Aktualne problemy obróbki ściernicy*, praca zbiorowa, Kraków–Łopuszna, 2001, str. 181–188.
- [3] Urbaniak M.: *Wpływ kondycjonowania ściernicy CBN ze spoiwem żywicznym szczotką stalową na jakość i wydajność szlifowania stali SW7M*, Materiały XXVII Naukowej Szkoły Obróbki Ściernicy, Koszalin, 2004, str. 145–152.

-
- [4] Inasaki I.: *A new preparation method for resinoid bonded CBN wheels*, Annals of the CIRP, 1990, Vol. 39/1, pp. 317–320.
- [5] Starczyk A.: *Analiza wpływu rodzaju spoiwa ściernicy na efektywność procesu szlifowania stali SW7M*, praca dyplomowa, Politechnika Łódzka, 2003.
- [6] Urbaniak M.: *Kształtowanie potencjału użytkowego ceramicznych ściernic CBN obciążaczem diamentowym jednoziarnistym*, Materiały XXVII Naukowej Szkoły Obróbki Ściernej, Koszalin, 2004, str. 139–144.
- [7] Urbaniak M.: *Analiza właściwości eksploatacyjnych ściernicy ze ścierniwem CBN i spoiwem żywicznym*, Materiały XXVI Naukowej Szkoły Obróbki Ściernej, Łódź, 2003, str. 117–124.

Wpływ kondycjonowania ściernic z azotku boru na efekty technologiczne szlifowania stali HS 6-5-2

Porównano wyniki szlifowania narzędziowej stali szybko tnącej ściernicami supertwardymi ze spoiwem ceramicznym i żywicznym. Stosowano różne warunki kondycjonowania ściernic. Wynik szlifowania określano na podstawie osiągniętej wydajności obróbki, wartości siły szlifowania oraz chropowości powierzchni przedmiotów po obróbce.

Assessment of ultimate bearing capacity of RC sections affected by mineral oil

T. BŁASZCZYŃSKI, J. ŚCIGAŁŁO

Poznań University of Technology, ul. Piotrowo 5, 60-965 Poznań

Bearing capacity of RC sections subjected to bending and eccentric compression and being under the influence of oil is evaluated. Two states of oiling up are considered: non-oiling up state and oiling up state after 12 months of subjecting the RC section to oil influence. Ultimate bearing capacity of reinforced sections influenced by mineral oils is evaluated numerically based on the diagrams of the limit state interaction. The analysis is carried out for rectangular section with tension and compression reinforcement. In the case of oiling up state, the bearing capacity of a section decreases compared with that being in non-oiling state.

Keywords: *RC section, oil influence, ultimate bearing capacity, diagram of limit state interaction*

1. Introduction

The bearing capacity of RC sections depends not only on the strength and deformation parameters of concrete, but also on some environmental factors. Of all environmental factors being insufficiently recognised, a physicochemical factor is associated with organic active surface molecules. Crude oil products usually comprise some of them. We deal with chemical corrosion in the case of a high neutralisation number (higher than 0.25 mg KOH/g). In technical literature, the effect of crude oil products on concrete is classified either as non-harmful or only mildly harmful, but there is evidence of serious damage caused by these products [1].

2. The influence of mineral oils on concrete

Long-term laboratory experiments have been conducted to assess the changes of physicommechanical characteristics of oil-contaminated concrete. A compressive strength was determined using 100 mm cubes, according to PN-EN 12390-1:2001, for concrete of type B25 as most commonly used for industrial RC structures in Poland (5 specimens, s_{fc} ranged from 0.84 to 2.87, v_{fc} ranged from 2.25% to 6.99%). After 28 days an average compressive strength f_{cm} of concrete was 29.8 MPa. The water to cement ratio was 0.59, and the aggregate to cement ratio was 6.70 [2].

Concrete was impregnated with most commonly used industrial oils of different kinematic viscosities, namely turbine oil TU-20 (81 mm²/s), machine oil M-40 (211 mm²/s) and hydraulic oil H-70 (383 mm²/s). The neutralisation numbers of these oils are low, ranging between 0.05 and 0.075 mg KOH/g. Two months after casting

concrete specimens were at first exposed to oil attack, and then they were examined every 4 or 12 months over a total period of 72 months. The control specimens (samples) were additionally examined after 28 days and 2 months (Figure 1). Two-month specimens were exposed to oil attack at an average compressive strength of concrete $f_{cm} = 37.35$ MPa.

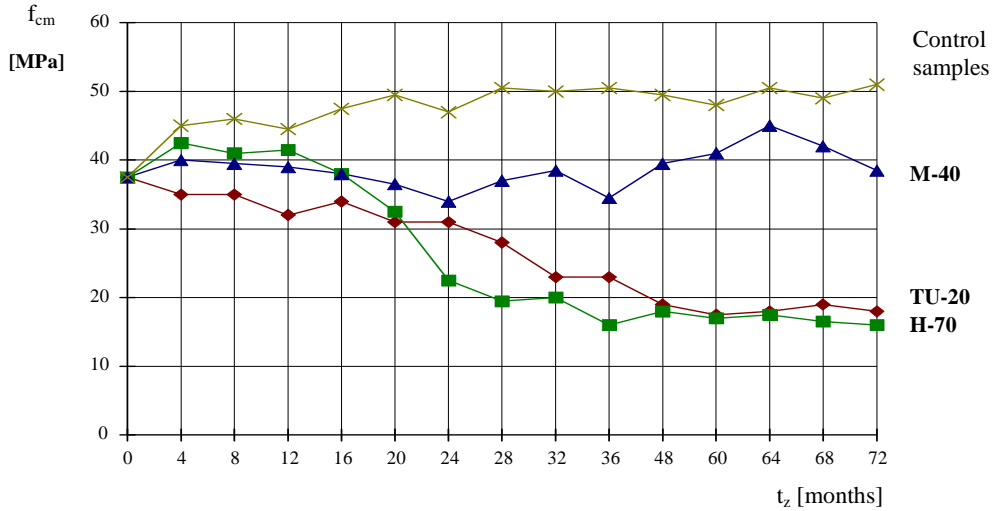


Fig. 1. Variation of concrete B25 compressive strength during the period of exposure to H-70, TU-20 and M-40 oils

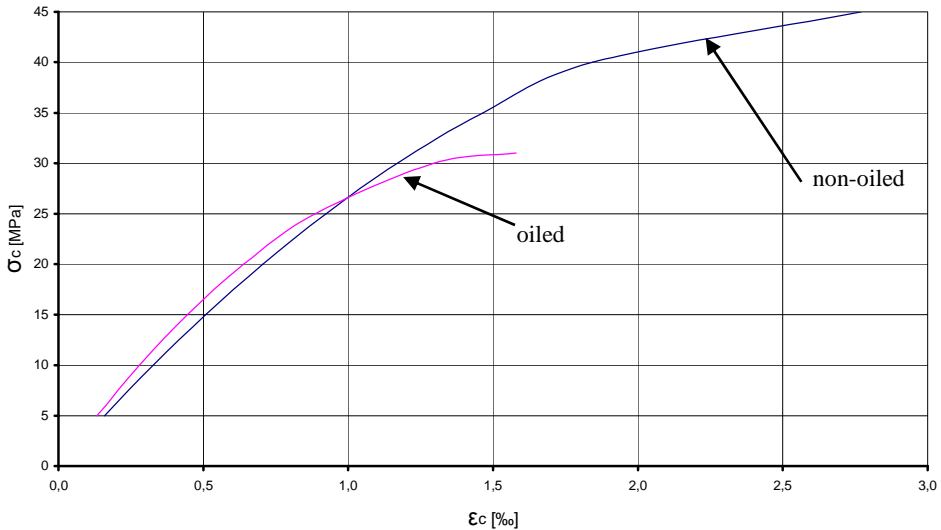


Fig. 2. $\sigma_c - \epsilon_c$ diagram for concrete B25 non-oiled and oiled by oil TU-20

$$M = \int_{-h_1}^{+h_2} b(y) \sigma_c(y) [\varepsilon(y)] y dy + N_{S2}(h_2 - a_{S2}) + N_{S1}(h_1 - a_{S1}). \quad (2)$$

The following assumptions were made in calculations of the bearing capacity:

- plane sections remain plane,
- strains of tension and compression reinforcement are the same as strains of the surrounding concrete,
- in the section under axial compression the concrete compressive strain is limited to ε_{c1} ,
- in the sections compressed in part, a limit concrete strain is assumed to be ε_{cu} ,
- the tensile strength of concrete is neglected,
- the relation $\sigma_c - \varepsilon_c$ for concrete is non-linear (Figure 4),
- the relation $\sigma_c - \varepsilon_c$ for steel is based on the formulae shown in Figure 5.

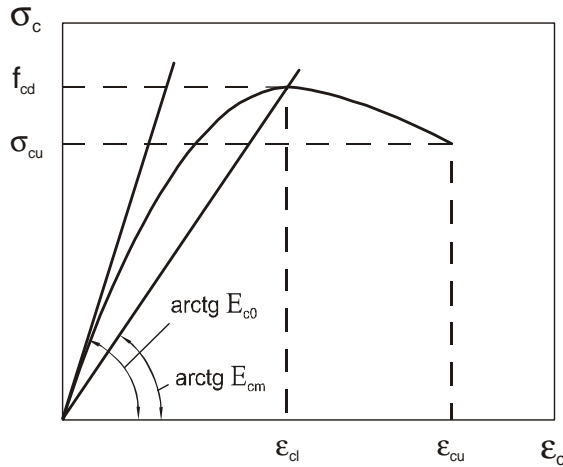


Fig. 4. Relationship $\sigma_c(\varepsilon_c)$ for concrete

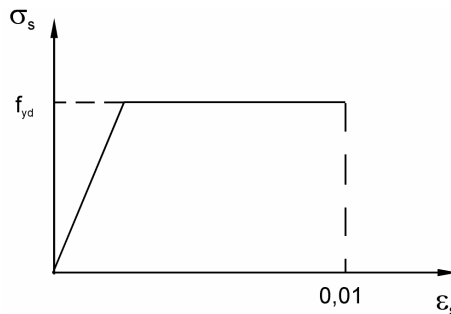


Fig. 5. Assumed relationship $\sigma_s(\varepsilon_s)$ for reinforced steel

The relationship $\sigma_c - \varepsilon_c$ for concrete in compression could be expressed by the Saenz equation. This solution is the best way of evaluating the limit state interaction diagrams, because it very slightly influenced the diagrams, i.e., only up to 5% [4]. The Saenz solution is given below [5]:

$$\sigma(\varepsilon) = \frac{\varepsilon_c}{A + B\varepsilon_c + C\varepsilon_c^2 + D\varepsilon_c^3}, \quad (3)$$

where:

$$A = \frac{1}{E_{c0}}, \quad R = \frac{R_E(R_f - 1)}{(R_E - 1)^2} - \frac{1}{R_E},$$

$$B = \frac{R_E + R - 2}{R_E f_c}, \quad R_E = \frac{E_{c0}}{E_{cm}},$$

$$C = -\frac{2R - 1}{R_E f_c \varepsilon_{c1}}, \quad R_f = \frac{f_c}{\sigma_{cu}},$$

$$D = \frac{R}{R_E f_c \varepsilon_{c1}^2}, \quad R_\varepsilon = \frac{\varepsilon_{cu}}{\varepsilon_{c1}}.$$

From the above equations it can be concluded that in order to evaluate the bearing capacity of RC section using the limit state interaction diagrams based on the Saenz relationship $\sigma_c - \varepsilon_c$, we have to know the $\varepsilon_{c1}/\varepsilon_{cu}$ ratio. The remaining elements could be taken from a simple $\sigma_c - \varepsilon_c$ concrete compression test.

The limit state interaction diagrams for concrete sections have been drawn based on the equilibrium conditions at the limit bearing capacity state (Figure 6).

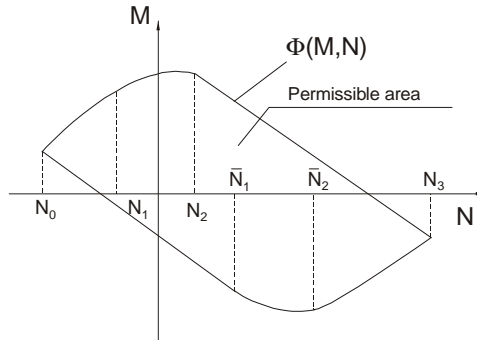


Fig. 6. The limit state interaction diagram for doubly reinforced RC section at $A_{s1} > A_{s2}$

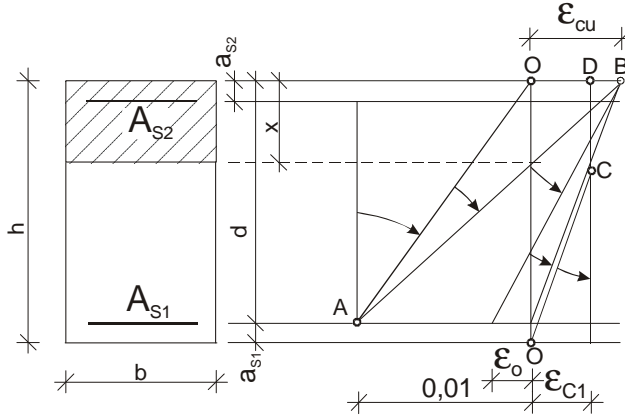


Fig. 7. The strains in RC section at limit bearing capacity

The M, N - coordinates in the interaction diagram (Figure 6) have been defined from equilibrium conditions (1), (2), taking advantage of the Gauss quadratic formula in numerical integration. According to Figure 7 showing the strains in RC section, appropriate ranges of coordinates were adopted for the curves of the limit state diagram:

- range 1a

$$-\infty < x \leq 0,$$

$$\varepsilon_{S1} = 0.01, \quad \varepsilon_{S2} = \varepsilon_{S1} \cdot \frac{x + a_{S2}}{x + d}; \quad (4)$$

- range 1b

$$0 < x \leq d \cdot \frac{\varepsilon_{cu}}{0.01 + \varepsilon_{cu}},$$

$$\varepsilon_{S1} = 0.01, \quad \varepsilon_{S2} = \varepsilon_{S1} \cdot \frac{x - a_{S2}}{d - x}; \quad (5)$$

- range 2a

$$d \cdot \frac{\varepsilon_{cu}}{0.01 + \varepsilon_{cu}} < x \leq d \cdot \frac{\varepsilon_{cu}}{\frac{f_{yk}}{E_s} + \varepsilon_{cu}},$$

$$\varepsilon_{S1} = \varepsilon_{cu} \cdot \frac{d - x}{x}, \quad \varepsilon_{S2} = \varepsilon_{cu} \cdot \frac{x - a_{S2}}{x}; \quad (6)$$

• range 2b

$$d \cdot \frac{\varepsilon_{cu}}{\frac{f_{yk}}{E_s} + \varepsilon_{cu}} < x \leq d,$$

$$\varepsilon_{S1} = \varepsilon_{cu} \cdot \frac{d-x}{x}, \quad \varepsilon_{S2} = \varepsilon_{cu} \cdot \frac{x-a_{S2}}{x}; \quad (7)$$

• range 2c

$$d < x \leq h,$$

$$\varepsilon_{S1} = \varepsilon_{cu} \cdot \frac{d-x}{x}, \quad \varepsilon_{S2} = \varepsilon_{cu} \cdot \frac{x-a_{S2}}{x}; \quad (8)$$

• range 3

$$h < x < \infty,$$

$$\varepsilon_c = \frac{\varepsilon_{c1} \varepsilon_{cu} x}{h \varepsilon_{c1} + \varepsilon_{cu} (x-h)}, \quad \varepsilon_{S1} = \varepsilon_c \cdot \frac{x-d}{x}, \quad \varepsilon_{S2} = \varepsilon_c \cdot \frac{x-a_{S2}}{x}. \quad (9)$$

The M , N - coordinates were approximated using the n -th order polynomial. The order of the polynomial was chosen in such a way that the divergence in the approximation did not exceed 0.1%.

The divergence coordinate R_{ai} is defined as follows:

$$R_{ai} = \frac{|r_i - r_{ai}|}{r_i} \cdot 100 \leq 0.1, \quad (10)$$

where:

$r_i = \sqrt{N_i^2 + M_i^2}$, N_i , M_i - the i -th coordinates of the interaction diagram taken from numerical integration of equilibrium conditions,

$r_{ai} = \sqrt{N_{ai}^2 + M_{ai}^2}$, N_{ai} , M_{ai} - the coordinates of point of the intersection of the line crossing the origin of co-ordinates and the point N_i , M_i with approximation curve (the n -th order polynomial).

Based on these solutions Ścigałło designed KNG software in FORTRAN language for IBM PC [3]. KNG software enables calculation of percentage divergence between the areas determined at different geometrical or material parameters.

The numerical analysis of the bearing capacity of a section using the limit state interaction diagrams was carried out for non-oiling up and oiling up states. In order to compare the influence of oiling up on the bearing capacity of RC section, presented in

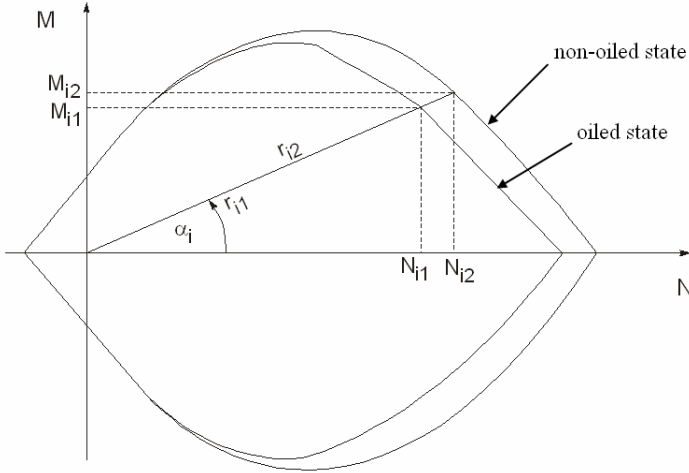


Fig. 8. Diagram for calculating the divergence between two bearing capacity areas

the form of limit state interaction diagram, the comparative divergence R_p was introduced in between the bearing capacity areas defined for concrete in non-oiling up and oiling up states (Figure 8):

$$R_{ip} = \frac{|r_{i1} - r_{i2}|}{r_{i1}} \cdot 100\% , \quad (11)$$

where:

$r_{i1} = \sqrt{N_{i1}^2 + M_{i1}^2}$, N_{i1} , M_{i1} – the coordinates of the point of intersection of line $M = a_i N$ (Figure 8) crossing the limit state interaction diagram No. 1 (oiling up state),

$r_{i2} = \sqrt{N_{i2}^2 + M_{i2}^2}$, N_{i2} , M_{i2} – the coordinates of the point of intersection of line $M = a_i N$ crossing the limit state interaction diagram No. 2 (non-oiling up state).

4. The ratio of $\varepsilon_{c1}/\varepsilon_{cu}$ for non-oiling up and oiling up concrete under compression

In order to define $\varepsilon_{c1}/\varepsilon_{cu}$ ratio, the $\sigma_c - \varepsilon_c$ relationship for compressed non-oiling up and contaminated concrete was tested. Cuboid specimens ($100 \times 100 \times 400 \text{ mm}^3$) according to PN-EN 12390-1:2001 are used for examination (Figures 9, 10). Based on available literature [6] and on my own tests for different types of concrete it can be

concluded that the optimum solution for the relationship $\sigma_c-\varepsilon_c$ is the value of loading velocity equal to $1.0 \mu\text{m/s}$.

In order to investigate the relationship $\sigma_c-\varepsilon_c$ and $\varepsilon_{c1}/\varepsilon_{cu}$ ratio, a universal hydraulic testing machine INSTRON 8505Plus was used. Such a powerful machine allows us to enforce the specimen loading in a typical way (applying the force assumed) or to create its assumed displacement and to search for the force produced in response. The force measurement and constraint were carried out with machine and control unit. The opposite sides and a mean of each specimen were measured (Figure 11). In the same way, the test results were analysed for non-oiled specimens (samples).

Strains were measured with two parallel Hottinger tensometers, type 150/120LY41, with the base of 150 mm. Tensometers were stuck to both opposite walls of the specimen parallel to the compressive force direction.



Fig. 9. Specimens of non-oiled concrete (samples) before and after the test

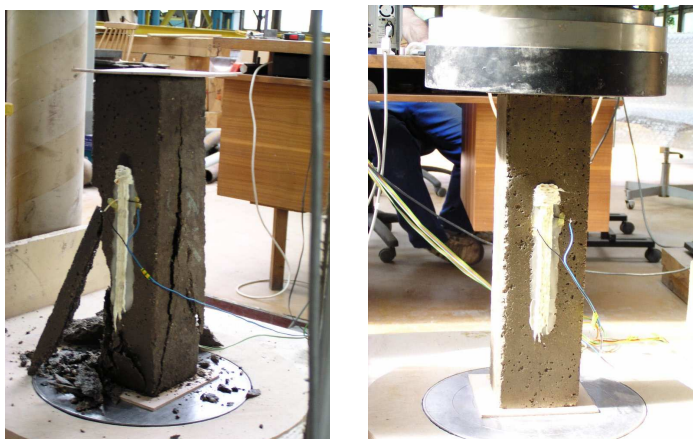


Fig. 10. Specimens of oiled concrete before and after the test

The strain measurement data were collected by Hottinger Baldwin Messtechnik measuring unit, type MGCplus, and software Catman 3.11 for system management, visualization and data handling. Before each test, the surfaces of the specimen being in contact with pressure plates were levelled.

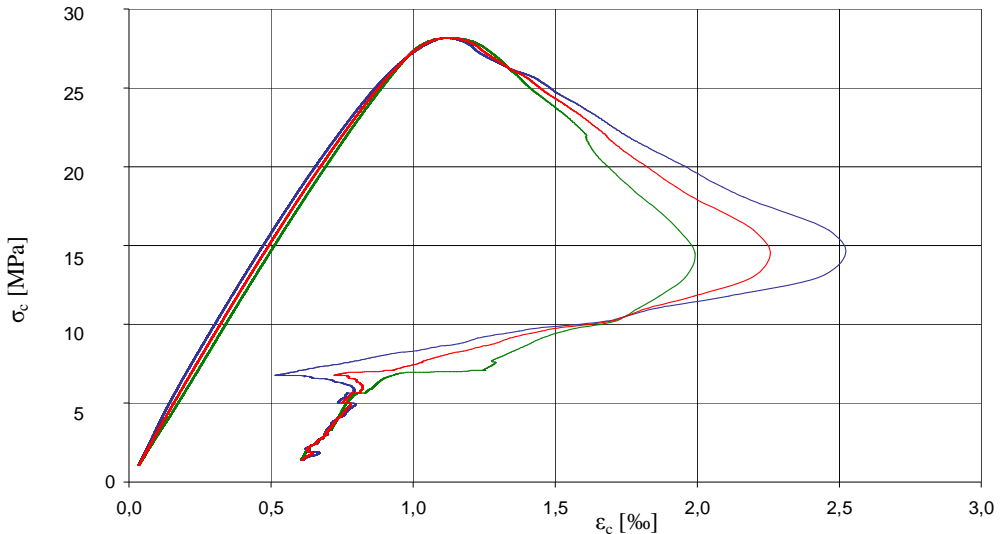


Fig. 11. The relationship $\sigma_c - \varepsilon_c$ for oiled concrete (measurement from the opposite sides and mean)

As a result of the tests we obtain the $\varepsilon_{c1}/\varepsilon_{cu}$ ratios for non-oiled concrete and for concrete contaminated with oil. They were respectively 0.75 ($s_{fc} = 0.019$, $v_{fc} = 2.58\%$) and 0.5 ($s_{fc} = 0.041$, $v_{fc} = 8.2\%$).

5. Numerical analysis

Ultimate bearing capacity of the singly and doubly reinforced RC sections influenced by mineral oil is defined numerically by the limit state interaction diagrams and KNG software. The numerical analysis of the bearing capacity of RC section is carried out in oiling up and non-oiling up states. This analysis is based on two conditions tested: non-oiling up and oiling up for 12 months (oil TU-20) (Figure 2). The results of tests are shown in Table 1.

As a result of the tests we obtain the $\varepsilon_{c1}/\varepsilon_{cu}$ ratios for non-oiled concrete and for concrete contaminated with oil. They were respectively 0.75 and 0.5.

Therefore:

- for oiled concrete (after 12 months of oiling)

$$\varepsilon_{cu} = \frac{\varepsilon_{c1}}{0.5} = \frac{0.001580}{0.5} = 0.003160 ;$$

- for non-oiled concrete (after 12 months)

$$\varepsilon_{cu} = \frac{\varepsilon_{c1}}{0.75} = \frac{0.002770}{0.75} = 0.003692.$$

Table 1. The results of $\sigma_{\chi} - \varepsilon_{\chi}$ tests for concrete B25

Stress [MPa]	Strain for concrete B25	
	Non-oiling up state	Oiling up state
5.00	0.000158	0.000133
10.00	0.000327	0.000279
15.00	0.000508	0.000445
20.00	0.000705	0.000639
25.00	0.000923	0.000885
30.00	0.001170	0.001296
31.00		0.00158
35.00	0.001464	–
40.00	0.001845	–
45.00	0.002770	–

We take into account a non-linear model of concrete that is based on the Saenz solution. The coefficients of the Saenz function were found by the numerical calculation using APROKS software designed by Z. Witkowski and given in Table 2.

Table 2. The coefficients of the Saenz function $\sigma_{\chi} - \varepsilon_{\chi}$

Value of coefficients	Concrete	
	Non-oiled	Oiled
<i>A</i>	$0.30397 \cdot 10^{-04}$	$0.25223 \cdot 10^{-04}$
<i>B</i>	$0.69065 \cdot 10^{-02}$	$0.95266 \cdot 10^{-02}$
<i>C</i>	$-0.48508 \cdot 10^{+01}$	$-0.20740 \cdot 10^{+00}$
<i>D</i>	$0.74099 \cdot 10^{+03}$	$0.27454 \cdot 10^{+04}$
<i>E_{c0}</i>	32898.0	39646.0
<i>ε_{c1}</i>	0.002770	0.001580
<i>f_c</i>	45.0	31.0

Rectangular concrete section (0.4 m × 0.7 m) with tension and compression reinforcement was examined by numerical analysis. The analysis was carried out for two classes of reinforcing steel ($f_{yk} = 220$ and 360 MPa). Minimum reinforcement percentage was taken as $\rho_{s \min} = 0.2\%$ and the choice of maximum reinforcement percentage $\rho_{s \max}$ was based on the main codes of practice for RC structures: Eurocode 2 [3], BS 8110 [7] and PN-B-03264 [8] and was equal to 3%. All the analysis was carried out for singly and doubly reinforced RC sections. Section parameters are shown in Figures 12 and 13.

Figures 12 and 13 show the limit state interaction curves representing concrete B25 in both states, i.e., non-oiling up and oiling up states; concrete in the latter state was subjected for 12 months to oil TU-20 action. Figure 12 depicts the diagrams representing the limit state interaction for minimum reinforcement percentage ($\rho_s = 0.2\%$)

(Figure 12a depicts singly reinforced section, and Figure 12b – doubly reinforced section). The diagrams representing the limit state interaction for the same solutions, but for maximum steel reinforcement ratio ($\rho_{s1} = 3\%$) are shown in Figure 13.

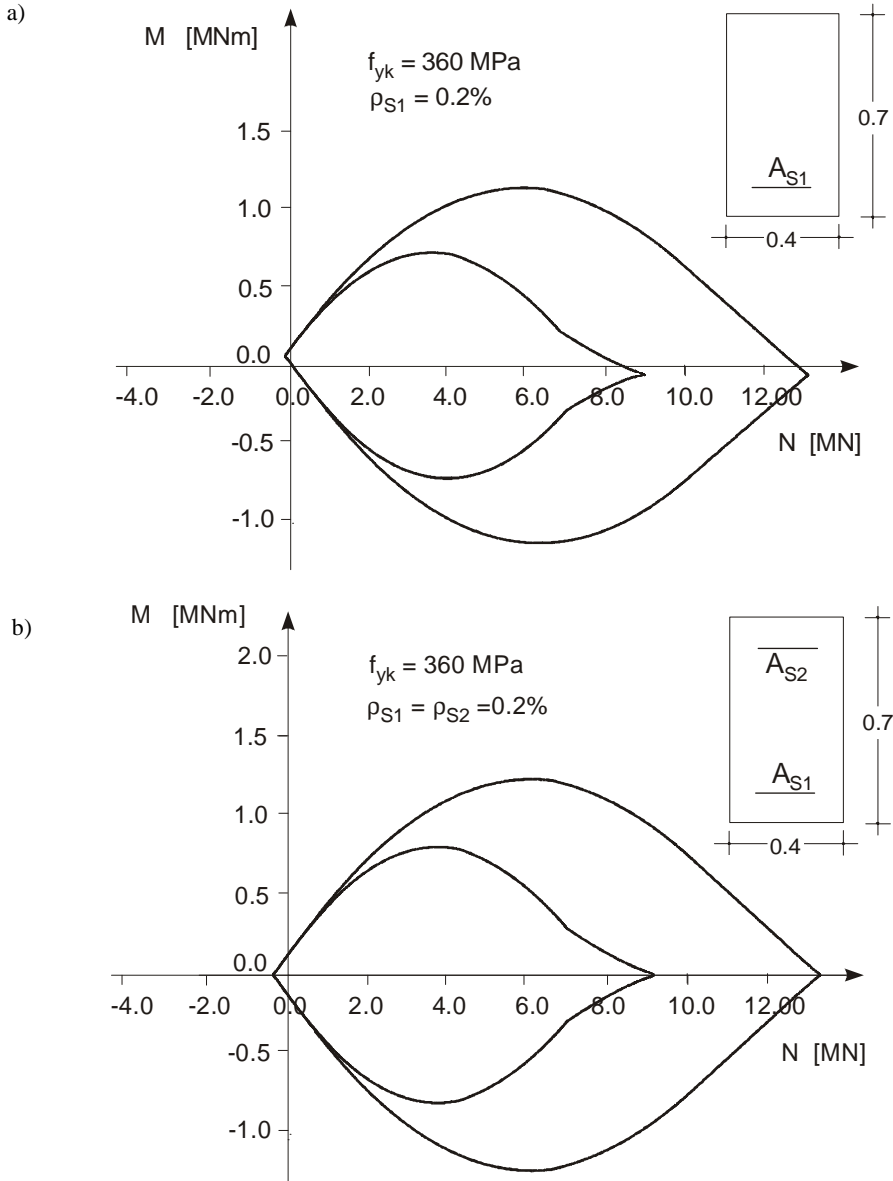
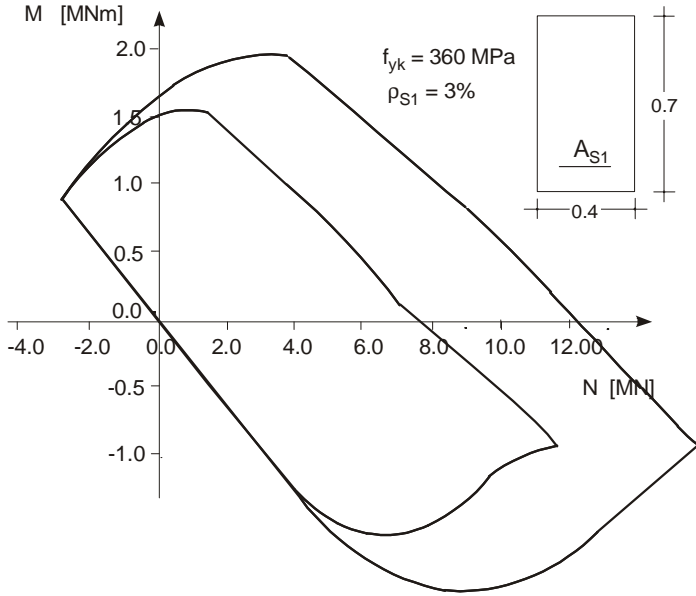


Fig. 12. The diagrams representing the limit state interaction for RC section of concrete B25 subjected to oiling up at $\rho_s = 0.2\%$: a) singly reinforced section, b) doubly reinforced section

a)



b)

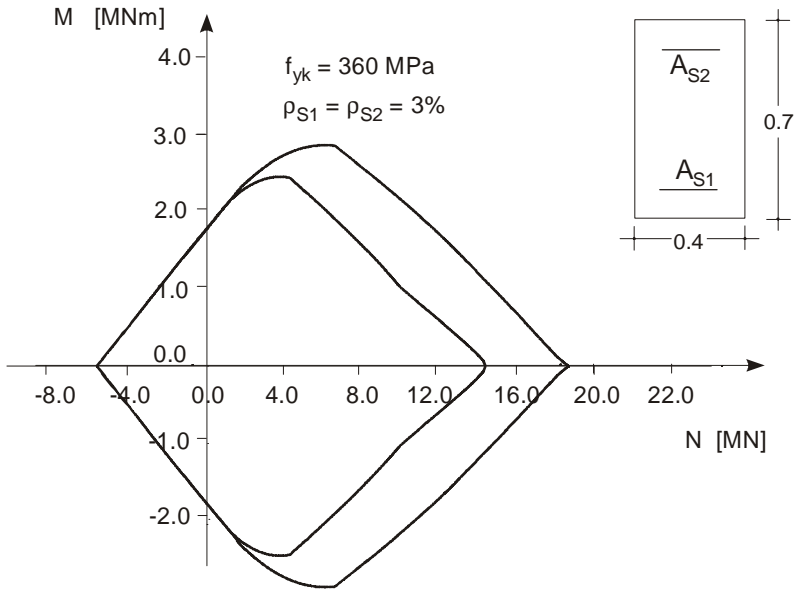
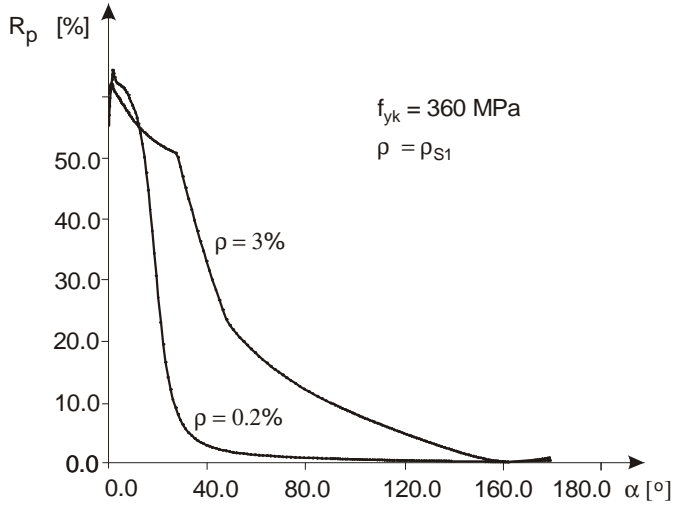


Fig. 13. The diagrams representing the limit state interaction for RC section of concrete B25 subjected to oiling up at $\rho_{s1} = 3\%$: a) singly reinforced section, b) doubly reinforced section

Figure 14 presents the distribution of divergence R_p (depending on the angle α_i , Figure 8) in the areas of bearing capacity of oiling up and non-oiling up states of steel at $f_{yk} = 360$ MPa.

a)



b)

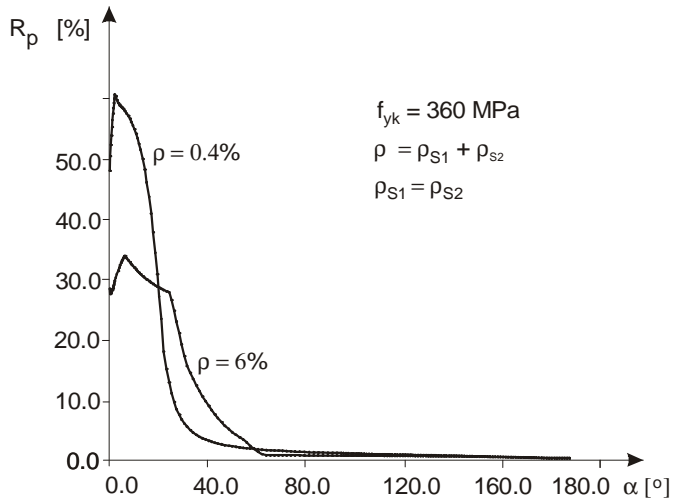


Fig. 14. Divergence in the diagrams representing the limit state interaction:
a) for singly reinforced section, b) for doubly reinforced section

It can be seen from Figure 14 that maximum divergence is in the case, where the angle α approaches zero, i.e., in the case of axial compression with small part of bending moment, and minimum value is in the case, where the angle $\alpha = 90^\circ$, i.e., for bending only.

Figure 15 shows the dependence of the divergence R_p in the sections RC analysed on the steel reinforcement ratio in the cross-section at $f_{yk} = 220$ and 360 MPa.

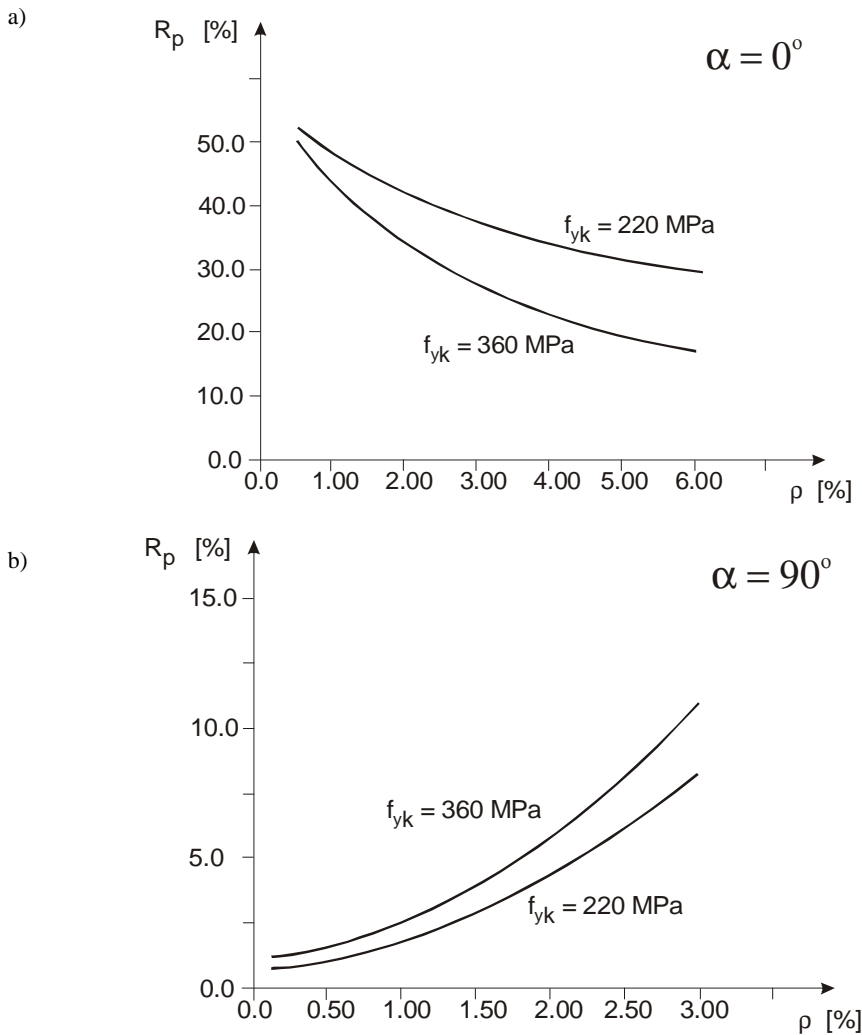


Fig. 15. Dependence of maximum divergence R_p on steel reinforcement ratio ρ_α :
a) for doubly reinforced compressed section, b) for singly reinforced bended section

6. Conclusions

As the numerical analysis presented proves, the limit state interaction diagrams are determined based on the degree of concrete oiling up and the degree of section reinforcement. The loss of bearing capacity of RC section in mineral oil environment ranges from 0 to 50% and is up to internal forces relation in RC section. In the case of

great participation of longitudinal force, the divergence rises with the lowering of both reinforcement percentage and steel strength, and can reach 50%. In the case of bending conditions only, the divergence decreases with the drop in the reinforcement percentage and the drop in steel strength, and could approach 10%. A remarkable lowering of bearing capacity of RC oiled sections testifies to the necessity of taking this fact into account in the design and assessment of the process.

References

- [1] Błaszczński T.: *Durability analysis of RC structures exposed to a physico-chemical environment*, Proceedings of the Third Kerensky Conference, Singapore, 1994, 67–70.
- [2] Błaszczński T.: *Some effects of crude oil environment on RC structures*, Foundation of Civil and Environmental Engineering, 2002, No. 2, 7.
- [3] *Eurocode 2. Design of concrete structures*. Polish version - ENV 1992 –1-1:1991.
- [4] Ścigałło J.: *The limit state interaction diagrams of RC sections and their advantages in structural optimization*, (in Polish), PhD Thesis, Poznań University of Technology, 1995.
- [5] Saenz L.P.: *Equation for the stress-strain curve of concrete*, Journal of ACI, 1964, Vol. 61, No. 9, 1227.
- [6] Godycki-Ćwirko T.: *Concrete mechanics*, (in Polish), Arkady, Warszawa, 1982.
- [7] BS 8110:1985. *Structural use of concrete. Code of practice for design and construction*.
- [8] PN-B-03264:2002. *Concrete, reinforced concrete and prestressed structures. Structural analysis and designing* (in Polish).

Ocena granicznej nośności przekroju żelbetowego poddanego oddziaływaniu olejów mineralnych

Przedstawiono ocenę granicznej nośności zaolejonego przekroju żelbetowego poddanego zginaniu i mimośrodowemu ścisnaniu. Rozważono dwa stany: niezaolejony i zaolejony (po 12 miesiącach oddziaływania oleju mineralnego). Graniczną nośność przekroju zbrojonego zaolejanego olejami mineralnymi oceniono numerycznie, wykorzystując krzywe graniczne. Analizy przeprowadzono dla przekroju prostokątnego podwójnie zbrojonego. Wykazano, że w stanie zaolejonym nośność graniczna przekroju żelbetowego jest mniejsza niż w stanie niezaolejonym.

Full-scale field tests of soil-steel bridge structure in two stages of its construction

Z. MAŃKO

Wrocław University of Technology, Wybrzeże Wyspiańskiego no. 27, 50-370 Wrocław, Poland

D. BĘBEN

Opole University of Technology, ul. Katowicka 48, 45-048 Opole, Poland

The paper presents the test procedures used for static load testing of a single-span road bridge, made from *Super Cor* corrugated steel plates, over the Bystrzyca Dusznicka River in Szczytna Zdrój, Poland, and the analysis of the results obtained. The conclusions drawn from this research can be useful for engineering practice, particularly for determining the interaction between the steel corrugated-plate shell structure and the surrounding soil, and they can be extended to the whole class of such bridge designs.

Keywords: *static field test, shell structure, corrugated plate, road bridge, backfill*

1. Introduction

Tests carried out in two stages of construction of a road bridge over the Bystrzyca Dusznicka River in Szczytna Zdrój, Poland, at the 2+240 km of Polanica Zdrój–Szczytna Zdrój district road no. 45117 are described. The test and calculation results obtained are verified [1]. The bridge is a flexible structure made from *Super Cor SC-56B* corrugated plates joined together by high-tensile bolts, founded in the ground on reinforced concrete continuous footings. In both stages of testing, i.e., the bridge without its roadway structure (backfill – stage 1) and under the principal static load (completed bridge – stage 2), deflection and strains were measured in selected points of the steel shell structure [1–3].

The objective of the experimental studies was to assess the behaviour of the bridge structure under a known load in order to validate the assumptions made in the static structural analysis and in the test live-load as well as to determine the bridge's actual load capacity and the contribution of soil consolidation to the reduction of the impact of vehicle wheels on the steel shell structure. Mainly the stiffness of the corrugated plates in the single-span structure was to be assessed and the shell width interacting in carrying loads (in particular, the transverse distribution of the load among the individual part of corrugations) was to be determined. Three span cross-sections under an asymmetric load (scheme I) and a symmetric load (schemes II and III) – relative to the bridge's longitudinal axis were tested [1, 3].

The conclusions drawn from the research had a bearing on the acceptance of the bridge for normal service under the class B load (400 kN) and served as the basis for

post-construction recommendations. They confirmed that the bridge's span and its strip foundations (supports) had been properly constructed. The measurements constituted the acceptance tests required by the bridge regulations [4–9].

Considering that it is a main bridge located in a tourist area (after the great flood of 1997 the road remained closed for several years), that it is prototype (in comparison with Canada or USA, few such bridges are built in Poland and Europe), it has been thoroughly tested under different loads and detailed analyses of the test results have been carried out. The conclusions drawn from the investigations can be useful for engineering practice, particularly for the test loading of steel road bridges made from corrugated or flat plates, and can be extended to the whole class of such bridge designs [1, 3, 10–15].

The advantage of steel flexible bridge structures made from corrugated plates lies in the fact that their interaction with the surrounding soil (usually native soil) can be exploited. Such bridges became feasible as composite steel shell with soil structures.

2. Short description of bridge

In its longitudinal section, the bridge has the form of a rigidly restrained single-span shell structure (of the *box culvert* type according to *Atlantic Industries Limited* – Canada) having effective span $l_i = 12.315$ m (Figure 1). In its cross-section, the bridge has a steel load-bearing shell structure made from corrugated plates of the corrugation depth of 140 mm, pitch of 380 mm and plate thickness $t = 7.10$ mm, joined together along the span by class 8.8 high-tensile bolts M20 forcing interaction of the span structure in both the longitudinal and transverse directions. The span is founded, by means of steel uneven-armed channel bars, on two reinforced concrete continuous footings (Figure 1). The shell structure is reinforced in three places, i.e., in the crown and in the two haunches (at the strip foundations) on the soil side on both sides of the bridge, with additional corrugated steel sheets spaced at every 380 mm to increase its transverse rigidity so that the bridge can carry the heavy standard loads. The load-bearing structure has the form of a flexible shell made from corrugated plates and earthed up with 0.20 m thick courses of permeable soil compacted to $I_D = 95\%$ (on the Proctor Normal scale) for the soil being in direct contact with the steel shell and to $I_D = 98\%$ for the other backfill whereby a pavement could be laid on a crushed stone subcrust [1, 3]. The span total thickness (the height of the plate corrugation) is $h = 380$ mm. The bridge length is: at the top $b_g = 14.00$ m and $b_d = 21.50$ m at the bottom. In plan the bridge is situated perpendicularly to the river current. The clear height under the bridge is 4.75 m. In order to increase the span's transverse rigidity and to secure the embankment slopes, reinforced concrete collars were made on the span sides. The bridge has two culverts made from $\phi = 1000$ mm *Pecor* pipes (to carry and discharge the increased flow of water during spring thaws or freshets) which constitute the main points of water thrust during a disaster (then the backfill around is allowed to be destroyed to prevent damage to the steel shell). The shell was secured in the strip foun-

datations by means of a 0.50 m high reinforced concrete collar (Figure 1). The bridge has sidewalks, each 1.50 m wide, on both sides of the roadway and typical SP-06 barriers [1, 3].

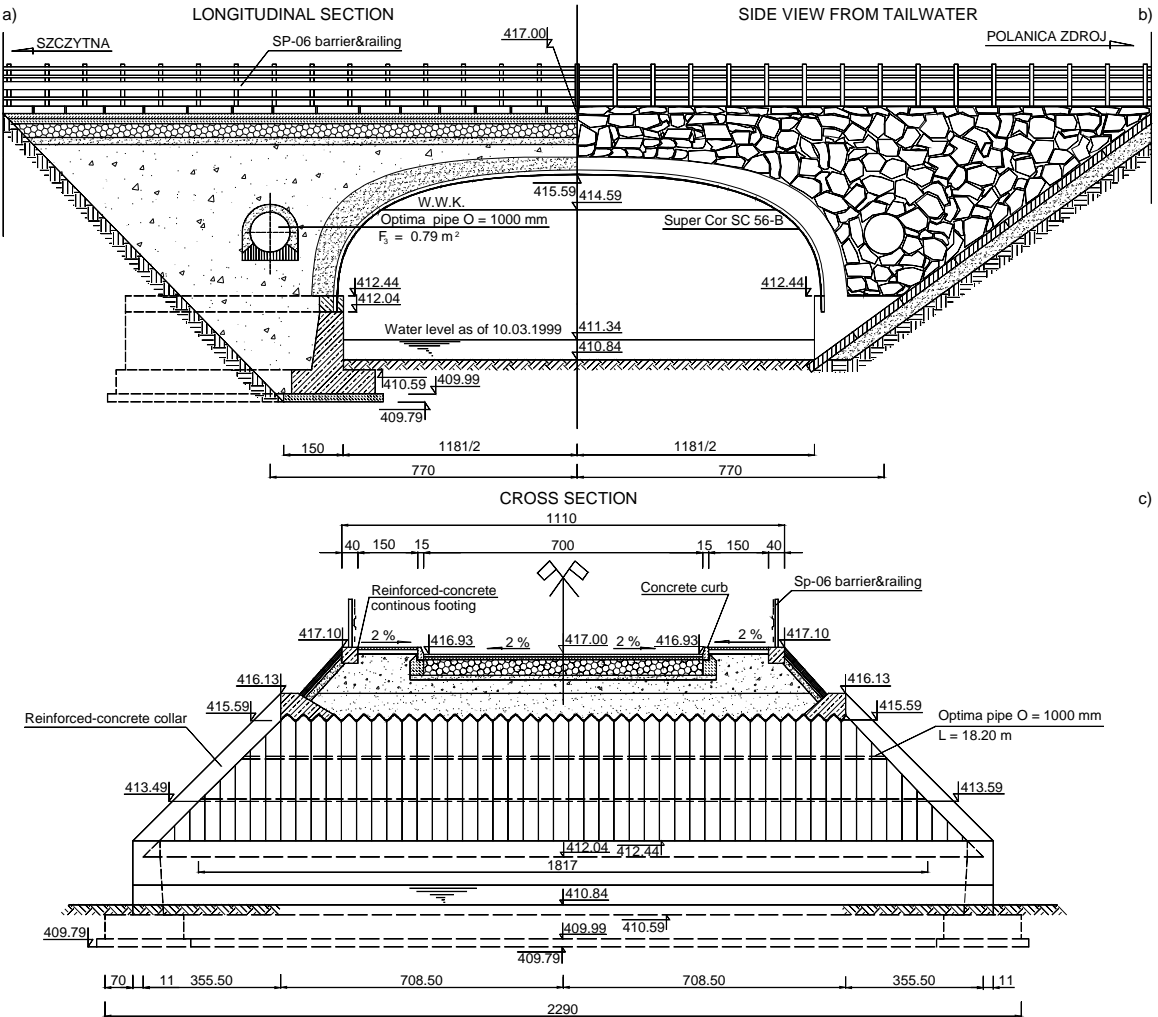


Fig. 1. Road bridge made from Super Cor SC-56B corrugated steel plates, located in Szczytna Zdrój:
a) longitudinal section, b) side view from tailwater side, c) cross-section



Fig. 2. Front view of bridge (without roadway layers) during test stage 1 (load scheme I)

3. Range and technique of tests

A *Jelcz Steyr* truck and a *Kamaz 5511* truck were used as the ballasting vehicles in the two stages of static testing. The total weight of the two trucks was over 500 kN (Figures 2–4). The expected static quantities, strains and displacements produced by the vehicles were calculated. The tests were to cover the full static (and dynamic) range and include measurements of displacements and strains (indirectly normal stresses) in the selected cross-sections of the shell structure. Three basic load schemes, i.e., one asymmetrical scheme (the two trucks positioned at one curb – scheme I shown in Figure 2) and two symmetrical (relative to the bridge’s longitudinal axis – schemes II and III shown in Figures 3 and 4, respectively) were realized.



Fig. 3. Front view of bridge during test stage 2 (load scheme II)

The settlement of the strip foundations was neglected since for this type of bridge structure and subsoil (rocky soil) it was insignificant and probably had already taken place – no deviations or irregularities in the foundations' behaviour or work were observed prior, during and after the tests.

For each of the three static load schemes (with the load positioned at half of the effective span) in the three selected cross-sections, i.e., in the crown, at the end of the crown reinforcement (where a change in stiffness occurs) and in the haunch, deflections and strains were measured several times in the two main test stages, i.e., before the bridge roadway was laid (during the construction of the steel shell, covering it with backfill layers and compacting the latter) and after the bridge was completed, i.e., under the field load. The following quantities were measured for selected corrugations:

- strains in the longitudinal and transverse directions of the span;
- horizontal and vertical (deflections) displacements in more than ten parts of corrugation;
- the effect of dynamic interactions on the displacement and strain values;
- pressures in the soil.

In order to ensure a proper safety margin for the structure, the loads determined by weighing the ballasting vehicles (the heavier rear axles were positioned in the critical sections of span and the weighed front and rear axles together exceeded the total weight) were assumed for calculations.



Fig. 4. Side view of bridge and scaffolds for measuring displacements during field load tests during stage 2 (load scheme III)

Before the tests the measuring circuits in the recording instruments had been calibrated for a fixed displacement value, e.g., 30 mm. The first indications (zero readings) had been obtained before the load was brought onto the span. After the ballasting

load was brought onto the span further readings were taken from all the instruments every 10 minutes for at least 30 minutes and after unloading until the readings stabilized. If the difference between two consecutive readings was larger than 2%, the load had to remain on the span until the difference was below 2%. Similarly, readings were taken after unloading the span, i.e., every 10 minutes for 20 minutes. At least three such readings were taken. The differences between the last indications of the induction gauges or the dial (and strain) gauges after unloading and the initial readings represented the permanent deflections (or strains) and the differences between the total deflections (or strains) and the permanent ones constituted the elastic deflections (or strains).

4. Results of calculations and measurements

A peculiarity of flexible bridge structures made from corrugated steel plates is that the backfill around the shell participates in carrying the service loads from the wheels of the vehicles crossing the bridge. If the surrounding soil is to fully interact with the steel shell in carrying a substantial part of the load, courses of it should be properly laid down around the shell and carefully (so that the allowable stress in the steel shell is not exceeded) compacted to a proper degree measured using, for example, the Proctor Normal scale ($I_D = 95\%$ and 89%). Soil is usually compacted by means of mechanical compactors whose action (a dynamic load) significantly affects the state of stress (and strains) in the steel shell structure. Also the dead weight of the soil courses cannot be neglected. If the permissible stresses in the shell are not to be exceeded they must be continuously monitored, e.g., by measuring strains. To get a comprehensive picture of the state of stress in the shell structure in the different stages of bridge construction, strains should be measured immediately after all the soil courses had been formed, after the road base layers had been laid (before applying asphalt and making sidewalks – stage 1) and during the static load testing of the completed bridge (stage 2).

4.1. Calculations

In the test live-load, the ordinates of the bending moment and deflection (displacements) influencing lines in the particular sections of the steel shell structure were computed using a Cosmos/M program on a PC for the three load schemes (Figures 2–4) at the actual parameters of the steel and the backfill. The considerable differences between the calculation results and the experimental ones lie mainly in the calculations and in the fact that it is extremely difficult to determine the extent and magnitude of the interaction between the steel shell structure and the surrounding backfill in the numerical model [1].

The influence lines of the transverse load distribution of particular sections of corrugated plates were used to calculate the expected values of deflections f , normal stresses σ and strains ε . The main difficulty in the analysis was the assessment of the

interaction between the steel shell structure and the surrounding soil in carrying loads. The calculations were verified for the same (or similar) assumptions using computer program *Robot Millennium* and similar values were obtained. Therefore, it was decided to conduct our own calculations based on real assumptions in *FLAC* program from the nonlinear contact elements of interface type [16]. The computations were performed for the actual positions and loads of the ballasting vehicles' axles. The ordinates of the influence lines under the axles were read directly from computer printouts to avoid needless and extremely laborious (and less precise) interpolation of the ordinates.

It follows from the above that other numerical methods should be sought and more realistic assumptions should be made when building computational models of such flexible structures. Currently the authors of this paper are in possession of an excellent computing program called *FLAC* which makes a comprehensive and accurate analysis of such complex steel-soil structures possible and allows one to model the interface between the different materials. Preliminary analyses and computations performed by means of this program yielded values much closer to the test results. This is described in detail by Beben in [16]. The new finite element procedures used for the analyses of soil-structures interaction are based on the techniques for modelling soil stress-strain behaviour. This is a semi-analytic procedure based on the use of a two-dimensional finite element mesh and the Fourier integrals to treat the variations in load and response in the axial direction. This approach leads to the decomposition that is harmonic in the axial direction and computationally efficient compared with conventional three-dimensional formulations. However, it is based on the principle of superposition and requires linear material behaviour. Furthermore, the Fourier integrals imply modelling of the culvert as infinitely long.

The two-dimensional analyses are performed step by step, beginning with the structure resting on its foundation with backfill. The placement of the first layer of backfill alongside the culvert is modelled by adding the first layer of soil elements to the finite element mesh. At the same time, loads are applied representing the weights of the elements added. Through their interaction, the soil elements load the structure. Subsequent steps of the analyses are performed in the same way, adding one layer of elements at the time, which simulates the process of backfilling around and over the shell structure. After the final layer of fill has been placed over the top of the structure, loads are applied to the surface of the fill to simulate vehicular traffic loads [16].

The soil is modelled as elastic-plastic model (the Coulomb-Mohr criterion), with linear modulus variations with depth. Modulus variation $E(z) = E_0 + mz$ is defined using surface modulus E_0 and modulus gradient m . The parameters used for modelling for 95% Standard Proctor are as follows: Poisson's ratio $\nu = 0.17$; cohesion $c = 0$, friction angle $\phi = 43^\circ$; gradient $m = 3.8$ MPa/m; $E_0 = 20$ MPa and unit weight of soil $\gamma = 20\text{--}26$ kN/m³. The steel structure of box culvert type was modelled as bilinear elastic with material constants of: initial Young's modulus $E_1 = 207$ GPa; secondary Young's modulus $E_2 = 12$ GPa; Poisson's ratio $\nu = 0.30$; yield stress $\sigma_y = 282$ MPa.

Table 1. Measured and calculated maximum normal stresses (MPa) in steel shell in test stage 1

Load scheme	Gauge no.	Analyzed cross-section at span shell level								
		Crown			End of crown reinforcement			Haunch		
		σ_m	σ_c	σ_m/σ_c (%)	σ_m	σ_c	σ_m/σ_c (%)	σ_m	σ_c	σ_m/σ_c (%)
I	1	4	20	20.00	16	40	40.00	–	–	–
	2	4	21	19.05	76	105	72.38	–	–	–
	2'	–	–	–	80	130	61.53	–	–	–
	3	6	18	33.33	–	–	–	–	–	–
	4	2	15	13.13	–	–	–	14	30	46.66
	5	4	17	23.52	57	110	51.81	12	28	42.85
	6	31	50	62.00	109	150	72.66	–	–	–
	6'	–	–	–	39	70	55.71	–	–	–
	7	62	80	77.50	–	–	–	–	–	–
	8	6	23	26.05	–	–	–	–	–	–
	9	158	200	79.00	82	134	61.19	16	50	32.00
10	14	28	50.00	107	180	59.44	201	290	69.31	
10'	–	–	–	205	240	85.42	–	–	–	
II	1	2	13	15.38	68	108	62.96	–	–	–
	2	6	20	30.00	21	40	52.50	–	–	–
	2'	–	–	–	68	95	71.57	–	–	–
	3	4	16	25.00	–	–	–	–	–	–
	4	6	27	22.22	–	–	–	4	28	14.28
	5	4	21	19.04	129	189	68.25	4	30	13.33
	6	25	47	53.19	82	150	45.55	–	–	–
	6'	–	–	–	100	160	62.50	–	–	–
	7	45	60	75.00	–	–	–	–	–	–
	8	4	12	33.33	–	–	–	–	–	–
	9	16	25	64.00	133	190	70.00	6	35	17.14
10	72	120	60.00	55	105	52.38	10	40	25.00	
10'	–	–	–	156	200	78.00	–	–	–	
III	1	6	19	31.57	60	90	66.66	–	–	–
	2	10	32	31.25	6	17	35.29	–	–	–
	2'	–	–	–	45	78	57.69	–	–	–
	3	4	18	22.22	–	–	–	–	–	–
	4	6	26	23.07	–	–	–	4	30	13.33
	5	12	27	44.44	47	80	58.75	8	50	16.00
	6	35	65	53.84	70	120	58.33	–	–	–
	6'	–	–	–	49	92	53.26	–	–	–
	7	19	40	47.50	–	–	–	–	–	–
	8	12	29	41.37	–	–	–	–	–	–
	9	19	37	51.35	101	160	63.12	14	50	28.00
10	6	16	37.50	31	50	62.00	4	28	14.28	
10'	–	–	–	74	120	61.66	–	–	–	

Note: ' – gauge place on top edge of reinforcing plate.
 σ_m, σ_c – measured and calculated normal stresses, respectively.

Table 2. Measured and calculated maximum normal stresses (MPa) in steel shell in test stage 2

Load schemes	Gauge no.	Analyzed cross-section at span shell level								
		Crown			End of crown reinforcement			Haunch		
		σ_m	σ_c	σ_m/σ_c (%)	σ_m	σ_c	σ_m/σ_c (%)	σ_m	σ_c	σ_m/σ_c (%)
I	1	2	25	8.00	4	26	15.38	–	–	–
	2	d	29	–	0	23	0.00	–	–	–
	2'	–	–	–	0	22	0.00	–	–	–
	3	4	30	13.33	–	–	–	–	–	–
	4	2	26	7.60	–	–	–	4	19	21.05
	5	2	29	6.80	6	34	17.64	2	19	10.52
	6	4	31	12.90	2	22	9.09	–	–	–
	6'	–	–	–	4	23	17.39	–	–	–
	7	2	18	11.11	–	–	–	–	–	–
	8	2	19	10.52	–	–	–	–	–	–
	9	4	24	16.66	12	34	35.94	4	21	19.05
10	6	39	15.38	0	30	0.00	4	25	16.00	
10'	–	–	–	2	12	16.66	–	–	–	
II	1	2	25	8.00	2	16	12.50	–	–	–
	2	d	27	–	4	21	19.04	–	–	–
	2'	–	–	–	2	16	12.50	–	–	–
	3	2	16	12.50	–	–	–	–	–	–
	4	0	18	0.00	–	–	–	8	34	23.52
	5	2	14	14.28	2	13	15.38	8	32	25.00
	6	0	14	0.00	12	36	33.33	–	–	–
	6'	–	–	–	2	13	15.38	–	–	–
	7	6	24	25.00	–	–	–	–	–	–
	8	2	14	14.28	–	–	–	–	–	–
	9	2	15	13.33	0	12	0.00	2	18	11.11
10	0	12	0.00	10	26	38.46	0	14	0.00	
10'	–	–	–	2	15	13.13	–	–	–	
III	1	0	15	0.00	0	13	0.00	–	–	–
	2	d	12	–	8	35	22.85	–	–	–
	2'	–	–	–	0	17	0.00	–	–	–
	3	8	32	25.00	–	–	–	–	–	–
	4	4	24	16.66	–	–	–	8	40	20.00
	5	8	36	22.22	2	19	10.52	8	38	21.05
	6	2	21	9.50	8	37	21.62	–	–	–
	6'	–	–	–	8	40	20.00	–	–	–
	7	0	20	0.00	–	–	–	–	–	–
	8	10	40	25.00	–	–	–	–	–	–
	9	4	25	16.00	16	40	40.00	6	35	17.14
10	12	43	27.90	8	28	28.57	10	40	25.00	
10'	–	–	–	0	23	0.00	–	–	–	

Note: ' – gauge place on top edge of reinforcing plate.

σ_m , σ_c – measured and calculated normal stresses, respectively.

d – damaged gauge.

The behaviour of the flexible structure of box culvert type is dependent to a large extent on its interaction with surrounding soil backfill, which restrains the tendency of the sides of the structures to flex outward and greatly increases the load-carrying capacity compared with that of a free-standing structure. It is this aspect of their behaviour that makes the use of soil–structure interaction analyses, with simulation of behaviour of both soil backfill and steel shell structure, absolutely essential to provide a realistic basis for design. Some of the maximum calculated displacements and strains (stresses) values obtained from FEM analysis are presented in Tables 1, 2 and 3. In these tables, the relative variations and proportions between calculated and measured values are also shown.

Table 3. Measured and calculated maximum vertical displacements (10^{-3} m) in steel shell in test stages 1 and 2

Gauge no.	Load schemes								
	I			II			III		
	Stage 1								
	f_m	f_c	f_m/f_c (%)	f_m	f_c	f_m/f_c (%)	f_m	f_c	f_m/f_c (%)
1	0.42	1.10	38.18	1.33	1.95	68.21	0.48	1.11	43.24
2	0.96	1.70	56.47	1.79	2.53	70.75	1.28	2.05	62.43
3	1.89	2.55	74.11	2.19	2.98	73.48	2.08	3.09	67.31
4	2.15	3.62	59.39	2.21	3.12	70.83	3.64	4.55	80.00
5	2.60	3.90	66.66	1.71	3.05	56.07	4.35	5.34	81.46
6	1.56	2.90	53.79	0.54	1.21	44.62	3.07	4.56	67.47
7	0.75	1.50	50.00	0.08	1.00	8.00	2.51	3.25	77.23
	Stage 2								
1	0.52	1.15	45.22	1.04	1.89	55.02	0.76	1.52	50.00
2	0.81	1.35	60.00	1.56	2.35	66.38	1.46	2.59	56.37
3	1.21	1.80	67.22	1.70	3.02	56.29	2.21	2.96	74.66
4	1.40	2.55	54.90	1.52	2.29	66.37	2.58	3.67	70.29
5	1.73	2.50	69.20	1.09	1.68	64.88	3.08	4.55	67.69
6	1.42	2.28	62.28	0.84	1.32	63.63	2.76	3.85	71.68
7	0.82	1.39	58.99	0.46	1.11	41.44	1.52	2.93	51.87
8	0.54	1.22	44.26	0.26	1.00	26.00	0.94	1.62	58.02

Note: f_m, f_c – measured and calculated vertical displacement, respectively.

4.2. Strains and deflections in test stage 1

Detailed diagrams of strains and deflections in time in the selected points of the shell structure under the three load schemes for the stage without a bridge roadway (stage 1) are shown in the report [17]. The diagrams of maximum strains and deflections (vertical displacements) in the selected points in the three cross-sections, i.e., in the crown, at the end of the crown reinforcement and in the haunch, for the three load schemes (I, II and III) in test stage 1 are shown in Figure 5.

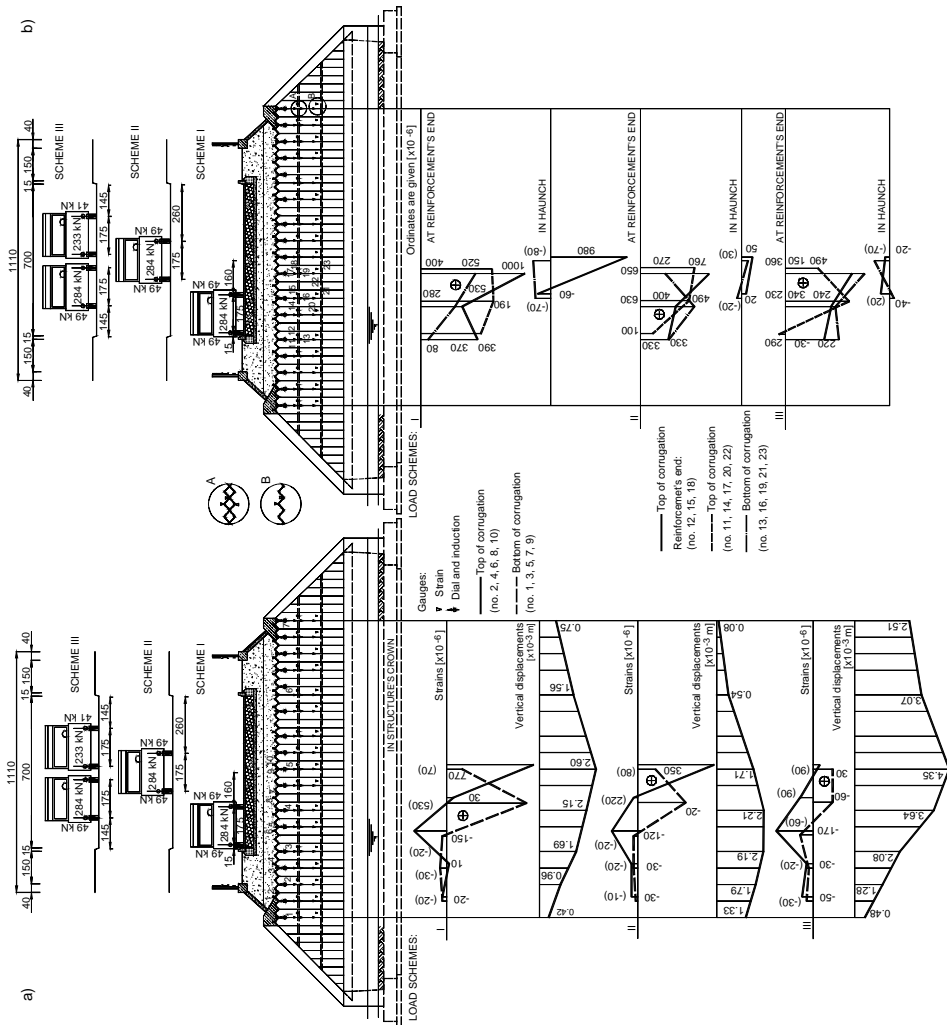


Fig. 5. Diagrams of maximum vertical displacements and strains in cross-section for three load schemes in test stage 1: a) in crown; b) at reinforcement end and in haunch

4.3. Strains and deflections in test stage 2

Diagrams of strains and deflections in time for test stage 2 (field loading) in the particular points and cross-sections (elements) of the shell structure are shown in the report [17]. The diagrams of maximum strains and vertical displacements (deflections) in the selected points in the three investigated cross-sections, i.e., in the crown, at the end of the crown reinforcement and in the haunch, for the three load schemes (I, II and III) in test stage 2 are shown in Figure 6. The initial, maximum and final readings for all the measuring points can be found in tables in the test report.

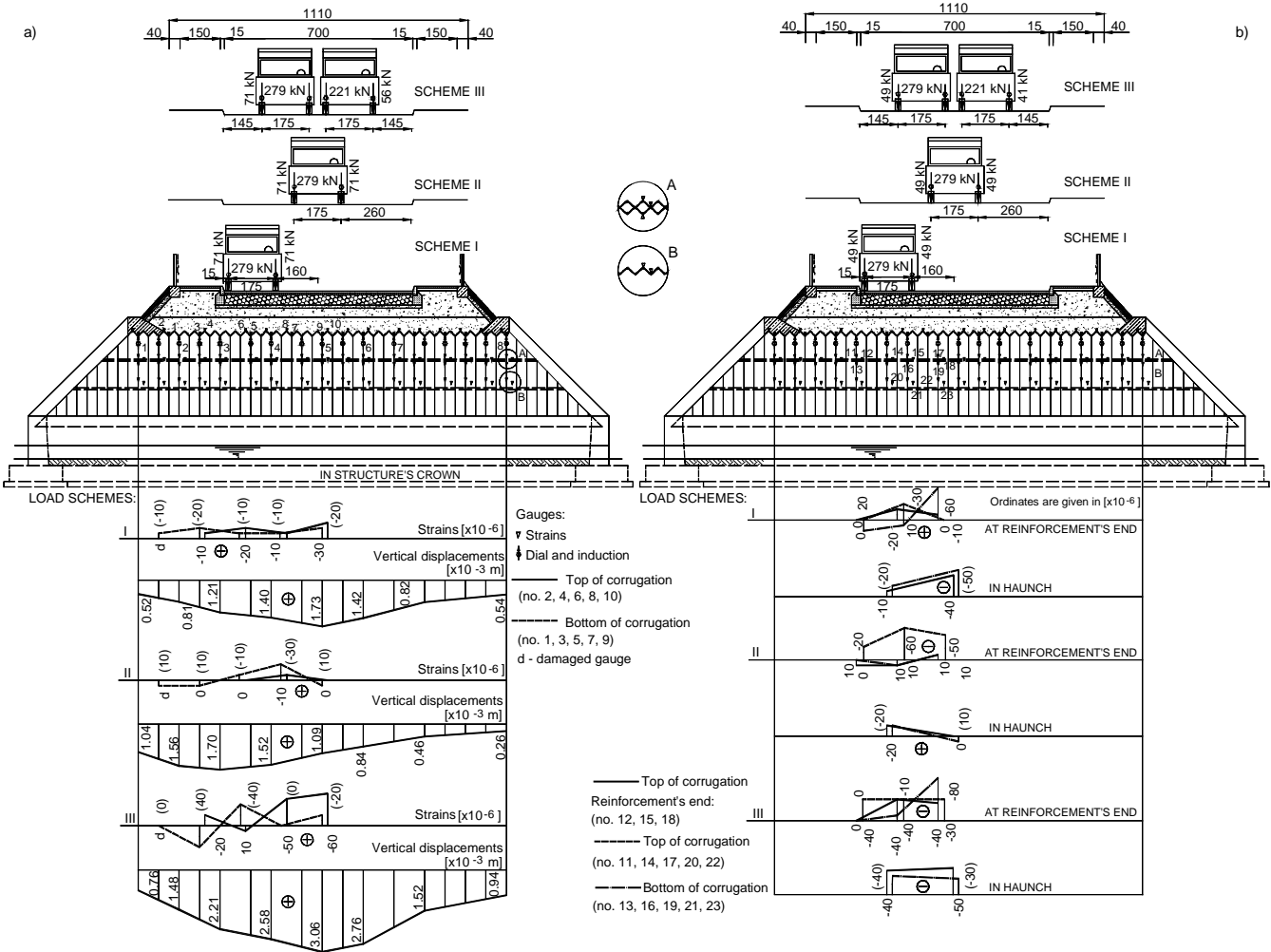


Fig. 6. Diagrams of maximum vertical displacements and strains in cross-section under three load schemes during stage 2 of testing steel bridge span: a) in crown; b) at reinforcement end and in haunch

5. Analysis of stress and deflection measurement results

5.1. Normal stresses obtained in test stage 1

The normal stresses calculated on the basis of the unit strains measured during the two stages of testing the bridge's steel shell structure are shown in Tables 1 and 2. The normal stresses measured in the corrugated plates were mostly smaller than the expected (calculated) ones in all the cross-sections considered along the length of the span.

The greatest normal stresses in the steel shell structure were measured at the end of its reinforcement under the load consisting of the two trucks (Figure 5b) during the construction of the bridge (test stage 1) and they were as follows (Table 1):

- a) under load scheme I: about 205 MPa, occurred in the part of corrugation top almost in the centre of the roadway width;
- b) under load scheme II: nearly 156 MPa, concentrated in the part of corrugation bottom between the ballasting vehicles' wheels;
- c) under load scheme III: about 101 MPa, occurred in the part of corrugation top under the vehicles' wheels.

Somewhat smaller strains (and so normal stresses) were measured in the shell haunch and they were as follows (Figure 5b and Table 1):

- a) under load scheme I (the two trucks positioned at the curb): about 201 MPa, occurred in the part of corrugation top between the vehicles' wheels;
- b) under load scheme II (the ballasting trucks positioned in the middle of the effective span (in the longitudinal direction) and in the centre of the bridge roadway (in the transverse direction): nearly 10 MPa in the edges of corrugation bottom between the vehicles' wheels;
- c) under load scheme III (the two trucks positioned in parallel in the middle of the effective span in such a way that a longitudinal axis of the span was between two rear axles of the vehicles): about 14 MPa, occurred in the part of corrugation bottom between the two trucks.

In the first cross-section investigated, i.e., in the middle of the effective span of steel structure (in the crown), the highest strain values measured were as follows (Figure 5a):

- a) under load scheme I: about 158 MPa, occurred in the part of corrugation top under the vehicles' wheels;
- b) under load scheme II: about 72 MPa, occurred in the parts of corrugation bottom and top under the outer wheels of ballasting vehicles;
- c) under load scheme III: about 35 MPa, concentrated in the part of corrugation top under the vehicles' wheels.

5.2. Normal stresses obtained in test stage 2

The greatest normal stresses in the bridge's steel shell calculated from the strains (Figure 6) measured during the test loading (test stage 2) of the bridge with the set of the two ballasting vehicles occurred at the level of the end of the shell reinforcement

(Table 2) and they were as follows:

- a) under load scheme I: about 12 MPa, concentrated in the part of corrugation top in the centre of the roadway;
- b) under load scheme II: also about 12 MPa, occurred in the part of corrugation top (on the reinforcement) under the vehicles' wheels;
- c) under load scheme III: about 16 MPa, located in the part of corrugation bottom towards the span end.

In the middle of an effective span of the shell, the following normal stresses were obtained (Figure 6a):

- a) under load scheme I: nearly 6 MPa, concentrated in the part of corrugation top in the middle of the roadway width;
- b) under load scheme II: nearly 6 MPa, occurred in the part of corrugation top towards the span end;
- c) under load scheme III: about 12 MPa, occurred in the parts of corrugation top and bottom towards the span end.

The strains (and so the normal stresses) in the structure haunch were as follows (Figure 6b):

- a) under load scheme I: 4 MPa, concentrated in the part of corrugation bottom towards the middle of the roadway width;
- b) under load scheme II: merely 8 MPa, concentrated in the part of corrugation top under the vehicles' wheels.

In test stages 1 and 2, the strains of steel shell (normal stresses), like its deflections (vertical displacements), as a rule would return to their original positions. The results obtained were traced through the different stages of construction of the bridge structure. The performance of the shell structure during all the tests was beyond reproach. Only soil stabilization (distressing) was rather slow and after relieving the span the gauges took a rather long time to return to their original readings, which might raise some suspicion, particularly in comparison with the behaviour of such gauges in the case of conventional steel spans.

Similar conclusions could be drawn from the diagrams of strains (normal stresses) and vertical displacements in several cross-sections of the steel shell structure, their linear distribution in the corrugation cross-sections, the interaction between the particular corrugated plates and the interaction between the steel shell and the surrounding backfill (Figures 5–6).

A comparison of the results shows that the expected (calculated values) of normal stress were much higher than the ones obtained on the basis of the strain measurements. Also here, like in the case of deflections (vertical displacements), there are substantial reserves of load capacity in the steel shell structure.

5.3. Vertical displacements of steel shell structure

An analysis of the displacement values measured in all the selected cross-sections of the steel shell showed that they were much lower than the expected (calculated) ones,

but in each case they had elastic character. This was true for all the selected cross-section under the three load schemes.

The differences between the initial and final readings were not roughly similar in the considered cross-sections under all the load schemes. This might have been due to the distressing of the backfill courses, the settlement of the continuous footings, small reading errors and, to a slight degree, due to the permanent deformations of the load-bearing structure interacting with the ground. It was assumed that the corrugated plates joined together by high-tensile bolts to form a flexible structure should not undergo larger permanent strains, all the more because the strip foundations were new and not subjected to such a heavy load before. One could expect that they would settle slightly when subjected to the service load of over 500 kN (close to the standard load [7]).

The ratio of the measured total displacements to the calculated ones was always lower than unity in all the cross-sections analyzed. The few deviations of the measured load-carrying structure displacements from the calculated ones were slight and the elastic displacements (with or without the settlement of the supports taken into account) were smaller than unity. This clearly proved that the displacements measured were smaller than the calculated ones. For all the load schemes the differences between the results ranged from a few to about 60% (Table 3). It was the first time that the bridge was subjected to such a heavy load and probably adjustment between some of its structural members, particularly between the corrugated plates as well as between the shell structure and the backfill around it, took place.

Moreover, the deflections were calculated for the worst case of rigidity of the individual corrugated plates, i.e., neglecting the transverse braces (the additional plates in the shell crown and haunch). Computations were also performed for the design rigidities of structural components and the values obtained were closer to the measured ones and so more advantageous from the comparative analysis point of view.

5.3.1. Vertical displacements obtained in test stage 1

The greatest vertical displacements of the shell structure (the load-bearing structure of the bridge made from corrugated plates) in test stage 1 were obtained under load scheme III (the two ballasting trucks positioned in parallel in the middle of the effective span in such a way that the longitudinal axis of span was between the rear axles of vehicles). The maximum displacements amounted to 4.35×10^{-3} m and occurred directly under the trucks' wheels. Under load scheme I (the two trucks positioned closely to the curbs) the greatest displacements of the load-bearing structure amounted to 2.60×10^{-3} m and were also located under the wheels of ballasting vehicles. Under load scheme II (the two trucks positioned in the middle of the effective span (in the longitudinal direction) and in the centre of the roadway (looking across the roadway)) they amounted to 2.21×10^{-3} m and also were concentrated under the ballasting vehicles' wheels (Figure 5a and Table 3).

5.3.2. Vertical displacements obtained in test stage 2

The greatest vertical displacements of the shell structure (the load-bearing structure of the bridge) in test stage 2 were obtained under load scheme III (the two ballasting trucks positioned in the middle of the effective span in the longitudinal direction so that the longitudinal axis of bridge was between them). They amounted to 3.08×10^{-3} m and were concentrated under the wheels of ballasting vehicles. Under load scheme I the greatest deflections of the load-bearing structure amounted to 1.73×10^{-3} m and were located directly under the trucks' wheels. Under load scheme II (the two ballasting vehicles positioned in the middle of the effective span so that their rears touched) the maximum vertical displacements occurred under the vehicles' wheels and amounted to 1.70×10^{-3} m (Figure 6a and Table 3).

A comparison of the results shows that the expected (calculated) deflections of the shell were considerably greater than the measured ones. Also here, as in the case of strains (normal stresses), the load capacity reserves in the steel shell structure were considerable.

6. Final conclusions

As a result of measurements, performed on the road bridge during construction and backfilling and under the main test static load, the vertical displacements (deflections) of the load-carrying structure and the strains (indirectly the normal stresses) in the selected points and cross-sections of the span were determined and compared with the calculated values. Taking into account the practical experience gained from static and dynamic load tests conducted on other existing bridges made from *Super Cor* or *Multiplate* corrugated plates, e.g., in Polanica Zdrój [3], in Gimån, Sweden [11], in Stary Waliszów [10] (it was also presented in [18]), the observations of the behaviour of this type of bridge structures made during the tests and the comprehensive analysis of the measurement and computation results, the following general conclusions about the actual behaviour of the bridge can be drawn:

1. In the light of the static load test results, the performance of the bridge (the span structure and the strip foundations) made from *Super Cor* corrugated steel plates was beyond reproach. The average values of the displacements and strains measured in the selected elements of the steel shell structure were much lower than the ones calculated for the same load (Tables 1–3). This became even more apparent when the permanent displacements and possible slight settlement of the supports were taken into account. This is clear evidence of a much greater stiffness of the span than the one assumed in the static-strength analysis in which such a large degree of interaction between the steel shell structure and the surrounding backfill was not foreseen.

2. The displacements measured at the top and bottom of the corrugations of the steel shell structure (made from corrugated plates joined together entirely with high-tensile bolts) and on the reinforcing plates, caused by the test load (two trucks with a total weight of over 50 Mg), had practically elastic character and were smaller than

the calculated (expected) ones in almost all considered points and cross-sections of the steel shell structure. The differences between the initial and final readings of the displacements and strains of the load-bearing structure were quite large in comparison with those for conventional steel (e.g., girder) bridges and it took a long time for them to come within the reading accuracy limits of gauges and the measuring devices and most of all, they did not exceed the permissible permanent displacements. The differences were probably due to the slight settlement of the strip foundations (supports), the irregularities in the corrugated plates and the continuous footings, reading or measuring instrument errors (changes in temperature and air humidity during the measurements) and only to a slight degree to the permanent deformations of the load-bearing structure itself.

3. Much lower, in comparison with the calculated values, average measured displacements (deflections) and strains of the load-carrying structure are evidence of much greater stiffness of the span shell – attributed to good interaction between the steel elements of plates and the surrounding backfill. The differences between the expected values and the measured ones for normal stresses (Table 1) amounted to: 13.13–85.14% (on average 46.97%) in test stage 1 and 6.80–40.00% (on average 18.06%) in stage 2, and for displacements (Table 3) they amounted to: 8.00–81.46% (on average 60.46%) in test stage 1 and 26.00–74.66% (on average 58.44%) in test stage 2. The differences can be attributed to good interaction between the steel shell and the soil and the road surface, to the fact that the road structure contributes to the distribution of a quite large concentrated load over a much larger area, whereby the strains originating directly from the vehicles' wheels acting on the shell are reduced, and to the flexibility of the steel shell in carrying the service loads. The causes of the differences between the calculated values and the measured ones lie in the calculations in which probably a too low stiffness of the shell cross-section was assumed and the interaction between the steel structure and the surrounding soil was estimated too conservatively (to increase the safety margin).

4. A comparison of the measured displacements of the load-carrying structure with the calculated ones shows considerable differences between them in the bridge and in the particular cross-sections (which contributes to the safety of the steel structure). So considerable differences might have been due to too large axle loads assumed in the calculations and analyses. Moreover, the values of displacements were computed in the grid nodes and not all the cross-sections (measuring points) investigated occurred in the same nodes in the computational model. For this reason the deflection values in the cross-sections investigated were sometimes obtained through interpolation. In addition, in grid structures the interaction between the structural components is much better than it was assumed in the original test program. This applies particularly to the transverse distribution of loads among the structural components (the corrugated plates). In the case of normal stresses, the results were found to be in better agreement, except for test stage 1.

5. The permanent displacements (amounting to less than 2% of the total deflections) measured in the particular points and cross-sections of the steel shell structure

differed from each other only slightly and they were not proportional to the elastic deflections. The distribution of the load-carrying structure elastic deflections in the span transverse direction, obtained from the measurements, had curvilinear character (broken curve) and the curvatures were much smaller than the theoretically calculated ones.

6. The settlements of strip foundations (supports) were slight and they were rather due to inaccuracy of readings, instrumental errors or irregularities in the contact between the corrugated plates and the foundation. The settlements were found to be so slight that their influence on the other deflection or deformation values was neglected, especially in view of the considerable load capacity reserves in the bridge shell structure. Since it was the first time that the strip foundations were subjected to heavy loads, one could expect some settlement, especially buckling of the plates at the joint with the foundation, under the heavy field live-load.

7. The determination of the width of load-bearing structure interacting with the soil or the pavement (the road base) is a special problem. The problem is complex and difficult and requires an in-depth analysis since in order to assess correctly the effort of the particular structural components of the span one must accurately determine their interaction in carrying the loads. Generally, it is assumed that the shell width interacting with the pavement and the ground depends on the effective span length and its thickness and stiffness, the kind of road base and the thickness and degree of compaction of the layer of soil over the steel shell. It seems that it should also depend on the rigidity of the particular structural members (dimensions of the corrugated plates), the kind and number of reinforcements and the way of loading (a concentrated or distributed load).

8. The position of the neutral axis in the cross-sections of the load-carrying structure (corrugated plates) and the strain values prove that the steel structure interacts very closely with the surrounding soil and the pavement laid on the backfill courses. This interaction greatly affects the magnitude of the displacements and strains. The neutral axes of the cross-sections of steel shell structure are situated slightly higher than the strength computations indicate.

9. Close inspection of the bridge and its high-tensile bolted joints and the supplementary and control measurements showed the bridge to be in good condition. Its performance under the heavy static (and dynamic) service load did not raise any suspicions and none of its structural elements suffered any damage. Having passed the static load tests, the bridge structure was accepted for dynamic testing and ultimately for normal service.

References

- [1] Bęben D.: *Badania mostu drogowego wykonanego z blach falistych typu Super Cor.*, III Konferencja Naukowa Doktorantów Wydziałów Budownictwa, Gliwice–Wisła, 2002, pp. 65–74.
- [2] Krajnik D., Michalski J. B.: *Pierwsze mosty kanadyjskie w Europie*, Inżynieria i Budow-

- nictwo, 2002, Vol. LVIII, No. 3–4, pp. 159–161.
- [3] Bęben D., Mańko Z.: *Badania mostu drogowego wykonanego ze stalowych blach falistych Super Cor.*, XLVIII Konferencja Naukowa Komitetu Inżynierii Lądowej i Wodnej PAN i Komitetu Nauki PZITB, Krynica, 2002, *Problemy Naukowo-Badawcze Budownictwa*, Opole – Krynica, 2002, Vol. 4, pp. 167–174.
- [4] AASHTO.: *Standard Specifications for Highway Bridges*. American Association of State Highway and Transportation Officials, New York, 1996.
- [5] PN-77/S-10040.: *Betonowe, żelbetowe konstrukcje mostowe. Wymagania i badania*.
- [6] PN-82/S-10052.: *Obiekty mostowe. Konstrukcje stalowe. Projektowanie*.
- [7] PN-85/S-10030.: *Obiekty mostowe. Obciążenia*.
- [8] PN-89/S-10050.: *Obiekty mostowe. Konstrukcje stalowe. Wymagania i badania*.
- [9] PN-91/S-10042.: *Obiekty mostowe. Konstrukcje betonowe, żelbetowe i sprężone. Projektowanie*.
- [10] Bęben D., Mańko Z.: *Badania pod obciążeniem statycznym mostu drogowego wykonanego ze stalowych blach falistych typu Multiplate położonego w miejscowości Stary Waliszów*, I Sympozjum Naukowo-Techniczne *Diagnostyka i badania mostów*, Opole, 4–6 kwietnia, 2001, Materiały Posympozjalne, Opole–Wrocław, 2003, pp. 71–96.
- [11] Bęben D., Mańko Z., Janusz L., Vaslestad J.: *Badania stalowej powłoki mostu drogowego w Gimån w Szwecji wykonanej z blach falistych typu Super Cor SC-56B podczas jej zasympyowania*, II Sympozjum Naukowo-Techniczne *Badania i diagnostyka mostów*, Opole, 2003, pp. 31–67.
- [12] Madaj A., Janusz L., Vaslestad J.: *Badania ceglanego przepustu wzmocnionego konstrukcją stalową z blach falistych*, XI Seminarium *Współczesne metody wzmocniania i przebudowy mostów*, Poznań–Kiekrz, 2001, pp. 98–105.
- [13] Madaj A., Vaslestad J., Janusz L.: *Badania in situ przepustu stalowego z blach falistych użytego do przebudowy ramowego wiaduktu kolejowego*, IX Seminarium *Współczesne metody wzmocniania i przebudowy mostów*, Poznań–Kiekrz, 1999, pp. 106–117.
- [14] Mańko Z., Bęben D.: *O badaniach odbiorczych łukowego mostu drogowego z blachy stalowej*, *Inżynieria i Budownictwo*, 2002, Vol. LVIII, No. 9, pp. 506–509.
- [15] Vaslestad J.: *Long-Term Behaviour of Flexible Large-Span Culverts*, *Transp. Research Record*, No. 1231, Transportation Research Board, Washington D.C., 1990, pp. 14–24.
- [16] Bęben D.: *Soil-Structure Interaction in Bridges Made from Steel Corrugated Plates*, PhD thesis, Faculty of Civil Engineering, Opole Technical University, Opole, September, 2005.
- [17] Bęben D., Mańko Z.: *Sprawozdanie z badań doświadczalnych mostu drogowego położonego w Szczytnej Zdroju*, Centrum Naukowo-Badawcze Rozwoju Budownictwa MO-STAR, Wrocław, 2002.
- [18] Machelski Cz., Antoniszyn G.: *Influence of live loads on the soil-steel bridges*, *Studia Geotechnica et Mechanica*, 2004, Vol. XXVI, No. 3–4, pp. 91–119.

Badania stalowo-gruntowej konstrukcji mostu w dwóch etapach jego budowy

Opisano procedurę przeprowadzania badań doświadczalnych pod obciążeniem statycznym mostu drogowego wykonanego ze stalowych blach falistych typu *Super Cor*. Obiekt jest położony nad rzeką Bystrzycą Dusznicką w Szczytnej Zdroju. Przedstawiono także analizę wyni-

ków badań. Wnioski końcowe otrzymane na podstawie wyników badań mogą być przydatne w praktyce inżynierskiej, szczególnie do określania zakresu współpracy między stalowymi blachami falistymi a otaczającym je gruntem zasypowym. Wnioski końcowe można także rozszerzyć na całą klasę podobnych rozwiązań konstrukcyjnych.

Efficiency improvement in internal grinding

J. MARKUL

Technical University of Koszalin, ul. Raclawicka 15/17, 75-620 Koszalin

B. SŁOWIŃSKI

Technical University of Koszalin, ul. Raclawicka 15/17, 75-620 Koszalin

The paper deals with the effectiveness and the possibilities of its increasing. As an example the conventional inside diameter grinding using the higher-hardness grinding wheels at higher grinding speeds was considered. The analysis was carried out for different criteria. The method for determining the standard effectiveness index was proposed. Such an index can be used for the multicriterial assessment of different processes.

Keywords: *effectiveness, grinding process, grinding wheel peripheral speed, criteria for assessment*

1. Introduction

The effectiveness and material removal rate are the most important aspects of each manufacturing process to be implemented in order to rationalise work processes and cut costs. The effectiveness concerns the task being implemented, and the rate of material removal is connected with the method for its implementing. The effectiveness is used as a measure of the positive effect achieved as a result of the expenditures incurred during the specified human activities. This effect is achieved due to the rational action, which means that the worse action is substituted for the better. In practice, it is nothing else than: “the opportunity to survive on the competitive market”. The rationality shows that the action applied is cognitively based on a proper knowledge in a given field and the practical rules following from it.

The rationality of the system could be affected (formed) only by information. This information in the specified field is collected by research centres and made available by professional journals. One of these cognitively based rules (principles) of procedure in the field of abrasive machining is, e.g., the rule applied to the processes of more efficient abrasive tools with higher hardness. However, the rule of this type has certain limitations that could be overcome using the higher grinding speeds. What efficiency of this action is, especially with reference to grinding processes taking place in the material removal rate (e.g., machining of bearing rings), became the object of research whose findings are discussed in the present paper.

2. Research problem

Global aspirations for an increase in productivity create novel trends in procedure. In the field of grinding, an increase in grinding speed is one of these trends [1]. The essence of the phenomena prevailing in the process of grinding with highperipheral speed of grinding wheel is explained on the basis of the average cross-section of the machined layer A_D given by the relation [2]:

$$A_D = \frac{v_w}{v_s} \frac{1}{N_A} \sqrt{\frac{a_e}{2r_{eg}}} \quad (1)$$

An increase in the workpiece peripheral speed v_w and the working engagement a_e makes this cross-section larger, whereas an increase in the grinding wheel peripheral speed v_s , the active grain count per unit active surface N_A of grinding wheel and the equivalent grinding wheel radius r_{eg} decreases it. According to formula (1), the peripheral speed of grinding wheel can be used to control the mechanism of abrasive wear and process dynamics.

Assuming this trend towards increasing the grinding wheel speed v_s to be legitimate, the question about this procedure in the field of conventional grinding could be referred to, i.e., up to 60 m/s (still widespread practice in industry). It is a common practice to control the grinding wheel wear in this field by changing the parameters of its structure. The decisive factor in this range is especially a change in the volume factor V_p of pores which determines its hardness by the Norton grades (E,F,G...). The question: which interconnections prevail among these variables, in the field of peripheral inside diameter grinding, became the object of the present investigations.

The essence of the beneficial effects on the higher-speed grinding v_s in conventional grinding could be explained using the schematic diagram given by Lurie [3] (Figure 1).

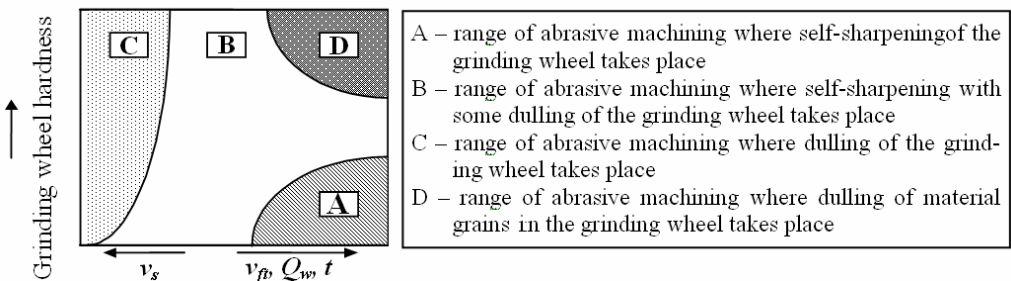


Fig. 1. Ranges of the occurrence of different mechanisms of abrasive wear and glazing of grinding wheel depending on its hardness and grinding parameters [3]

At different relationships between the grinding wheel hardness and the grinding parameters the different character of its operation is observed. Thus, if the grinding wheel with sample hardness grade K is operated at constant grinding parameters, the acceptable range of its hardness, not affecting its operating characteristic, is contained within the upper (USL) and the lower (LSL) tolerance limits ($T_K = 6\sigma_{n-1}$) (Figure 2a). However, if the peripheral speed of grinding wheel increases from v_{s1} to v_{s2} , then much wider range of grinding wheels hardness ($T_{2K} > T_{1K}$), measured by the value of standard deviation σ_{n-1} , does not affect their operating characteristic (Figure 2b).

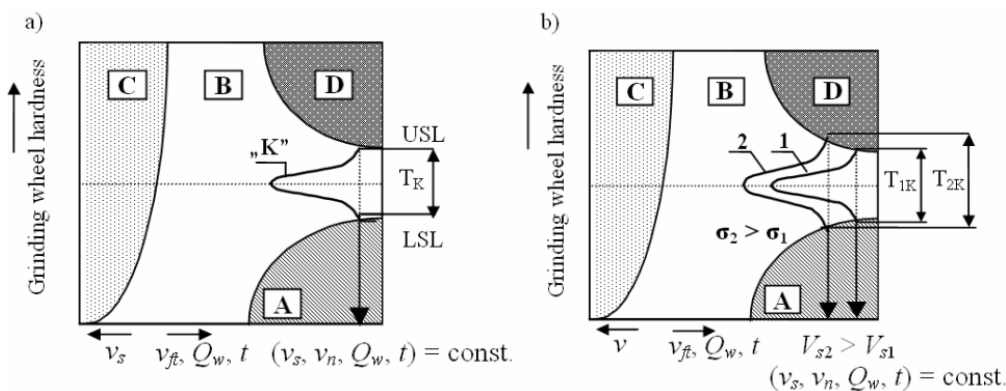


Fig. 2. Scheme for the analysis of the effects of grinding wheel speed v_s on the allowable range of grinding wheel hardness T_K : a) constant grinding speed, b) variable grinding speed

This phenomenon in workshop practice is commonly defined as “the apparent hardening of the grinding wheel”.

In the case of the peripheral inside diameter grinding, which is performed mostly in series production (e.g., bearing and automotive industry), a great number of grinding wheels with the same parameters are used. Conventional abrasive tools, especially with ceramic binder, in terms of its manufacturing process are characterized by wide range of hardness (the average of the order of 2–3 classes by the Norton scale) and due to characteristic change in the speed v_s it should have a very favourable influence on the grinding process.

3. Experimental procedure

Experimental investigations were carried out on the experimental setup specially developed in this study (affixed to the universal grinding machine RUP 28×500). The grinding wheel was driven with an electrospindle EV-70/70-2WB made by FISCHER, which allowed grinding to be carried out at the speed of up to 60,000 rpm. A frequency converter SIEB&MEYER, type 21.60, was used to supply and control the

electrospindle. The program TERM51 was used to monitor the working parameters of the electrospindle.

The objects under investigation were small-size grinding wheels of the following characteristics: 1C-25×10×10/99A80J...N5VD, prepared at the Materials Engineering Laboratory, Technical University of Koszalin (9 pieces per each test). Abrasive grains were bonded with a new binder (glass–crystalline) developed at this laboratory. It was selected due to the results of tests on abrasiveness of grinding wheels made using this binder [4].

Grinding was applied to the inside surfaces of the bearing rings with dimensions: $\phi_z = 52$ mm, $\phi_w = 40$ mm, $h = 18$ mm, made of ŁH15 bearing steel (64 ± 2 HRC). The process of grinding was carried out under the following conditions: the peripheral speeds of grinding wheel $v_s = 35$ m/s, 45 m/s and 60 m/s, the engagement of a grinding wheel: $a = 0.01$ mm, cooling with 3% emulsifiable oil (Cimtech D18) supplied via a standard sprinkler head.

Conditions of grinding wheel dressing: a diamond single-point dresser (0.5 carat in weight), the engagement of a dresser $ad = 0.005$ – 0.01 mm, the feed $f_d = 0.02$ – 0.05 rpm, without cooling.

The effectiveness of the process was estimated based on one criterion taken from three groups as follows:

- *technological group* (connected with a workpiece) – surface roughness, defined by the parameter Ra ;
- *geometrical group* (connected with a tool) – the grinding wheel radial wear Δr_s ,
- *energy-oriented group* (connected with a grinding machine) – the spindle power P_c .

The grinding was carried on until the material removal V_w reached the value of 3000 mm³. Power measurements were performed by means of sensors incorporated in the structure of the electrospindle. The roughness parameters of the surfaces machined by grinding were measured using an ME 10 profilometer, Carl Zeiss Jena, connected to an IBM computer (measuring error: $\pm 4\%$, measuring range of tracing point: ± 100 μ m, tip of tracing needle; diamond 90° , radius of tracing point: ≤ 2 μ m). Measurements of the radial wear of grinding wheel were carried out using the Abbe vertical microscope of the accuracy of 0.001 mm.

4. Results and discussion

Averaged values of the criteria for the assessment of the effectiveness of a given process are listed in Table 1.

Table 1 also includes the values of the grinding ratio G . It was calculated as the time-dependent ratio of the material removal V_w to the volumetric wear V_s . This ratio is commonly applied to the assessment of grinding processes. The relationships between the parameters investigated and the peripheral speed v_s of grinding wheel determined on the basis of the above data are given in Figure 3.

Table 1. Average values of the criteria for assessment of grinding processes using the grinding wheels: 1C-25×10×10/99A80J - N5V

Wheel speed	$v_s = 35$ [m/s]			$v_s = 45$ [m/s]			$v_s = 60$ [m/s]		
Hardness	J	L	N	J	L	N	J	L	N
Q_s [mm ³ /s]	0.059	0.027	0.015	0.056	0.026	0.017	0.056	0.023	0.014
P_c [W]	86	108	154	83	105	140	62	89	125
Ra [μm]	0.80	0.76	0.44	0.74	0.60	0.43	0.45	0.45	0.25
G	12.44	27.09	43.03	13.66	27.58	45.48	14.41	34.68	49.58

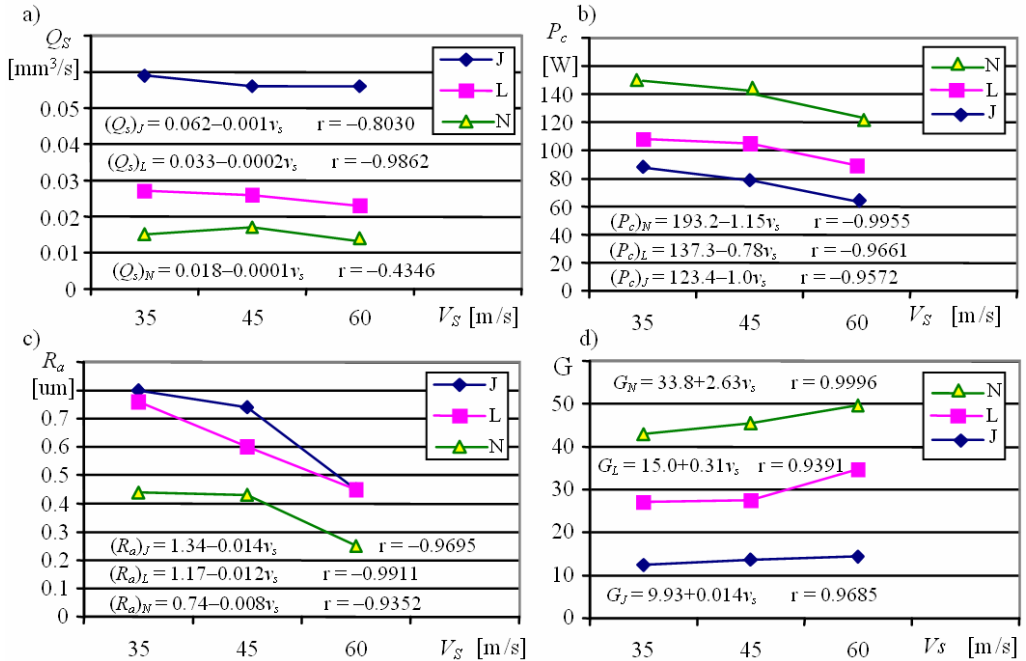


Fig. 3. Functional relationships between grinding process parameters and the wheel speed v_s : a) the rate of the grinding wheel wear Q_s , b) spindle power P_c , c) arithmetic mean of roughness Ra , d) grinding ratio G

Figure 3 shows that an increase in the speed of a grinding wheel has a beneficial influence on each of the parameters allowing the grinding effectiveness to be assessed. However, the values of these parameters depend greatly on the hardness of the grinding wheels applied. The functions obtained are strongly correlated (Person's correlation coefficient mostly exceeded the value of 0.9). Thus, these functions could be represented by straight lines of linear regression. The values of equations representing these models are given in respective figures.

It can be seen from Figure 3a that the grinding wheel with the hardness grade J is characterized by the highest abrasive wear, and at the same time it requires the highest spindle power (Figure 3b). This means that this grinding wheel works in the range of

intensive self-sharpening (range A in Figure 1). The usefulness of this grinding wheel for a given process is limited, which is confirmed by a low value of the ratio G (Figure 3d). Variation of the parameters investigated can be described by their normal distributions $N(\bar{a}, \sigma_{n-1})$, where \bar{a} is a mean value of the parameter investigated. An example illustrating such distributions for the ratio G are given in Figure 4.

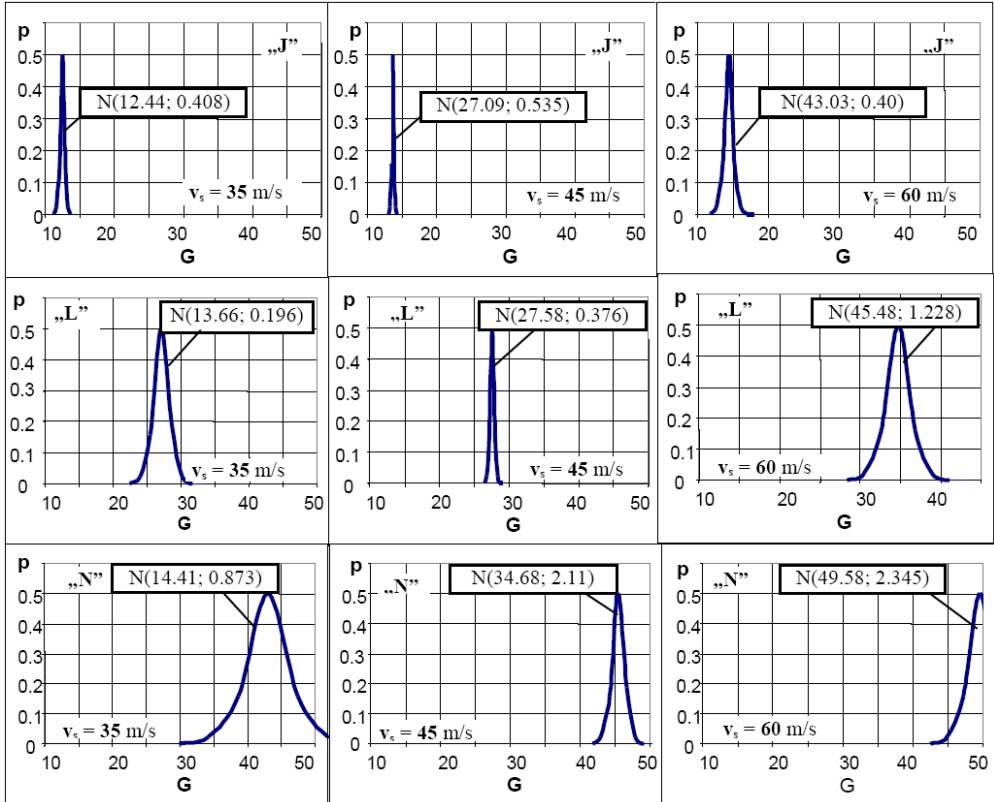


Fig. 4. Influence of the cutting speed v_c on the distributions of grinding ratio G of the grinding wheel investigated

The distributions given in Figure 4 show that the higher the speed v_s of the grinding wheel and its hardness, the wider range of the grinding ratio G . The narrowest range is found at the hardness grade L, which according to Figure 1 confirms that grinding wheels with these characteristics despite the fluctuations in the speed v_s work in the range B, i.e., the range of normal work. In the case of a grinding wheel with the hardness grade N (also partly with L), there was a wide range which means that tools with these characteristics work on the boundary of ranges (B, C). But despite such wide ranges, the increased speed is conducive to an increase in the grinding ratio G (Figure 3d).

The influence of the grinding wheel hardness (volume fraction of pores V_p) and its speed v_s on the mean value of the grinding ratio G is illustrated in Figure 5.

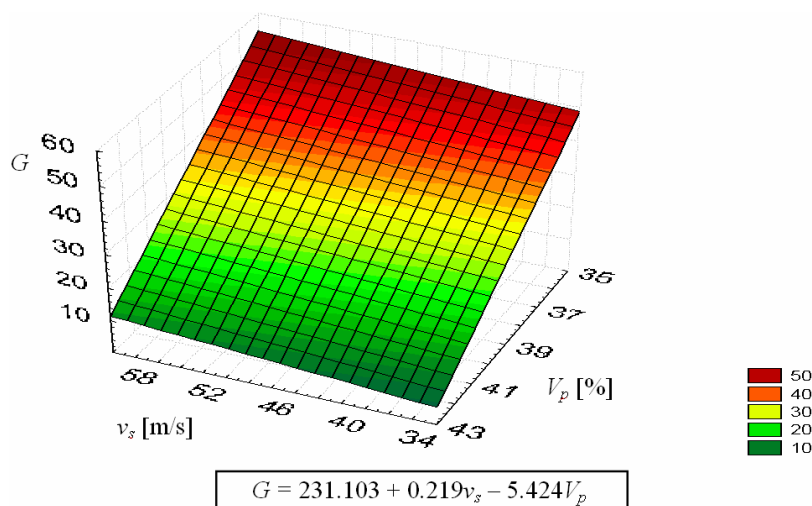


Fig. 5. The influence of pores fraction V_p and grinding wheel speed v_s on mean value of grinding ratio G

According to Figure 5 the conventional grinding is characterized by definitely stronger dependence of the grinding ratio G on the grinding wheel hardness than on its peripheral speed v_s . Despite a relatively small influence of the speed v_s , its increase is beneficial, especially for automated processes of inside diameter grinding considering the neutralization of (unavoidable) ranges of grinding wheel hardness in lots of tools with the same characteristics (Figure 2b). The measure of grinding process effectiveness in specific applications is not only the ratio G , but also the synthetic index, which includes all the individual criteria taken into consideration (they are listed in Table 1). For this reason a certain ordering function is required, because the applied criteria of assessment usually have different importance. This function makes it possible to arrange all the criteria on one common scale. The quality scale of 0–1 is considered to be the most advisable. The form of this ordering function W_i is the following:

$$W_i = \frac{k_{zm} - k_{\min}}{k_{\max} - k_{\min}}, \quad (2)$$

where:

- W_i – the value of the ordering function for the parameter taken for assessment,
- k_{zm} – the measured-value parameter for a specific object of research,
- k_{\max} – the maximum-value parameter for all the objects of research,
- k_{\min} – the minimum-value parameter for all the objects of research.

This form of the ordering function is appropriate for a criterion considered to be favourable for a given process (a growing value is desirable, e.g. G). If an increase in the value of the assessment criterion is not favourable for the process proceedings, the ordering function will assume the following form:

$$M_i = 1 - W_i. \quad (3)$$

As an example for the parameter Q_s (Table 1) we have: $k_{\min} = 0.014$, $k_{\max} = 0.059$, for J (at $v_s = 35$) $k_{zm} = 0.059$, for L (at $v_s = 35$) $k_{zm} = 0.027$, hence $W_{1J} = 1$, $W_{1L} = 0.29...$ It is known that an increase in the grinding wheel wear Q_s is unfavourable for the process, hence the value of the ordering function $M_{1J} = 1 - W_{1J} = 0$, $M_{1L} = 1 - W_{1L} = 0.71$.

From the summation and calculation of the ordering function average for a given object of research it is possible to determine the level of a synthetic (normalised) index of the process effectiveness assessment Q_{iso} including a given object (where s is the number of the considered criteria for assessment):

$$Q_{iso} = \sum_{i=1}^s W_i(M_i). \quad (4)$$

The index Q'_{iso} for a given group ($l = 1, 2, 3...p$) of objects is the sum:

$$Q'_{iso} = \sum_{l=1}^p Q_{iso}. \quad (5)$$

Taking into consideration the above arrangements, we calculate the value of the ordering function (for parameters from Table 1) and the values of the effectiveness assessment index Q_{iso} for a given machining system (Table 2).

Table 2. Criterion values for calculation of the effectiveness indices: Q_{iso} and Q'_{iso} for a given process

Grinding wheel speed	$v_s = 35$ [m/s]			$v_s = 45$ [m/s]			$v_s = 60$ [m/s]		
	J	L	N	J	L	N	J	L	N
$M_i(Q_s)$	0	0.71	0.98	0.07	0.73	0.93	0.07	0.80	1
$M_i(P_c)$	0.74	0.50	0	0.77	0.53	0.15	1	0.71	0.32
$M_i(Ra)$	0	0.07	0.65	0.11	0.36	0.67	0.64	0.64	1
G	0	0.39	0.82	0.03	0.40	0.89	0.05	0.60	1
Q_{iso}	0.25	0.42	0.54	0.32	0.50	0.58	0.57	0.69	0.77
Q'_{iso}	0.40			0.47			0.67		

Graphical representation of the standardised effectiveness indices Q_{iso} and Q'_{iso} is provided by the plots of Figure 6.

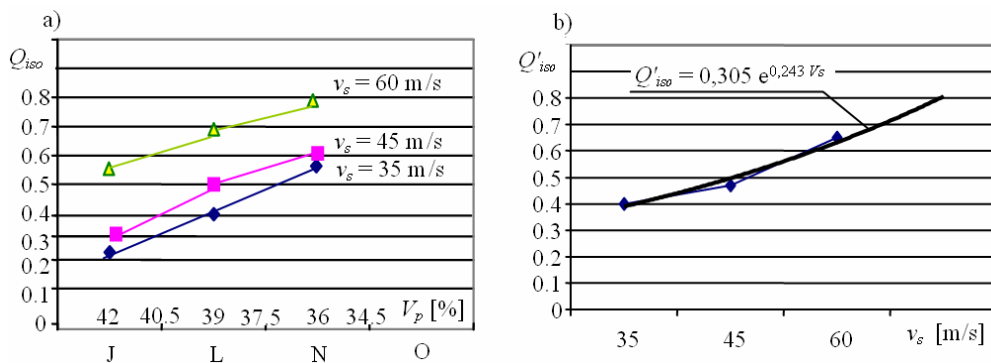


Fig. 6. Dependence of standardised indices of the grinding process effectiveness assessment: on hardness of grinding wheels applied (a), on peripheral speed of grinding wheel (b)

In the case of conventional inside diameter grinding ($v_s < 60$ m/s), it is possible to achieve higher process effectiveness both by an increase in the hardness and in the peripheral speed of grinding wheel (Figure 6). An exponential function approximates best the effects of the speed v_s to the synthetic index (Q'_{iso}) (Figure 6b), which means that the higher effectiveness of the process could be expected if this parameter was increased.

5. Conclusion

The paper gives an analysis of the effectiveness of the grinding at higher peripheral speeds and higher hardness of grinding wheels in the conventional process of inside diameter grinding. The investigations have proved that satisfying different criteria of the process assessment, especially the grinding ratio G , it is advantageous to increase the grinding wheel hardness and its speed v_s .

The effectiveness of the process investigated was also analysed on the basis of one standardised (Q_{iso}) index of multicriterial assessment. The method of such a unification by the introduction of the ordering function was also suggested. The application of this function makes it possible to reduce *multiplicity to unity*, thus satisfies the fundamental principle of normalization. Making use of one synthetic and standardised index of assessment reduces the difficulties in taking decisions and also provides optimum actions and rational use of resources with one of the fundamental premises. The present procedure can be used for the assessment of the effectiveness of any process at any number of criteria.

References

- [1] Werner G.: *Schneller Abtrag und hohe Bearbeitungs-güte durch innovative HEDG – Schleifprozesse*, Maschinenmarkt, 1997, Vol. 103, No. 36, 44–54.

- [2] Kloke F. et al.: *High-speed grinding – Fundamentals and State-of-the-Art in Europe, Japan, and the USA*, Annals of the CIRP, 1997, Vol. 46, No. 2, 715–724.
- [3] Lurie G.D.: *Šlifovanije mettalov*, Mašinstrojenije, Moskva, 1970.
- [4] Herman D., Markul J.: *Influence of microstructures of binder and abrasive grain on selected operational properties of ceramic grinding wheels made of alumina*, International Journal of Machine Tools & Manufacture, 2003, Vol. 44/5, 511–522.

Zwiększanie efektywności procesu szlifowania otworów

Na przykładzie konwencjonalnego szlifowania wewnętrznych powierzchni walcowych omówiono efektywność tego procesu oraz przedstawiono możliwości jej zwiększenia przez zastosowanie ściernic o większej twardości oraz zwiększonych prędkościach skrawania. Analizę prowadzono ze względu na różne kryteria. Podano sposób wyznaczenia unormowanego wskaźnika efektywności, który może być wykorzystywany do wielokryterialnej oceny różnych procesów.

Application of the neural network method in optimization of the drawing process of hemispherical parts made from metal sheets

G. BRABIE, F. ENE

University of Bacau, 157 Marasesti Street, 5500 Bacau, Romania

The conditions and steps necessary for the application of the neural network method in order to optimize the drawing processes of hemispherical parts made from metal sheets are analysed. The main purpose of the system based on the above mentioned method is to optimize the drawing tool geometry and the process parameters by reducing or eliminating the springback effects.

Keywords: *springback, hemispherical drawn parts, process optimization, neural network method*

1. Introduction

The drawing of sheet metals is a complex process, characterized by a series of phenomena, deciding factors and specific parameters. The springback is considered to be the main phenomenon that affects the precisions of the drawn parts. The effect of springback is reverse compared to the forming load and it modifies the values of the angles, the curvature of the part walls and the part dimensions. Generally, the springback angles decrease as the punch profile radius decreases at sufficiently large values of blankholder force and this fact is explained by the greater straining of the material and the sidewall radius decreases to the increase of die profile radius at high values of blankholder force. The mathematical models for springback calculation are based on different simplifying hypotheses concerning different factors of influence. These models lead to important differences compared with the experimental values. The main technical methods applied in order to reduce the springback can be itemized as follows: the correction of tool geometry and the value of springback angle; a supplementary deformation of the material; the utilization of stiffeners; the utilization of the punches with coining strips; the utilization of an arched counterpunch that induces supplementary deformations compensating for the springback; the utilization of variable blankholder force [1–4]. These methods have positive effect on the drawing process, but on the other hand they increase the tools complexity and costs. Based on these conclusions, it is necessary to develop a method allowing reduction or the elimination of the springback effects from the design stage and the process of forming tools.

2. Application of the neural network method

2.1. Description of optimization method

In order to find the optimum relation between the process parameters, tool geometry and springback parameters in the case of hemispherical drawn parts, use is made of an artificial neural network. In the operation of this computer system, the following steps can be itemized:

- Data collection that consists in the generation of training data. The artificial neural network (ANN) model will correctly solve the problem if it learns from a representative number of peculiar examples. If the data collected in the training set are not representative of the input data class, we can expect poor performance with the test data set, even though the performance can be excellent with the training data set.

- The choice of the ANN model. The number of the neurons within a hidden layer must be chosen in such a way that the square mean error at the end of the training process is minimal.

- The learning process of the neural networks. The neural networks must first be trained in order to make their generalization possible. In the learning process, the adjustment of the connections weights is assumed. The most common method of changing the weights connected with the net hidden neuron layers is the *back-propagation algorithm* that works as its name suggests: after the propagation of an input through the network, the error is calculated and it is propagated back through the net while the weights are adjusted in order to make the error smaller. The steps of the algorithm are as follows: 1. Perform the random initiation of the weights w_{ij} . 2. Perform the forward propagation phase for an input pattern and calculate the output error. 3. Perform the errors back-propagation and change all weight values of each weight matrix using the following relation:

$$W_{ij}(t+1) = W_{ij}(t) + \eta(t) \cdot e \cdot o_i \cdot o_{i+1} \cdot (1 - o_{i+1}), \quad (1)$$

where: w_{ij} are the connections weights, $\eta(t)$ is the learning rate; e is the error in the targets data and the current date; o_i , o_{i+1} are the outputs of the i and $i+1$ neurons, respectively. It should be stressed that the above relation is based on the uni-polar sigmoid function:

$$f(x) = \frac{1}{1 + e^{-\text{input}}}; \quad (2)$$

go to the first step 1; end the algorithm if all output pattern match their target patterns. A special attention should be paid to the correctness of the training phase, because a smaller error does not always mean a better network [5–8].

2.2 Application of the method in the case of hemispherical drawn parts

The parameters of the design and training process used in the neural network method have been optimized by using the Taguchi method. In the case of a hemispherical drawn part (Figure 1), the neural network with 3 layers (input layer, intermediate layer and output layer), a sigmoid function of activation between the input and intermediate layers and a linear function between the intermediate and output layers were chosen. In the input layer, three neurons (respectively the three process parameters R_p , R_m , F – Figure 2) and in the output layer, three geometric parameters that quantify the springback of the part (respectively r_p , r_m , ρ) were used. The number of neurons in the intermediate layer that permitted us to obtain the smallest quadratic errors was equal to 4. In order to learn the network, an algorithm of inverse propagation and a set of validation data representing 20% of the total input data were used. The learning curve is presented in Figure 3. By analyzing Figure 3 it can be seen that the chosen ANN model leads to an adequate variation in the learning curve; as a consequence, the model will be used for the next functional phase of the neural network. In order to test the capacity of generalization of the network, a set of validation data representing 30% of the total input data was used. In the Figure 4 and Table 1, a comparative analysis of the inputs desired and the inputs prescribed by the network is presented.

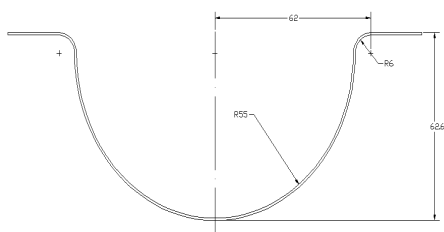


Fig. 1. Hemispherical part

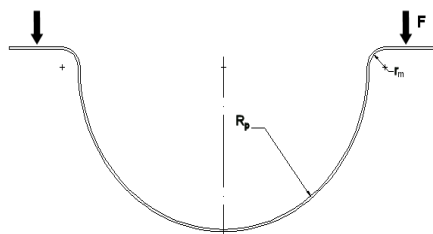


Fig. 2. Process parameters that must be considered in optimization

Table 1. The values of the inputs desired and the inputs prescribed by the network

Values desired			Values prescribed by the ANN model		
r_p	r_m	ρ	r_p	r_m	ρ
56.59	7.1	63.85	56.113	7.080	63.396
55.57	5.01	60.71	55.486	4.967	60.643
55.11	7.37	62.57	54.923	7.067	62.253

By analyzing the data of Table 1 and the diagrams given, the concordance between the inputs desired and the inputs prescribed can be observed; as a consequence the neural network is validated.

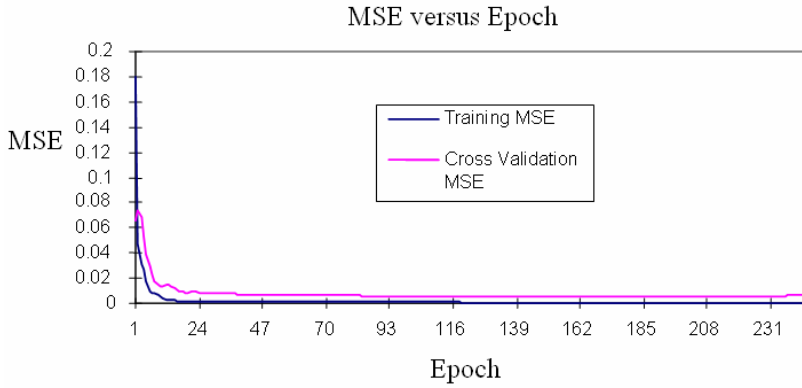


Fig. 3. The learning curve of the network. MSE – mean square error

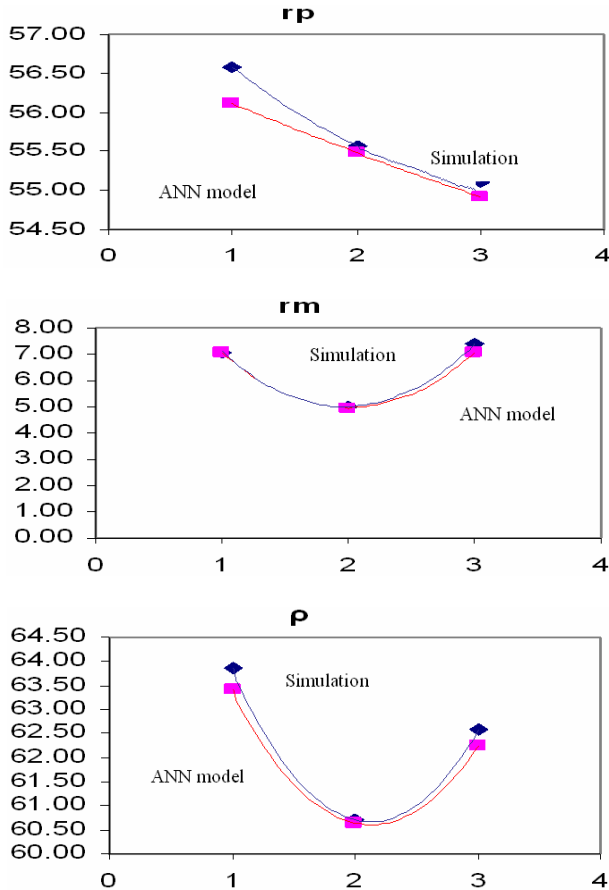


Fig. 4. A comparative analysis of the inputs desired and the inputs prescribed by the network

2.3. Optimization of the process parameters and tool geometry

In order to find the best set of the parameters that allow the springback to be reduced, the network validated will be tested for different combinations of process parameters and tool geometry. The following set of parameters was chosen: $R_p = 54.5$ mm; $R_m = 5.9$ mm; $F = 40$ kN. To validate the neural network method, a simulation has been performed using as input data this set of parameters and the results obtained were compared with the nominal geometry of the part. A comparative analysis of the results is presented in Table 2.

Table 2. Comparative analysis of results

	R_p [mm]	R_m [mm]	F [kN]	r_p [mm]	r_m [mm]	ρ [mm]
Values from simulation using the ANN model	54.5	5.9	40	54.922	5.965	61.300
Nominal values				55.00	6.000	62.000

By analyzing the results in Table 2, we arrive at the conclusion that the nominal values of the geometrical parameters of the part and the values resulted from the simulation that uses as input data the process parameters prescribed by the neural network are in agreement. As a consequence, the set of process parameters mentioned previously can be considered to be optimal. In Figures 5 and 6, the new configurations of the tools and process parameters and the resultant geometry of the part are presented.

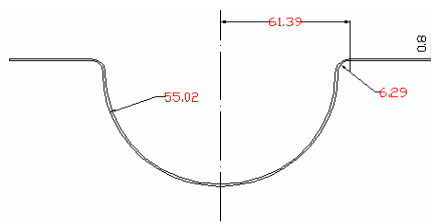


Fig. 5. Correct geometry of tools

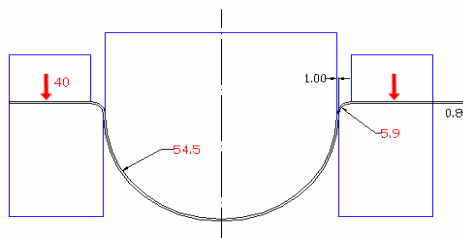


Fig. 6. Resultant part geometry

3. Conclusions

1. In order to identify an optimum relationship between the process parameters and the springback parameters, the neural network method was applied.

2. The deviations of the geometrical parameters of the part tested from the nominal profile were as follows: 0.088 mm decrease in the radius of the part sidewall r_p , 0.035 mm decrease in the radius of the connection between the part flange and part sidewall r_m , 0.7 mm, decrease in the distance ρ between the two radii.

3. The main advantage of the neural network method lies in the fact that once an adequate model is identified, the determination of the optimum process parameters can be performed in a very short time and with a minimum effort of calculus.

Acknowledgements

This research was performed with the financial support from the Romanian Ministry of Education and Research.

References

- [1] Apostolos P.: *Tooling and binder design for sheet metal forming processes compensating springback errors*, Int. J. Mech. Tools Manufact., 1996, 4, pp. 503–526.
- [2] Ghouati O., Joannic D., Gelin J.C.: *Optimization of process parameters for the control of springback in deep drawing*, Proc. of the 6th Int. Conf. on Numerical Methods in Industrial Forming Processes, Numiform'98, 1998.
- [3] Zimniak Z.: *Tooling design compensation springback errors after deep drawing and trimming operation*, ESAFORM, The 5th International Conference on Material Forming, Kraków, 2002, pp. 531–534.
- [4] Choi K.K., Kim N.H.: *Design optimization of springback in a deep drawing process*, AIAA Journal 2002, Vol. 40, No. 1, pp. 147–153.
- [5] Viswanathan V.: *Experimental implementation of neural network springback control for sheet metal forming*, Dep. of Mec. Eng. Northwestern Univ., Evanston, IL, 2001.
- [6] Cho I.N., Hung C.: *Finite element analysis and optimization of springback reduction*, International Journal of Machine Tools & Manufacture, 1999, 39, pp. 517–536.
- [7] Kinsey A.O.: *Consistent and minimal springback using stepped binder force trajectory and neural network control*, Journal of Engineering Materials and Technologies, 2000, Vol. 122.
- [8] Fausett L.: *Fundamentals of neural networks*, Prentice-Hall, 1994.

Zastosowanie metody siatek neuronowych do optymalizacji procesu tłoczenia półkulistych wyrobów z blach

Przeprowadzono analizę warunków i kroków koniecznych do zastosowania metody sieci neuronowych w celu optymalizacji procesu tłoczenia półkulistych wyrobów z blach metalicznych. Głównym celem było zastosowanie systemu optymalizującego opartego na wymienionej metodzie zoptymalizowania geometrii narzędzi stosowanych w procesie tłoczenia oraz parametrów procesu przez zmniejszenie lub wyeliminowanie powrotnych odkształceń sprężystych. Główną zaletą stosowania metody siatek neuronowych, gdy adekwatny model jest zidentyfikowany, jest znaczne skrócenie czasu obliczeń prowadzących do wyznaczenia optymalnych parametrów procesu.

Information about PhD thesis at the Civil Engineering Faculty and the Mechanical Engineering Faculty of Wrocław University of Technology

Title: *Forming the flow processes in the positive-displacement rotary pumps exemplified by the gerotor pump (in Polish)*

Kształtowanie procesów przepływowych w rotacyjnych pompach wyporowych na przykładzie pompy gerotorowej

Author: Piotr Andrzej Antoniak

Supervisor: Professor Jarosław Stryczek, Professor of Wrocław University of Technology

Promoting Council: Scientific Council of Institute of Machines Design and Operation

Reviewers:

Professor Mariusz J. Olszewski, Professor of Wrocław University of Technology

Professor Jan Kulczyk, Wrocław University of Technology

Date of PhD thesis presentation: June 06th, 2006

PhD is available in Main Library and Scientific Information Centre of WUT

The monograph contains: 132 pages, 64 figs, bibliography: 65 items.

Keywords: *machine design, displacement machines, gerotor pump, simulation*

Abstract: A theoretical model of the flow processes observed in the displacement chamber of pump was designed. Then, the model of the gerotor pump was developed by specifying relations established in a general theoretical model. The theoretical model was built and a series of theoretical examinations on the model was carried out. The influence of the selected operational parameters, the physical properties of working fluid, and the geometrical features of the gerotor pump on the pressure characteristics in the displacement chamber was determined. The system of parameters for comparing and evaluating the flow processes in the positive-displacement rotary pumps was developed. The experimental gerotor pump and the test stand were designed and constructed. Based on the verified theoretical and simulation models, the correct values of geometrical parameters (the angular displacement of the plate directional control valve) were specified for the gerotor pump of PGK series.

Title: *The influence of structural irregularities of framed tube of tall concrete building on the tube stiffness (in Polish)*
Wpływ nieregularności konstrukcyjnych powłoki ramowej betonowego budynku wysokiego na jej sztywność

Author: Rafał Piekarz

Supervisor: Professor Sylwester Kobiela, Professor of Wrocław University of Technology

Promoting Council: Scientific Council of Building Engineering Institute

Reviewers:

Professor Mieczysław Kamiński, Wrocław University of Technology

Professor Kazimierz Furtak, Cracow University of Technology

Date of PhD thesis presentation: June 7th, 2006

PhD is available in Main Library of Wrocław University of Technology

The monograph contains: 265 pages, 180 figs, bibliography: 90 items.

Keywords: *tall building, concrete framed-tube structure, cracking, stiffness*

Abstract: Theoretical and numerical research was concentrated on the behaviour of new model of concrete framed-tube structure of tall buildings made of reinforced concrete and subjected to lateral loads. The methods of linear and nonlinear numerical analyses of the population of concrete framed-tube structures of tall building at a wide range of many variable parameters were also given. The population of tall buildings made of reinforced concrete was differ in many various structural, material and loading parameters of framed-tube structures. Based on my own theoretical and numerical analyses the simplified formulas for the values of bending moments in columns and spandrel beams of web frames of framed-tube structure under lateral loads were proposed. A simple calculation method for approximate prediction of cracking influence on the stiffness characteristics of spandrel beams under lateral loads was presented as well as three methods to approximate the determination of the lateral drifts of framed-tube structures with cracked spandrel beams were also described.

Title: *The model of procurement process that takes into account the consequences of technical system unreliability (in Polish)*
Model procesu zaopatrzenia z uwzględnieniem skutków niezdatności systemu technicznego

Author: Anna Jodejko

Supervisor: Professor Tomasz Nowakowski, Professor of Wrocław University of Technology

Promoting Council: Scientific Council of Institute of Machines Design and Operation

Reviewers:

Professor Jan Szybka, University of Mining and Metallurgy in Kraków

Professor Franciszek Przystupa, Wrocław University of Technology

Date of PhD thesis presentation: June 13th, 2006

PhD is available in Main Library and Scientific Information Centre of WUT

The monograph contains: 144 pages, 63 figs, bibliography: 126 items.

Keywords: *procurement process, reliability, redundant elements, safety, reliability structure*

Abstract: One of the basic exploitation decision is to choose successful maintenance strategy. A lot of maintenance models accept an assumption that unlimited resources are necessary to make all maintenance actions in the system. This assumption, however, is not accepted by all authors, because usually resources are used according to needs and replenished again. The thesis concentrates on the problem of spare elements provision the technical systems, when elements are critical from the up-time point of view. Based on the research we can conclude that if one chooses the best inventory order level and order quantity, one should take into consideration reliability characteristics of provisioned system. When the possible severe consequences of system down-time are taken into account, the best parameters of system procurement policy change in comparison with reference models.

Title: *Evaluation of non-linear effects in steel cable-stayed bridges (in Polish)*

Ocena wpływów nieliniowych w stalowych mostach podwieszonych

Author: Przemysław Jakiel

Supervisor: Professor Zbigniew Mańko, Professor of Wrocław University of Technology

Promoting Council: Institute of Civil Engineering, Wrocław University of Technology

Reviewers:

Professor Piotr Konderla, Wrocław University of Technology

Professor Jerzy Weseli, Professor of Silesian University of Technology

Professor Witold Wolowicki, Poznań University of Technology

Date of PhD thesis presentation: April 13th, 2005

PhD is available in Main Library of Wrocław University of Technology

The monograph contains: 361 pages, 329 figs, 182 tables, bibliography: 169 items.

Keywords: *cable-stayed bridge, geometric and material nonlinearities, static and dynamic analyses, MES, field test*

Abstract: In steel cable-stayed bridges, moderately long span structures, the contribution of nonlinear influence to static response and parametric modal and stability analyses due to hinges located along a deck of untypical cable-stayed bridge were studied. Moreover, the response of chosen steel one-tower cable-stayed bridge was discussed on the basis of detailed combined field tests and numerical calculations under static and dynamic loads. The influence of geometrical and material nonlinearities on the displacement, bending moment and axial force in selected arrangements of three- and multi-span cable-stayed bridges under dead- and life loads was established. Theoretical analyses of planar 2D and spatial 3D models have been mostly conducted by FEM software Cosmos/M using suitable solution techniques for nonlinear schemes, such as these of Newton–Raphson, modified Newton–Raphson and BFGS, applying load and arc-length methods.

Title: *Study on the drawbead restraining force in the stamping processes (in Polish)*
Badanie oporów kotnierza wywołanych działaniem progów ciągowych w procesach tłoczenia blach

Author: Dawid Kręcisz

Supervisor: Professor Andrzej Matuszak, Professor of Wrocław University of Technology

Promoting Council: Faculty of Mechanical Engineering, Wrocław University of Technology

Reviewers:

Professor Monika Gierzyńska-Dolna, Częstochowa University of Technology

Professor Feliks Stachowicz, Rzeszów University of Technology

Date of PhD thesis presentation: May 17th, 2005

PhD is available in Main Library of Wrocław University of Technology

The monograph contains: 104 pages, 69 figures, bibliography, 9 items.

Keywords: *sheet metal, deep drawing, drawbead, restraining force, friction*

Abstract: This paper deals with the drawbead restraining force in the stamping processes. Nowadays, finite element analysis of the stamping processes is carried out using an equivalent drawbead model, in which the actual drawbead is replaced by its projection onto the binder surface. The restraining force produced by the actual drawbead is assigned to the nodes in the regular mesh of the equivalent drawbead. The simulation results can correspond closely with those observed in physical object, when the drawbead restraining force is reflected effectively by the equivalent drawbead model.

The drawbead restraining force was shown, both experimentally and analytically, to be a complex function of drawbead position, drawbead geometry and friction conditions. Experimental results, in the form of force–displacement curves, are compared to the results obtained both from the analytical and the numerical models. It was found that correlation between the models and experiment is not high and the significant differences in drawbead restraining force obtained by this method exist.

Finally, the regression model of drawbead restraining force has been built. The model allows us to predict accurately the influence of variations in material, geometry of the drawbead and friction condition.

Title: *Integration of simulation tools in design of machine tools with parallel kinematics (in Polish)*
Integracja narzędzi symulacyjnych w procesie projektowo-konstrukcyjnym obrabiarek o zamkniętym łańcuchu kinematycznym

Author: Piotr Górski

Supervisor: Professor Jan Koch, Wrocław University of Technology

Promoting Council: Faculty Council of Institute of Production Engineering and Automation of WUT

Reviewers:

Professor Leszek Kwapisz, Technical University of Łódź

Professor Eugeniusz Rusiński, Wrocław University of Technology

Date of PhD thesis presentation: September 20th, 2005

PhD is available in Main Library of Wrocław University of Technology

The monograph contains: 137 pages, 69 figs, bibliography: 7 items.

Keywords: *machine tool, hexapod, finite element method*

Abstract: The aim of the project is to design a model of fundamental simulation tools integration. It is assumed that integration of CAD/FEM/SIM simulation systems will allow multi-variant design and optimization of modern machine tools constructions. There were performed a number of analysis including finite elements analysis (FEM) as well as multi-mass analysis.

Information for Authors

Send to: *Archives of Civil and Mechanical Engineering*
Polish Academy of Sciences, Wrocław Branch
Podwale 75, 50-449 Wrocław, Poland

Archives of Civil and Mechanical Engineering (ACME) publishes both theoretical and experimental papers which explore or exploit new ideas and techniques in the following areas: structural engineering (structures, machines and mechanical systems), mechanics of materials (elasticity, plasticity, rheology, fatigue, fracture mechanics), materials science (metals, composites, ceramics, plastics, wood, concrete, etc., their structures and properties, methods of evaluation), manufacturing engineering (process design, simulation, diagnostics, maintenance, durability, reliability). In addition to research papers, the Editorial Board welcome: state-of-the-art reviews of specialized topics, letters to the Editor for quick publication, brief work-in-progress reports, brief accounts of completed doctoral thesis (one page is maximum), and bibliographical note on habilitation theses (maximum 250 words). All papers are subject to a referee procedure, except for letters, work-in-progress reports and doctoral and habilitation theses, which are briefly reviewed by the Editorial Board.

The papers submitted have to be unpublished works and should not be considered for publication elsewhere.

The Editorial Board would be grateful for all comments on the idea of the journal.

Submit three copies, each complete with abstract, tables, and figures.

Detailed information about the Journal on web:

<http://www.pan.wroc.pl>

www.ib.pwr.wroc.pl/wydzial/czasopismoACME.html

<http://www.wmech.pwr.wroc.pl>

Price 15 zł
(0% VAT)

Subscription orders should be addressed to:
Oficyna Wydawnicza Politechniki Wrocławskiej
Wybrzeże Wyspiańskiego 27
50-370 Wrocław